Proceedings

MICCAI-STENT'12

1st MICCAI-Workshop on Computer Assisted Stenting

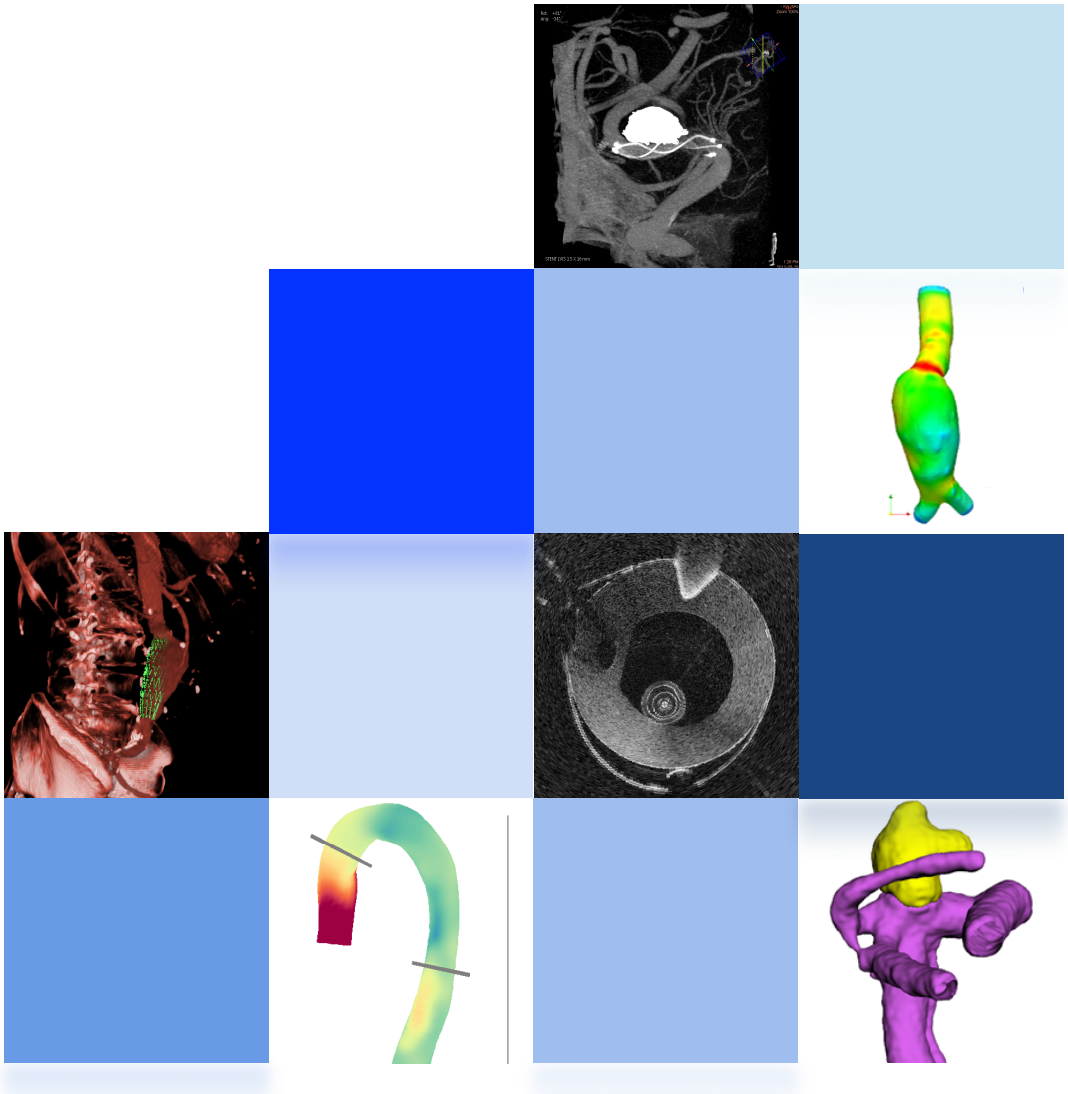

MICCAI

The MICCAI-STENT Workshop brings together researchers in the field of endovascular stenting procedures in different anatomical regions. While researchers concerned with cerebral, coronary, carotid, and aortic stenting have mostly published within their corresponding anatomy, this workshop provides a platform for scientific discussion on stent-related research across anatomical boundaries. The aim is to form the basis of a specialized subcommunity within MICCAI.

Technological advances in diagnostic and intraoperative imaging offer increasingly useful information regarding vascular anatomy and function, and are poised to have dramatic impact on the diagnosis, analysis, modeling, and treatment of vascular diseases. Computational vision techniques designed to analyze images for modeling, simulating, and visualizing anatomy and medical devices such as stents as well as the assessment of interventional procedures are therefore playing an important role and are currently receiving significant interest. In the 1st MICCAI-STENT workshop, held on October 1, 2012, in Nice, France, all aspects of this topic are addressed, and to the best of our knowledge, STENT is the only workshop dedicated to these particular aspects of stenting procedures.

Stefanie Demirci, Su-Lin Lee, Petia Radeva, Gozde Unal

Sponsored by
SIEMENS
Boston Scientific

Workshop Organizers
Stefanie Demirci, CAMP/TUM, Germany
Su-Lin Lee, Imperial College London, UK
Petia Radeva, Universitat de Barcelona, Spain
Gozde Unal, Sabanci University, Turkey

Steering-Organizing Committee
Nassir Navab, CAMP/TUM, Germany
Kevin Cleary, Childrens National Medical Center, US
Alejandro Frangi, University Pompeu-Fabra, Spain

Technical Assistants
Etibar Taghiyev, CAMP/TUM, Germany
Osman Rahmi Ficici, Sabanci University, Turkey
Timur Aksoy, Sabanci University, Turkey

Invited Speakers
Dr. Reza Ghotbi, Klinikum Muenchen Pasing, Germany

Panel Discussion
Dr. Reza Ghotbi, Klinikum Muenchen Pasing, Germany
Dr. Yunqiang Chen, Siemens Corporate Research, US
Dr. Frode Manstad-Hulaas, St Olavs Hospital, Norway
Dr. Vincent Bismuth, GE Healthcare, France

Program Committee - Technical Board
Georg Langs, Medical University Vienna, Austria
Ying Zhu, Siemens Corporate Research, US
Regis Vaillant, General Electric, France
Nenad Filipovic, University of Kragujevac, Serbia
Geir Arne Tangen, SINTEF, Norway
Ignacio Larrabide, University Pompeu-Fabra, Spain
Simone Ballocco, Universitat de Barcelona, Spain
Carlo Gatta, Universitat de Barcelona, Spain
Almar Klein, University Twente, The Netherlands

Program Committee - Medical Board
Frode Manstad-Hulaas, MD, St. Olavs Hospital, Norway
Christian Loewe, MD, Medizinische Universitat Wien, Austria
Hans-Henning Eckstein, MD, Klinikum rechts der Isar, Germany
Reza Ghotbi, MD, Kreisklinik Muenchen-Pasing, Germany
Christian Reeps, MD, Klinikum rechts der Isar, Germany
Mojtaba Sadeghi-Azandaryani, MD, Klinikum der Universitat Mnchen, Germany
Juan Rigla, MD, Boston Scientific, Spain
Colin Bicknell, MD, Imperial College London, UK

External Reviewing Committee
Amin Katouzian
Jakob Vogel
Wen Wu
Richard Brosig
Abouzar Eslami
Celia Riga
Yunqiang Chen

Contents

Influence of vascular morphology on hemodynamic changes after flow diverter placement in saccular intracranial aneurysms

Ignacio Larrabide[1,2], Arjan J. Geers[2,1], Martha L. Aguilar[2,1], Hernán G. Morales[2,1], Daniel Rufenacht[3], and Alejandro F. Frangi[2,1,4]

[1] Networking Research Center on Bioengineering, Biomaterials and Nanomedicine (CIBER-BBN), 08019 Barcelona, Spain
[2] Universitat Pompeu Fabra, c/Tanger 122-140, 08018, Barcelona, Spain
[3] Hirslanden Clinic, Zrich, Switzerland [4] Department of Mechanical Engineering, University of Sheffield, Sheffield, UK
ignacio.larrabide@upf.edu

Abstract. Flow diverter stents (FDs) are becoming widely used for the treatment of intracranial aneurysms, particularly for cases that present difficulties for other treatments such as coiling or clipping. The relationship between the surrounding vascular morphology and the effect of these devices on the changes of hemodynamic forces in the aneurysm, which has not been assessed so far, is studied in this paper. The Vascular Modeling Toolkit (VMTK) has been used for the characterization of vascular morphology. CFD simulations have been performed on untreated and virtually treated geometries of 16 saccular intracranial aneurysms. Our results indicate that distance of the aneurysm with respect to the previous curvature peak of the vessel and the angle of the aneurysm with respect to the parent vessel osculating plane are closely related to the changes of hemodynamic variables inside the aneurysm after placement of a FD.

Keywords: Intracranial aneurysm, vascular morphology, flow diverter, hemodynamics

1 Introduction

FDs are stent-like devices designed to divert the flow along the normal anatomical course of the vessel and away from the aneurysm neck and dome. These devices have shown to be most useful in cases that are difficult to treat by other means [1]. Stagnation of the flow activity in the aneurysm stimulates thrombosis and, ultimately, occlusion of the aneurysm. This process induces reverse remodeling of the aneurysm and reconstruction of the parent artery. Although animal experiments and clinical series have already shown impressive effectiveness of this technology, the effects on local hemodynamics are yet not fully understood [2]. Longer term persisting patency and delayed aneurysm ruptures have been reported in some cases after FD treatment. Still, complete angiographic occlusion

is reported in the majority of the cases [3–5]. The effectiveness of FD treatment is related to factors ranging from physiology to the blood flow mechanics [6].

Proposals have been made for quantifying the effectiveness of the treatment (e.g., porosity, permeability) [7]. In this study, we relate the vascular morphology to the reduction in hemodynamic forces in the aneurysm after flow diverter treatment. Vascular morphology is studied and quantified following methodologies proposed in previous studies [8, 9].

2 Material and Methods

Sixteen saccular aneurysms were used in this study and drawn from the @neurIST database, which was collected in different centers and processed by different observers following the same data processing protocol. All selected aneurysms were located at the supraclinoid segment of the ICA to reduce differences in parent vessel flow rate due. Anatomical models were obtained from diagnostic 3DRA images, acquired through an Integris^{TM} Allura System (Philips Healthcare, Best, The Netherlands) or an AXIOM Artis (Siemens Medical Solutions, Erlangen, Germany). Voxel sizes in the reconstructed 3D images ranged from 0.208 mm^3 to 0.378 mm^3.

Vascular extraction and geometric characterization

Images were segmented using a GAR method, and a 3D model consisting of a triangulated surface mesh was generated [10]. Triangle removal, hole filling and volume preserving optimized Laplacian smoothing were employed to remove imperfections in the vascular models. GIMIAS software was used for these operations [11]. Vascular morphology was described in terms of centerline, vessel diameter and curvature using the Vascular Modeling Toolkit (VMTK) package [9]. From the centerline, two variables were considered following the work of Piccinelli et. al [9] (Fig. 1):

- D_{pc}: distance from the aneurysm ostium location over the centerline (origin of the bifurcating branch going into the aneurysm) to the peak curvature before the aneurysm.
- a_o: angle between the aneurysm vector (vector pointing into the aneurysm of the local reference system defined in the aneurysm bifurcation) and the local osculating plane (defined form the local Frenet frame on the parent vessel at the location of the bifurcation).

Also, all vascular geometries where also characterized in terms of the length of the model l_S, defined as the length between the proximal end of the ICA visible from the model and the ICA bifurcation.

Virtual treatment and CFD analysis

Geometric models of the FDs, consisting of 48 wires of 60 μm thickness were created and deployed in the vascular models using the Fast Virtual Stenting method

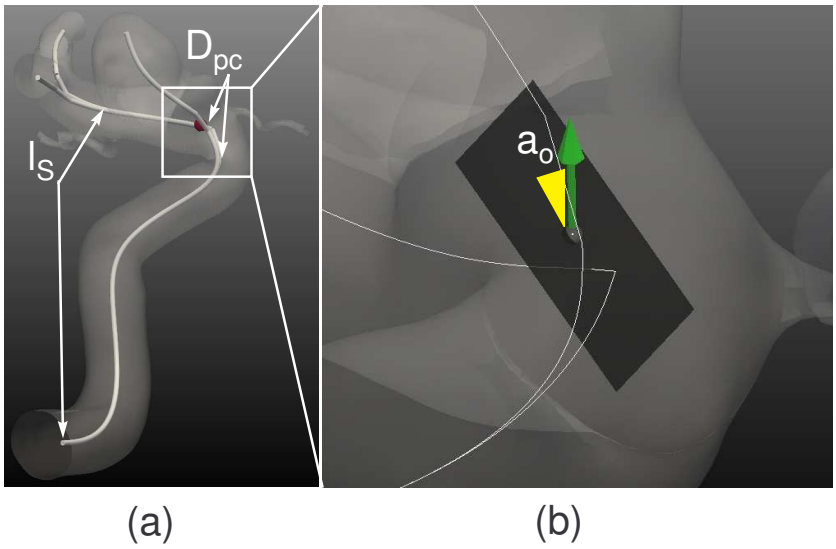

Fig. 1. (a) Graphical representation of the distance from the aneurysm neck to the curvature peak measured along the centerline. The red dot represents the location origin in the aneurysm bifurcation. (b) Angle between the osculating plane (dark gray) and the aneurysm vector (green).

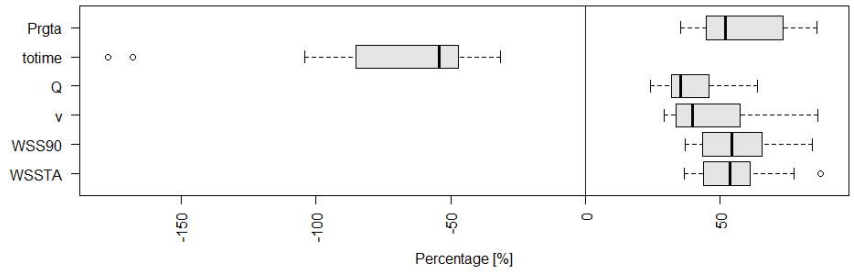

Fig. 2. Changes of hemodynamic variables measured on the aneurysm region.

[12]. Volumetric meshes were generated using the commercial software ICEM CFD, Version 11.0 (ANSYS, Canonsburg, Pennsylvania), which were composed of unstructured tetrahedral and 8-node prism elements. Mesh independent CFD solutions were obtained for meshes with 0.016 mm elements around the stent struts (i.e. approximately 12 elements along the perimeter) and maximally 0.4 mm elements in the lumen. Following the study of Appanaboyina et al. [13], portions of the stent laying on the vessel wall were removed to reduce computational time.

Transient CFD simulations for both treated and untreated geometrical models were performed with CFX, Version 11.0 (ANSYS), which uses a finite volume approach to solve the Navier-Stokes equations. Blood was modeled as an incompressible Newtonian fluid (density = 1066 kg/m^3, viscosity = 0.0035 Pa·s). The vessel wall was assumed to be rigid with no-slip boundary condition. Flow boundary conditions were derived from a 1D mathematical model of the systemic arterial tree. Flow rate waveforms were imposed at the inlet and pressure waveforms at the outlets. For the setup of the flow boundary conditions, a straight extension was added to each vascular model at the location of the inlet (upstream end). A flat velocity profile was imposed at the inlet of that extension. FOr all models, the inlet was located at the ICA. Cardiac cycles of 0.8s each were discretized in time steps of 0.005s. To remove the effect of initial transients, three complete cardiac cycles were computed and data from the last one was stored and analyzed.

Data analysis

Intra-aneurysmal hemodynamics were quantitatively analyzed using the following variables:

- Spatial-averaged wall shear stress averaged in time (WSS_{ta}) and 90^{th} percentile (WSS_{90}).
- Spatio-temporal average of velocity (v_{an}).

- Average aneurysm inflow (Q_{an}).
- Turn-over time inside the aneurysm (defined as $totime = V_{an}/Q_{an}$, with V_{an} being the aneurysm volume).
- Time-average of the aneurysm pressure range (p_{rgta}), defined as the difference between the highest and lowest pressure (in mmHg) in the aneurysm at each time point averaged over time.

These variables were recorded before and after virtual placement of the FD. The changes of each variable x was computed as:

$$x_{changes} = 100\% * (x_{untreated} - x_{treated})/x_{untreated} \quad (1)$$

A negative change indicates an effective increase of the variable and a decrease otherwise. Data analysis was performed using the R statistical package software [14]. Spearman's test was used to study correlation between the morphological variables and hemodynamics reduction. Results were considered statistically significant for $p<0.05$.

3 Results

	l_S[mm]	$D_{pc}[mm]$	a_o[degrees]
mean (SD)	49.98 (16.78)	-8.39 (5.19)	92.77 (32.83)
min	29.76	-18.50	49.60
max	86.49	-2.56	144.23

Table 1. Vascular morphological descriptors for the cases studied

Table 1 summarizes the morphological variables in terms of mean, standard deviation (SD), minimum and maximum values. The l_S went from 26.76 to 86.49mm and the average D_{pc} was 8.39mm (SD = 5.19mm). The average angle between the aneurysm and the osculating plane of the parent vessel at that location was 92.77 degrees (SD = 32.83). After FD deployment, a mean porosity of 72.8% (SD = 5.4%) was measured in all our cases.

Fig. 2 presents boxplots of the reduction in hemodynamic variables. All variables have been reduced after the placement of the FD with the exception of *totime* that consistently increased after FD placement, which renders as a negative reduction (Fig. 2). Changes in hemodynamic variables were statistically significant.

Fig. 3 presents scatter plots relating the hemodynamic and morphological variables. Regarding D_{pc}, significant correlation was found for WSS_{ta} (ρ = -0.53). Although not statistically significant, high correlation was found for Q_{an} (ρ = -0.47, p= 0.06) and *totime* (ρ = 0.41, p= 0.06). For WSS_{90}, v_{an} and p_{rgta} no significant correlation was found. This findings suggest that, the further away the aneurysm is located from the curvature peak, the higher the FD induced changes

in inflow and WSS. One possible explanation is that the further downstream we are from curvature peaks, secondary flow disappears, main flow is re-stabilized and oriented in the vessel longitudinal direction. In this condition, the FD might have a stronger influence on hemodynamic variables.

Fig. 4(a) presents the hemodynamic results for two cases that illustrate this difference. For the aneurysm far from the curvature peak, the flow into the aneurysm is largely reduced. For the aneurysm near the curvature peak, a strong vortex generated at that location progresses into the aneurysm creating a major flow stream into it. After placement of the FD, the first case presents a stronger cessation of flow motion inside the aneurysm. On the other hand, the inflow in the aneurysm near the curvature peak is not strongly affected by the presence of the FD.

When looking at a_o, significant correlations are observed for WSS_{ta} (ρ = 0.58), WSS_{90} (ρ = 0.64), v_{an} (ρ = 0.58) and p_{rgta} (ρ = 0.65). No significant correlation was found for Q_{an} (ρ = 0.26) and *totime* (ρ = -0.26). It was found that as the aneurysm angle is leaning towards the outer side of the bend ($a_o > 90°$), the relative reduction of hemodynamic variables is larger. In such geometrical condition, the changes induced by the presence of a FD have a stronger effect on hemodynamic changes is higher. Fig. 4(b) presents hemodynamic results for two exemplary cases, one where the aneurysm between the aneurysm and the osculating plane is wide (top) and another with a narrow angle (bottom). We observe for the case on the top (wide angle) that the part of the main flow jet going into the aneurysm is small and the presence of a FD redirects the flow to the parent vessel. When the angle between the aneurysm and the osculating plane is narrow (bottom) the presence of the FD induces smaller changes in the local flow.

In the present work, we make use and extend previous work by Piccinelli et al. [8] by looking at the effect of FDs in relation to vascular morphology. In this way, we provide a link which has not been assessed before. Still, further work is required to set the basis for such studies and their future use in clinical practice.

One limitation of this work is that is only based on simulation results and not on experimental or clinical observations. Nevertheless, special care has been put on the extraction of the anatomical models to ensure their fidelity (by using state-of-the-art image analysis techniques) and on the boundary conditions chosen (ensuring realistic flow conditions in all models). In this way, we expect that the results reported by the models are, at least, within physiological ranges.

4 Conclusions

In this study we investigated the effect vascular morphology on hemodynamics after FD. CFD simulations were performed before and after virtual placement of the FD. We found that time-averaged WSS is more reduced in aneurysms far away from the curvature peak. This larger reduction is attributed to that secondary flow is reduced further downstream from the curvature peak. This is reflected by the high correlation observed between D_{pc} and Q_{an}. We also

observed high correlations with statistical significance for reduction of WSS, velocity and pressure range in the aneurysm with respect to the angle between the local osculating plane and the aneurysm. Local hemodynamics are largely affected by the incidence angle of the aneurysm, which strongly influences the direction the aneurysm inflow jet angle.

The hemodynamic variable reduction can be correlated to vascular morphology nearby the aneurysm. Still, to provide proper predictive estimations of flow in complex vascular geometries, a deeper understanding of the relationship between geometry and hemodynamics is fundamental.

Acknowledgements

This research has been partially funded by the Industrial and Technological Development Center(CDTI) under the CENIT-CDTEAM and CENIT-cvREMOD programs, the European Commissions project @neurIST (IST-2005-027703) and Philips Healthcare (Best, The Netherlands), and from the Catalonian Department of Innovation, Universities and Enterprise (DIUE), through the EndoTreat project (exp. VALOR2010-00064).

References

1. Nelson, P.K., Lylyk, P., Szikora, I., Wetzel, S.G., Wanke, I., Fiorella, D.: The pipeline embolization device for the intracranial treatment of aneurysms trial. AJNR. American journal of neuroradiology **32**(1) (January 2011) 34–40
2. Sadasivan, C., Lieber, B.B., Gounis, M.J., Lopes, D.K., Hopkins, L.N.: Angiographic quantification of contrast medium washout from cerebral aneurysms after stent placement. AJNR. American journal of neuroradiology **23**(7) (August 2002) 1214–21
3. Cebral, J.R., Mut, F., Raschi, M., Scrivano, E., Ceratto, R., Lylyk, P., Putman, C.M.: Aneurysm Rupture Following Treatment with Flow-Diverting Stents: Computational Hemodynamics Analysis of Treatment. AJNR. American journal of neuroradiology (November 2010) 1–7
4. Kulcsár, Z., Houdart, E., Bonafé, A., Parker, G., Millar, J., Goddard, a.J.P., Renowden, S., Gál, G., Turowski, B., Mitchell, K., Gray, F., Rodriguez, M., van den Berg, R., Gruber, A., Desal, H., Wanke, I., Rüfenacht, D.a.: Intra-Aneurysmal Thrombosis as a Possible Cause of Delayed Aneurysm Rupture after Flow-Diversion Treatment. AJNR. American journal of neuroradiology **23**(1) (November 2010) 20–25
5. Klisch, J., Turk, a., Turner, R., Woo, H.H., Fiorella, D.: Very late thrombosis of flow-diverting constructs after the treatment of large fusiform posterior circulation aneurysms. AJNR. American journal of neuroradiology **32**(4) (April 2011) 627–32
6. Lieber, B.B., Sadasivan, C.: Endoluminal scaffolds for vascular reconstruction and exclusion of aneurysms from the cerebral circulation. Stroke; a journal of cerebral circulation **41**(10 Suppl) (October 2010) S21–5
7. Sadasivan, C., Cesar, L., Seong, J., Wakhloo, A.K., Lieber, B.B.: Treatment of rabbit elastase-induced aneurysm models by flow diverters: development of quantifiable indexes of device performance using digital subtraction angiography. IEEE transactions on medical imaging **28**(7) (July 2009) 1117–25

8. Piccinelli, M., Bacigaluppi, S., Boccardi, E., Ene-Iordache, B., Remuzzi, A., Veneziani, A., Antiga, L.: Geometry of the internal carotid artery and recurrent patterns in location, orientation and rupture status of lateral aneurysms: an image-based computational study. Neurosurgery **68**(5) (January 2011) 1270–1285
9. Piccinelli, M., Veneziani, A., Steinman, D.a., Remuzzi, A., Antiga, L.: A framework for geometric analysis of vascular structures: application to cerebral aneurysms. IEEE transactions on medical imaging **28**(8) (August 2009) 1141–55
10. Hernandez, M., Frangi, A.F.: Non-parametric geodesic active regions: method and evaluation for cerebral aneurysms segmentation in 3DRA and CTA. Medical image analysis **11**(3) (June 2007) 224–41
11. Larrabide, I., Omedas, P., Martelli, Y., Planes, X., Nieber, M., Moya, J.A., Butakoff, C., Sebastián, R., Camara, O., de Craene, M., Bijnens, B.H., Frangi, A.F.: GIMIAS: An open source framework for efficient development of research tools and clinical prototypes. In: Functional Imaging and Modeling of the Heart. Volume 5528/2009 of Lecture Notes in Computer Science. (2009) 417–426
12. Larrabide, I., Kim, M., Augsburger, L., Villa-Uriol, M.C., Rüfenacht, D., Frangi, A.F.: Fast virtual deployment of self-expandable stents: Method and in vitro evaluation for intracranial aneurysmal stenting. Medical image analysis (May 2010)
13. Appanaboyina, S., Mut, F., Löhner, R., Putman, C., Cebral, J.: Simulation of intracranial aneurysm stenting: Techniques and challenges. Computer Methods in Applied Mechanics and Engineering **198**(45-46) (2009) 3567–3582
14. Team, R.D.C.: R: A Language and Environment for Statistical Computing (2008)

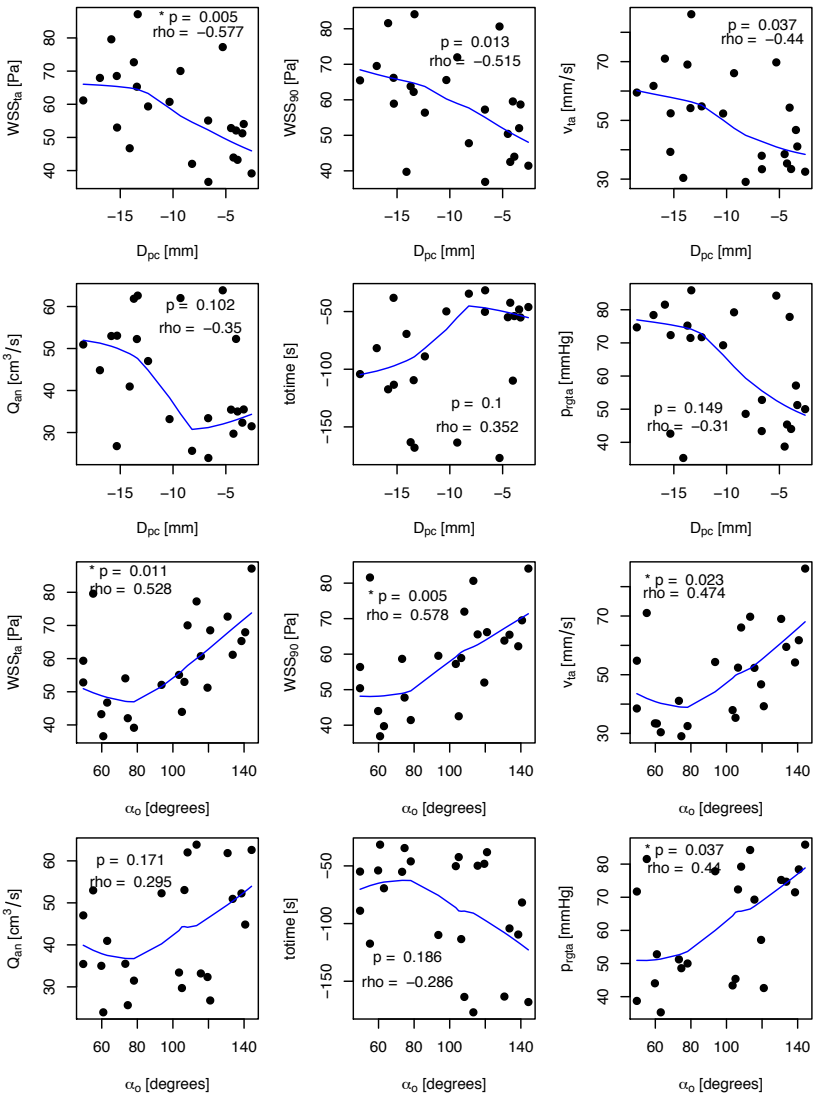

Fig. 3. Scatter plots for the relation between morphological and hemodynamic variables studied. Also, locally-weighted polynomial (blue) regression is shown for each plot.

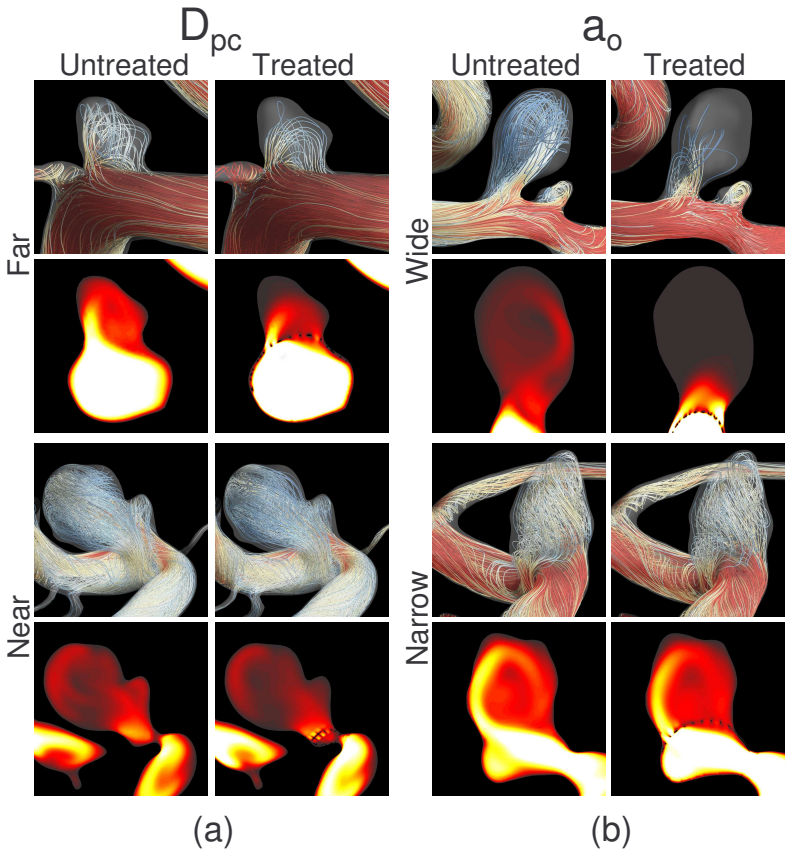

Fig. 4. Qualitative hemodynamic simulations results for four selected cases are presented. Each group of images presents streamlines (top), velocity magnitude on a cross section plane across the aneurysm (bottom), untreated (left) and treated (right). (a) Two cases with extreme values of D_{pc} and on the right two extreme cases for a_o. On the left, the one on the top is an aneurysm laying far from the curvature peak (high D_{pc}) and on the one the bottom is very near to the peak (low D_{pc}). (b) The one on top presents a wide angle with respect to the osculating plane (high a_o) and the one on the bottom has a narrow angle with respect to it (low a_o).

Towards Predicting the Effects of Stent-Grafting on the Motion of the Thoracic Aorta*

Ernst Schwartz[1], Johannes Holfeld[2], Martin Czerny[3], Christian Loewe[4], and Georg Langs[1]

[1] CIR Lab, Department of Radiology, Medical University of Vienna
[2] Department of Cardiac Surgery, Innsbruck Medical University
[3] Department of Cardiovascular Surgery, Bern University Hospital
[4] Department of Radiology, Medical University of Vienna

Abstract. The Thoracic Aorta is a highly dynamic vessel. Changes induced to vessel motion due to procedures such as stent-grafting are hypothesized to play a significant role in the outcome of interventions. A priori knowledge about these effects is difficult to establish due to numerous unknown factors influencing the prognosis. We propose a framework that learns typical changes to vessel wall motion induced by interventions from a set of pre- and post-intervention sequence pairs, and a large set of single sequences. The method uses a combined model of vessel shape, -motion, and stent location to predict post intervention deformation from pre-intervention sequence. Experimental results illustrate the influence of the individual regressors on the prediction accuracy. They indicate that prediction is feasible.

Keywords: Vascular, Aorta, Modeling, Prediction, Treatment planning, Stent-grafting

1 Introduction

The complex topology of the vasculature in the Aortic Arch and its strong movement related to myocardial motion makes the treatment of pathologies in the thoracic aorta a challenging procedure in vascular surgery. Supra-aortic branch transposition [1] followed by stent-grafting has recently been proposed as a promising treatment option. However, the insertion of a stent-graft in this highly dynamic region of the aorta affects the morphological and dynamic properties of the vessel [2]. These changes have been hypothesized to lead to elevated local stress on the vessel wall and in turn to adverse prognosis on the outcome of endovascular interventions [3, 4]. In order to support clinicians in treatment planning, we propose a method to predict movement-related stress in the Thoracic Aorta after the intervention from pre-intervention data. We base our analysis on ECG-gated Computed Tomography Angiography (CTA) sequences as this

* This work was partially funded by the OeNB (13497 AORTAMOTION), EU (257528 KHRESMOI), and Austrian Science Fund FWF (22578-B19 PULMARCH)

modality allows for the extraction of both dynamic and static properties of the aorta.

The remainder of the paper is organized as follows. First, we describe the methods used to extract deformation fields and surface segmentations from the CTA data in Section 2. We use this information in Section 3 to obtain a discriminative description of the global shape of the Thoracic Aorta. Together with pre-intervention shape and motion parameters, these parameters are used to build a regression model of vessel motion after intervention. This is described in Section 4. We present results for a predictive model of stent-grafting procedures in Section 5. Finally, a discussion of open questions and future research directions concludes the paper in Section 6.

2 Preprocessing

The proposed method is based on ECG-gated CTA data [3] whose original voxel size of 0.67 x 0.67 x 0.33 mm is resampled to isotropy of 1mm. We found this resolution to be a reasonable compromise between the level of detail of the analysis and the required processing time. Each acquisition consists of a series $\mathbf{S} = (\mathbf{V}_1, ...\mathbf{V}_T)$ of volumes $\mathbf{V}_t$ representing the thorax of the patients at breath-hold during one cardiac cycle. Registration and segmentation procedures are then applied to the sequence in order to extract dynamic models of the Thoracic Aorta $\mathcal{A}$.

3D+t Registration Group-wise temporal b-spline registration [5] is performed on each CTA sequence to extract myocardial and induced vascular motion. The result of the registration $\mathcal{R}$ is a sequence of vector fields matching each volume $\mathbf{V}_t$ to a hypothetical mean volume. We exploit the fact that the time-point in the cardiac cycle corresponding the first frame in $\mathbf{S}$ is known from the ECG-signal. We resample the displacement fields to yield $\mathcal{R}(\mathbf{S}) = (\mathbf{D}_1, ..., \mathbf{D}_T)$, a smooth sequence of dense vector fields $\mathbf{D}$ each mapping $\mathbf{V}_{t=1...T}$ to $\mathbf{V}_1$. These vector fields can be interpolated at a given position $\mathbf{v}$ and a series of time points t to yield trajectories of this location during the cardiac cycle as $\mathbf{d}(\mathbf{v}, t) = \mathbf{D}_t(\mathbf{v}), \mathbf{v} \in \mathbb{R}^3, t \in [0...T]$.

Segmentation We compute the mean volume $\overline{\mathbf{V}}_{\mathcal{A}} = \frac{1}{T}\sum_{t=1}^{T} \mathbf{V}_t(\mathbf{D}_t^{-1}(x))$ of a sequence which we segment using a tracking-based approach similar to [6]. We represent the resulting segmentation $\mathcal{S}(\overline{\mathbf{V}}_{\mathcal{A}})$ of the aorta as an estimate of the vessel centerline C and the radially sampled surface point parameterization R

$$\begin{aligned} \mathcal{S}(\overline{\mathbf{V}}_{\mathcal{A}}) \ni \mathbf{v}(s,\theta) = C(s) + R(s,\theta)\boldsymbol{n} \\ s \in [0...1] \ , \ \theta \in [0...2\pi[\ , \ \boldsymbol{n} \cdot dC(s) = 0 \end{aligned} \tag{1}$$

The positioning of surface points in consecutive orthogonal planes of the centerline is optimized to minimize radial drift, resulting in a smooth surface model.

3 Automated Shape-Model Construction

We expect both local and global geometric properties of the vessel to influence the outcome of vascular interventions. In order to encode global properties of the shape of each aorta in the population, we propose to build a low-dimensional representation of the surface models $\mathcal{S}(\mathcal{A}_n), n = 1...N$ using a Statistical Shape Model (SSM) [7].

3.1 Shape Alignment

To align all centerlines C_n in the population, we translate each to the center of its Aortic Arch and assume the closest points $C_n(s = c_n)$ on the centerline to correspond across subjects. The remainders $C_n(s > c_n),\ s \leq 1$ and $C_n(s < c_n),\ s \geq 0$ are resampled to ensure complete overlap. This alignment procedure establishes correspondences among all centerlines $C_n(s)$ of the model population so that $C_i(s) \leftrightarrow C_j(s)\ \ \forall i, j \in [1...N]\ ,\ s \in [0...1]$

3.2 Model construction

We construct the mean centerline $\overline{C} = \frac{1}{N}\sum_{n=1}^{N} C_{\mathcal{A}_n}$ and a linear shape model $C_{\mathcal{A}_n} \approx \overline{C} + \mathbf{\Psi}^{(C)}\boldsymbol{\lambda}_{\mathcal{A}_n}^{(C)}$ for the population of centerlines using PCA, where $\mathbf{\Psi}^{(C)}$ is the eigendecomposition of the covariance matrix of all $C_{\mathcal{A}_n}$ and $\lambda_{\mathcal{A}_n}^{(C)}$ the corresponding modes of variation for a specific aorta $\mathcal{A}_n$.
Because radial correspondences can be assumed as explained in Section 2, we model the radial component R in identical fashion as $R_{\mathcal{A}_n} \approx \overline{R} + \mathbf{\Psi}^{(R)}\boldsymbol{\lambda}_{\mathcal{A}_n}^{(R)}$ where $\overline{R} = \frac{1}{N}\sum_{n=1}^{N} R_{\mathcal{A}_n}$.

In each of the two shape models, we retain the coefficients that explain 95% of the total shape variability in the population. The shape of each aorta $\mathcal{A}_n$ in the population can then be represented as two low-dimensional sets of coefficients $\boldsymbol{\lambda}_{\mathcal{A}_n}^{(C)} \in \mathbb{R}^8$ and $\boldsymbol{\lambda}_{\mathcal{A}_n}^{(R)} \in \mathbb{R}^{26}$ of these shape models.

4 Predicting the Effects of Stent-Grafting

In the previous section, we described how to encode the shape of the aorta in a low-dimensional representation. We will now use these global shape descriptors, as well additional local properties of the aorta before intervention in a regression model to predict its motion after stent-grafting.

4.1 Parameters affecting treatment outcome

We expect three main factors to predict the outcome of endovascular interventions: the shape of the affected vessel, its dynamics before the procedure and the location of the stent-graft. We use the coefficients of the shape model as descriptors of its overall shape, and local features to represent morphological details of each case.

Global shape information The global shape of every $\mathcal{S}(\mathcal{A}_n)$ is encoded using an SSM computed from 54 CTA sequences as described in Sec. 3. The coefficients $\boldsymbol{\lambda}_{\mathcal{A}_n}^{(C)}$ represent the shape of the centerline before the intervention. The coefficients $\boldsymbol{\lambda}_{\mathcal{A}_n}^{(R)}$ encode the mode of radial displacement from the centerline. Concatenating these results in the global shape feature vector $\mathbf{f}_{\text{globalshape}}(\mathcal{A}_n) \in \mathbb{R}^{34}$.

Local shape information For each $\mathbf{v} \in \mathcal{S}(\mathcal{A}_n)$, we compute the surface curvature in terms of its minimum, maximum, mean and gaussian components. Additionally, the distance of each $\mathbf{v}$ to the centerline C and a local estimate of vessel radius are computed. Finally, we compute a shape signature of $\mathcal{S}(\mathcal{A}_n)$ as proposed in [8]. This representation encodes local geometric information at each point in the feature vector $\mathbf{f}_{\text{localshape}}(\mathbf{v}) \in \mathbb{R}^{27}$.

Location relative to stent-graft The location of a stent graft is indicated as a binary variable for each $\mathbf{v}$. In cases where a stent-graft is present, we also compute the distance between every point outside the stent graft and its distal ends which we store as $\mathbf{f}_{\text{stent}}(\mathbf{v}) \in \mathbb{R}^3$.

Motion properties Common methods of describing vascular motions rely on aggregate values for cross-sectional regions of the vessel [9]. However, we expect the changes of vessel movement to be more unevenly distributed. Therefore, we estimate the motion of the aorta on the complete vessel surface represented by $\mathbf{v}$ by interpolating and concatenating the displacement fields $\mathbf{D}_t$. From these raw motion trajectories, we compute information about the Total Distance Travelled (TDT) as $\text{TDT}(\mathbf{v})_{\mathcal{A}} = \int \frac{\partial \mathbf{d}(\mathbf{v},t)}{\partial t} dt$. Furthermore, we compute the maximum distance travelled between two time points and the standard deviation of distances travelled. In order to to include more contextual information about vessel movement in the model, we aggregate information about cross-sections of the vessel. We compute mean and maximum TDT as well as the standard deviation in TDT in each cross-section $C(s)$. In order to reduce the influence of patient condition at the time of acquisition, we normalize each of these values to the interval [0...1]. This results in the local motion features $\mathbf{f}_{\text{motion}}(\mathbf{v}) \in \mathbb{R}^8$.

4.2 Regression Model

Estimating the way in which an intervention affects the motion of the aorta is a highly non-linear and underdetermined problem. We therefore use the recently proposed ensemble-method of Random Forest Regression [10] for model learning. Furthermore, due to limited amount of training data, we aim at predicting TDT instead of the complete vessel movement. We limit the space of training vectors according to a rejection procedure, detailed below.

Random Forests Random Forest Regression is a popular non-linear regression method based on a bootstrapping approach [11]. It uses a series of regression trees that are built from random subsamplings of the training data instances.

The accuracy of each tree is tested based on the remainder of the training set. By computing the average vote of all trees in the forest, regression can be performed on unseen data.

Outlier Removal The effects of stent-grafting in the Aortic Arch are highly non-linear and can vary widely from patient to patient [2]. To reduce the effects of local spurs of aortic motion in single patient we removed all $\mathbf{v}$ from the training set whose TDT was 3 standard deviations larger than the mean in each case. We retained all $\mathbf{v}$ located in the Ascending Aorta, as strong movement in that part of the anatomy is expected.

Prediction model For each surface model point observed before stent-grafting $\mathbf{v} \in \mathcal{S}(\mathcal{A}_{\text{pre}})$ we concatenate the previously described features to form a 75-dimensional feature vector $\mathbf{f}(\mathbf{v})$. Using Random Forests, we learn a regression model $\mathfrak{R}_{\text{RF}}$ between these features and the motion of the Thoracic Aorta $\mathcal{A}_{\text{post}}$ as

$$\text{TDT}(\mathbf{v}') \approx \mathfrak{R}_{\text{RF}}(\mathbf{f}(\mathbf{v})) \ , \ \mathbf{v} \in \mathcal{S}(\mathcal{A}_{\text{pre}}) \ , \ \mathbf{v}' \in \mathcal{S}(\mathcal{A}_{\text{post}}) \tag{2}$$

5 Results

We applied the proposed model learning method to a set of 4 cases where stent-grafting in the Aortic Arch was performed after supra-aortic rerouting [1]. We perform Leave-One-Out Cross Validation (LOOCV), learn a model from 3 cases and apply it to predict post-intervention motion from pre-intervention feature vectors for the fourth case. We present the results in Figure 3. Subfigure a) shows the TDT of the aorta before the intervention, b) the prediction of TDT using the presented regression model and c) the real measured TDT. As the distribution of values of TDT are skewed due to the strong movement of the AA, we limit the color-coding at +3 standard deviations TDT in each case.

5.1 Importance of model parameters

During regression Random Forests compute the Gini importance score of each parameter in the feature vectors used for training. Figure 2 shows the feature importance in the 4 LOOCV runs we performed. As expected, the most relevant feature for predicting post-intervention TDT changes is the position of the observed sampling point $\mathbf{v}$ on the centerline. The second-most important factor in the 4 observed cases is the distance of the observed point to the stent in the Ascending Aorta, which stems from the strong motion in that part of the vessel. Changes in motion seem further to be strongly influenced by the motion before the intervention, most notably the mean displacement of the corresponding orthogonal plane. According to our experiments, the local shape of the vessel plays a lesser but still significant role in the outcome of the intervention. The information contained in the first 3 components of the spectral signature shows the highest importance of the local shape parameters. Finally, the global shape of the vessel encoded in the parameters of the shape model seems to have no influence on the motion of the Thoracic Aorta after stent-grafting.

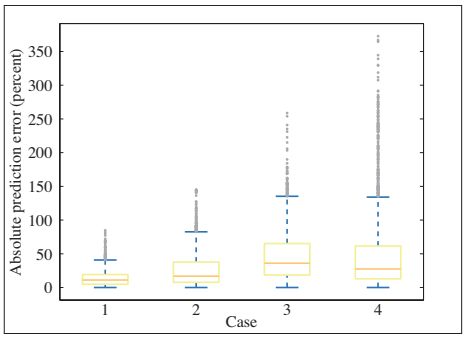

Fig. 1: Prediction error

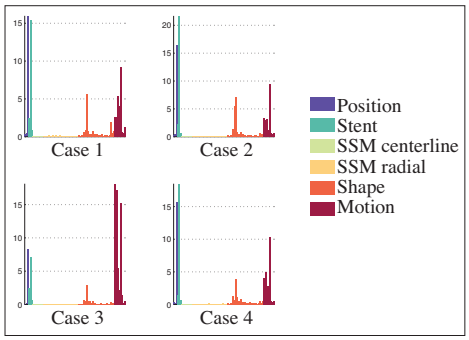

Fig. 2: Feature Importance

5.2 Model accuracy

We evaluate the accuracy of the proposed model of stent-grafting in the Thoracic Aorta in 4 cases with LOOCV. Illustrative plots of the pre-interventional, estimated and post-interventional values of TDT are shown in Figure 3. We computed the prediction error in percent of the absolute values of the change after intervention calculated with the proposed regression model. The mean error over all cases was 32.19%. The mean median error lies at 21.91%, with a mean standard deviation of 29.83%. Figure 1 shows a detailed graph of these results.

5.3 Effects of stent-grafting

By visual inspection of the cases in figure 3, the influence of stent-grafting on the motion of the Thoracic Aorta become apparent. As could be expected due to its closeness to the aortic valve and thus the heart, the strongest vessel movement can be observed in the Ascending Aorta. As previous results indicated [6], introduction of a stent-graft generally reduces the motion in the affected area. In the observed cases, the TDT of the stented area (indicated by the horizontal grey lines in each figure) decreased by 0.96mm on average while the overall decrease was of only 0.5mm. As we previously reported [12], another measurable effect of stent-grafting is the homogenization of the movement in the affected area. In the 4 cases we investigated, the standard deviation in TDT in the stented part of the vessels decreased an average of 1.5mm. However, this effect is not consistent over all cases. Notably, at -0.045mm and $+0.004$mm, the changes in standard deviation in TDT in cases 1 and 2 is negligible. Cases 3 and 4 however show significant changes of $+0.37$mm and -0.5mm respectively. We explain the poorer performance of our prediction model in cases 3 and 4 (at mean error rates of 46% and 49% compared to 14% and 26% in cases 1 and 2) with these large variations in TDT. In these cases, the stent-grafting procedure seems to have led to considerable changes in the homogeneity of the vessel movement that could not be learnt by the proposed method based on the small amount of training data available.

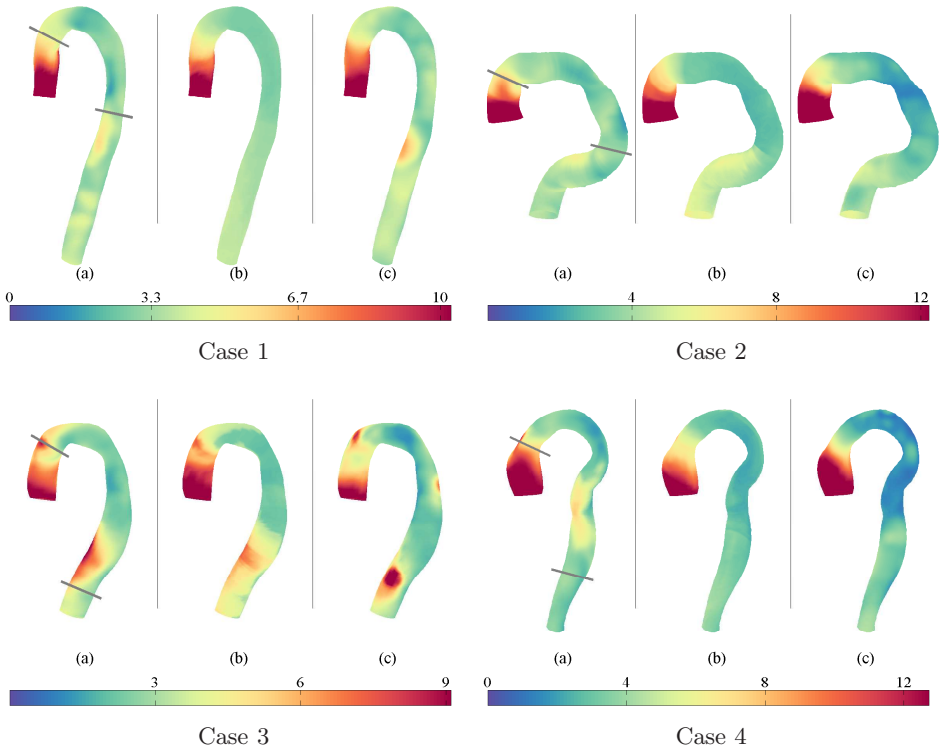

Fig. 3: (a) pre-intervention, (b) predicted post-intervention, and (c) measured post-intervention TDT in mm. Lines indicate the position of the stent-graft.

6 Discussion

In this paper, we present a method that predicts the effects of stent-grafting in the Aortic Arch on the motion of the thoracic aorta. From a set of dynamic surface models, we extract salient features describing local and global vessel shape as well as the motion of the vessel before the intervention. We apply Random Forest Regression to learn a model of the total distance travelled for each point on the surface of the vessel based on these features. We evaluate the proposed method on 4 cases where stent-grafting has been performed after supra-aortic branch transposition.

As previous work [12] indicated, subtle differences in the shape of the stented part of the vessel as well as the location of the prosthesis in the aorta can lead to large variations in the homogeneity of vascular movement after the intervention. Analysis of the error rates on the 4 observed cases confirms these results, as it correlates with the deviation in vascular movement.

Feature importance scores indicate that global shape features seem to have negligible influence on the effects of the stent-grafting procedure when compared

to a priori movement and local geometry of the vessel. In the future, we plan on assessing the locality of vascular movement in more detail. We expect that investigating the interaction between global and local shape features on larger datasets as well as their correlation with vascular movement will lead to a deeper understanding of the relevance of specific geometric properties of the aorta in terms of development and treatment of vascular diseases.

References

1. Gottardi, R., Funovics, M., Eggers, N., Hirner, A., Dorfmeister, M., Holfeld, J., Zimpfer, D., Schoder, M., Donas, K., Weigang, E., Lammer, J., Grimm, M., Czerny, M.: Supra-aortic transposition for combined vascular and endovascular repair of aortic arch pathology. Ann Thorac Surg **86**(5) (Nov 2008) 1524–9
2. van Prehn, J., Bartels, L.W., Mestres, G., Vincken, K.L., Prokop, M., Verhagen, H.J.M., Moll, F.L., van Herwaarden, J.A.: Dynamic aortic changes in patients with thoracic aortic aneurysms evaluated with electrocardiography-triggered computed tomographic angiography before and after thoracic endovascular aneurysm repair: Preliminary results. Annals of Vascular Surgery **23**(3) (Jun 2009) 291–297
3. Muhs, B., Vincken, K., van Prehn, J., Stone, M., Bartels, L., Prokop, M., Moll, F., Verhagen, H.: Dynamic cine-ct angiography for the evaluation of the thoracic aorta; insight in dynamic changes with implications for thoracic endograft treatment. European journal of vascular and endovascular surgery **32**(5) (2006) 532–536
4. Figueroa, C., Taylor, C., Yeh, V., Chiou, A., Gorrepati, M., Zarins, C.: Preliminary 3d computational analysis of the relationship between aortic displacement force and direction of endograft movement. Journal of vascular surgery **51**(6) (2010) 1488–1497
5. Metz, C.T., Klein, S., Schaap, M., van Walsum, T., Niessen, W.J.: Nonrigid registration of dynamic medical imaging data using nd+t b-splines and a groupwise optimization approach. Medical Image Analysis (Nov 2010) 1–12
6. Schwartz, E., Gottardi, R., Holfeld, J., Loewe, C., Czerny, M., Langs, G.: Evaluating deformation patterns of the thoracic aorta in gated cta sequences. Biomedical Imaging: From Nano to Macro, 2010 IEEE International Symposium on (2010) 21–24
7. Heimann, T., Meinzer, H.P.: Statistical shape models for 3d medical image segmentation: A review. Medical Image Analysis **13**(4) (Aug 2009) 543–563
8. Jain, V., Zhang, H.: A spectral approach to shape-based retrieval of articulated 3d models. Computer-Aided Design **39**(5) (2007) 398–407
9. Choi, G., Cheng, C.P., Wilson, N.M., Taylor, C.A.: Methods for quantifying three-dimensional deformation of arteries due to pulsatile and nonpulsatile forces: Implications for the design of stents and stent grafts. Ann Biomed Eng **37**(1) (Jan 2009) 14–33
10. Breiman, L.: Random forests. Machine Learning **45**(1) (2001) 5–32
11. Liaw, A., Wiener, M.: Classification and regression by randomforest. R News 2 **3** (2002) 18–22
12. Schwartz, E., Holfeld, J., Czerny, M., Langs, G.: Visualizing changes in vessel wall dynamics due to stent-grafting in the aortic arch. Biomedical Imaging: From Nano to Macro, 2012 IEEE International Symposium on (2012) to appear

Model-based Postoperative Modeling of Stent-Based Devices from CT: Application to TAVI

Ingmar Voigt[1,2], Etienne Assoumou Mengue[1,2], Razvan Ionasec[1], Tommaso Mansi[1], Dominik Bernhardt[3], Bogdan Georgescu[1], Joachim Hornegger[2], and Dorin Comaniciu[1]

[1] Imaging and Computer Vision, Siemens Corporate Research, Princeton, USA
[2] Pattern Recognition Lab, Friedrich-Alexander-University, Erlangen, Germany
[3] Clinical Applications Design and Algorithm Predevelopment, H IM CR R&D PA A, Siemens Healtcare, Forchheim, Germany

Abstract. As cardiac minimally invasive interventions are progressively substituting conventional surgical procedures, a constantly increasing number of stent-base devices are being implanted. Hence, tools for post-operative assessment and monitoring, which can provide a high-level of information about in-vivo structural and mechanical characteristics of devices, are becoming essential. We propose a novel method to automatically extract a model of stent-based implants from 3D CT volumes that combines data-driven machine learning methods with physicallly geometrical constraints. The Marginal Space Learning framework is used to estimate the position of a stent from an input cardiac image. A robust detector is introduced, which localizes stent struts crossing from an unfolded volumetric representation parameterized by the local coordinate system of the detected device. The model of a stent-frame is determined by computing its realistic deformation subject to internal forces that emulate mechanical behavior. The method was evaluated on post-operative CT volumes of 28 patients that received CoreValve devices during TAVI procedures. Results demonstrated a speed of 10.2 second per volume and average accuracy of 1.27 mm.

1 Introduction

Last decade has seen a tremendous development of minimally invasive techniques and interventional procedures for cardiac treatment substituting conventional open-heart surgery. An immediate effect of this global trend is a constantly increasing number of implanted devices in lieu of surgical repairs and sutured prosthesis. Hence, the postoperative assessment and monitoring of devices as well as a better understanding of their motion characteristics and in vivo behavior has become essential.

Inaccurate deployment can result in poor hemodynamic performance with severe paravalvular leakages and/or high gradients of pressure and suboptimal effective orifice. Wrong implant sizing may require re-operation or can damage

the vessel tissue and cause catastrophic events as arterial dissection or rupture. A misplaced implant, for instance in the aortic valve, can block the coronary ostia, thus inducing a life threatening ischemic condition. Long term stress during the life time of the implant may cause defects in the device and necessitates periodic evaluation [1]. Therefore, a model that captures a high level of information about a stent-based device would be valuable to analyze and gain insights into its in vivo behavior.

Several methods have been proposed for the segmentation of the wire frame of the stent grafts from CT data, which further underlines the importance for assessment tools for stent-based devices. Recently in a work by Lang et al. [2], the stent's frame is found using a statistical model by simultaneously learning structural and shape information from a training set. In Klein et al. [3], graph processing is proposed to determine connections between seed points and further refine the segmentation output for the stent in the form of an undirected graph. Since these methods are purely data-driven, performance may suffer in the presence of noise and motion artifacts as well as calcifications.

We propose a novel method to automatically extract a model of stent-frames from 3D CT volumes, which combines data-driven statistical methods with physically-meaningful geometrical constraints. We specifically address an emerging procedure of high-interest, namely the Transcatheter Valve Interventions (TAVI), performed using a Medtronic CoreValve Device (Minneapolis, MN, USA) [4]. In a first step, the device type and global position are computed using the Marginal Space Learning framework. A robust learning-based algorithm is introduced to estimate the probability of strut crossing points in an unfolded volumetric representation of device parameterized by cylindrical coordinates. The final parameters of the stent-frame are determined by computing its realistic deformation subject to internal forces that mimic the mechanical behavior of the device. The proposed method was evaluated on 28 post-operative CT volumes of CoreValve TAVI procedures demonstrating an average accuracy of 1.27 mm and a speed of 10.2 second per volume.

2 Methodology

The process of estimating a personalized model is divided in three stages (Fig 1) that combine the discriminative power of machine learning approaches with the prior knowledge about the device and its geometrical properties: *i)* estimation of global rigid parameters, *ii)* identification of stent strut crossing locations and *iii)* model-based fitting. While the method is generic enough to be applied to other device types, this work focuses without loss of generality on two types of implants of the CoreValve Revalving System by Medtronic (Minneapolis, MN, USA), which are the models CRS-P3-640 and CRS-P3-943.

2.1 Estimation of Global Rigid Parameters

In this step the global position parameters

$$\Phi = \{(C_x, C_y, C_z), (\alpha_x, \alpha_y, \alpha_z), (S_x, S_y, S_z)\} \quad (1)$$

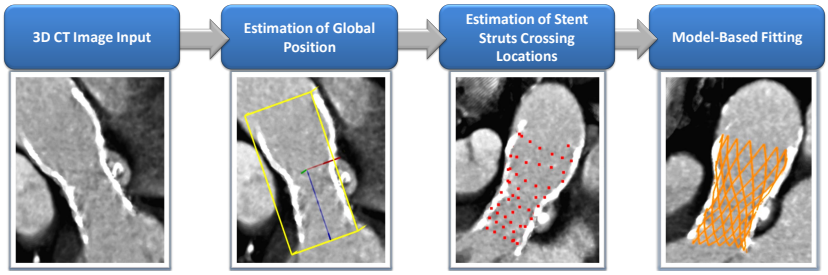

Fig. 1. Diagram depicting the personalized model estimation. See text for details.

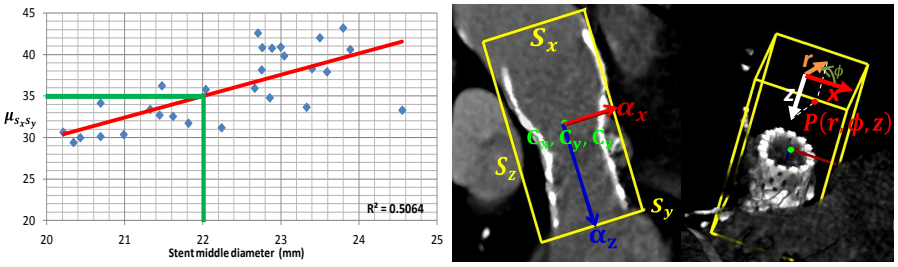

(a) (b)

Fig. 2. (a) Diagram showing the correlation function between the middle diameter of the stent and the average μ_{S_x,S_y} of the bounding box size S_x and S_y measured in mm, the regression line (**red line**) and its R-Squared value, (b) Cylindrical coordinate system using the estimated parameters Φ

are estimated defining a bounding box around the stent device, where (C_x, C_y, C_z), $(\alpha_x, \alpha_y, \alpha_z)$, (S_x, S_y, S_z) are the position, orientation and scale parameters respectively, and the type $T_1 = CRS-P3-640, T_2 = CRS-P3-943$ of a device from an input CT volume I. A probabilistic boosting tree (PBT) with Haar-like features [5] is trained to estimate the posterior probability $p(\Phi|I)$. The optimal parameters of Φ are then determined by efficiently scanning the search space using Marginal Space Learning [6].

The variation between the two devices addressed in this work is mainly characterized by a difference in the smallest diameter and height when completely expanded: 22/55mm and 24/53mm for the CRS-P3-640 and CRS-P3-943, respectively. Knowing that the diameter of CRS-P3-640 cannot be larger than 22 mm. A linear regression model (Fig 2(a)) can be used to estimate the device type directly from the global size parameters S_x and S_y and the measured smallest diameter. The device type T is determined based on $\mu_{S_x,S_y} = (S_x + S_y)/2$, where $T = T_1$ if $\mu_{S_x,S_y} < 35mm$ and $T = T_2$ otherwise.

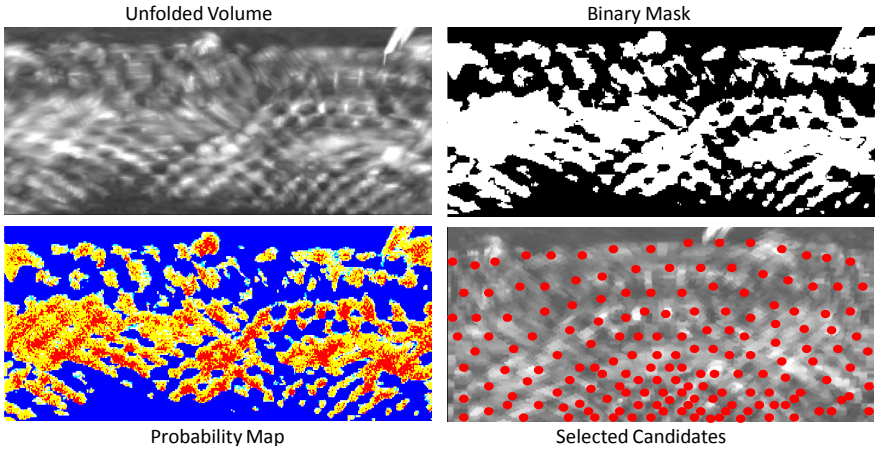

Fig. 3. Top Left: The unfolded volume in cylindrical coordinate. **Top Right:** The binary mask used to constrain the generation of positive and negative samples. **Bottom Left:** The output probably map for the strut apex detector. **Bottom Right:** The unfolded volume including the selected top candidates. Please note that for illustration purposes all four figures are generated by integrating along the depth axis of the unfolded volumes using a Multiple Intensity Projection.

2.2 Estimation of Stent Struts Crossings Locations

In this step a set of probable candidates is estimated for the location of stent struts crossings $C = \{(x, y, z)_1, .., (x, y, z)_n\}$. From the estimated parameters Φ, a cylindrical coordinate system is defined, that allows for an unfolded volumetric representation of the stent. The original volume I is reinterpreted and interpolated along radial, circumferential and longitudinal coordinates (r, ϕ, α_z), to construct the unfolded volume I_u capturing the maximum diameter and height of the device (Fig 2(b) and 3 Top Left). The parameterization in the cylindrical coordinates not only facilitates the assessment and annotation of the device but also significantly benefits the subsequent discriminative learning steps by eliminating feature aligning procedures and minimizing the interclass variation [7]. Next, a robust detector is trained using Haar features and the PBT algorithm to model the posterior probability of strut crossing locations $p(S|I_u)$. As radiation attenuation is much stronger for metallic materials, and hence its Hounsfield units (grey level intensity) is significally above the tissue intensities, we reduce the search space for training and testing within a binary mask, obtained by image thresholding ($\geq$ 1600 HU showed best performance in the presence of noise and artifacts), to concentrate the generation of positive and negative locations (Fig. 3 Top Right). A typical probability map for strut crossing locations is given in Fig. 3 Bottom Left.

From the obtained uniform distribution of the final candidates for stent struts crossing locations a subset is extracted by exploiting prior knowledge about the

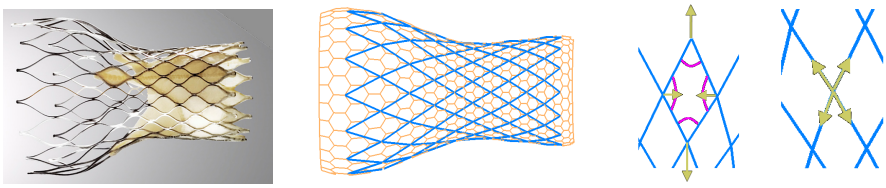

(a) (b) (c) (d)

Fig. 4. (a) CoreValve implant (Source: http://www.medtronic.com), (b) long axis cross section of stent mesh (orange) with superimposed computational mesh (blue). Forces acting on the model on deployment to converge to the observed geometric properties: (c) f_{angle} enforces the charateristic angles at the strut joints (green), (d) f_{length} maintains the strut lengths.

device geometry and topology. A clustering scheme is applied that is parameterized by the crossing location and size of a strut of an optimally deployed stent in cylindrical coordinate space (Fig 3 Bottom Left). In the spirit of non-maximal suppression for each of the clusters ($N \leq 165$), the top 10 most probable candidates are selected for further consideration.

2.3 Model based fitting

In order to address image noise and artifacts following a model based approach, a virtual templates of the target stent is created, which incorporate realistic geometrical properties of the device and mimics its mechanical behavior during the process of fitting the template to the subject specific deformation.

Device Modeling The implant consists of two eyelets and 135 cells formed by the struts, which ensues 165 strut crossing locations and 11 parallel ring levels, where the levels are defined by the short axis cuts containing the strut crossings (see Fig. 4(a)). Dimensions were obtained from the design specification and stereolithographic scans of fully expanded implants, namely the strut lengths, the characteristic angles in each cell and circumferences at each ring level. The virtual device is composed of the *computational mesh* – a 2-simplex mesh, which guides the fitting process – and the *stent mesh*, which is defined on a subset of points across the computational mesh (see Fig. 4(b)) and captures the device's geometry [8] and is associated with the measured dimensions.

Device Deployment The virtual deployment of the device is modeled by balancing external and internal forces to mimic its mechanical behavior, using iterative optimization methods. Internal stiffness and external attraction to the previously estimated strut crossings are acting on the stent template to enforce subject specific deformation, while preserving characteristic dimensions

	mean (std)	80%	90%
stent point-to-mesh	1.27 (1.26)	0.77	1.36
ascending aorta [A]	1.11 (1.4)	1.12	1.5
valsava sinuses [B]	1.09 (1.51)	1.06	1.31
annulus [C]	1.38 (1.21)	1.35	1.75

Fig. 5. Estimation accuracy in mm across the whole stent (point-to-mesh) and three levels relative to the aortic valve anatomy ([A], [B], [C]). Values of mean and standard deviation are provided as well as 80 and 90-percentiles.

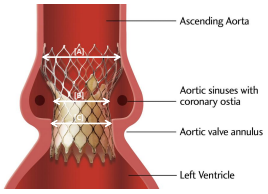

Fig. 6. CoreValve implant with sketch of target anatomy and the three evaluated ring levels (**white color**). Modified from http://www.medtronic.com

such as strut lengths. Initially centered and oriented using the previously estimated bounding box the fully expanded model represented by a simplex mesh is deformed iteratively according to the following explicit scheme:

$$\boldsymbol{p_i^{n+1}} = \boldsymbol{p_i^n} + (1-\gamma)(\boldsymbol{p_i^n} + \boldsymbol{p_i^{n-1}}) + f_{int}(\boldsymbol{p_i^n}) + f_{ext}(\boldsymbol{p_i^n}) + f_{reg}(\boldsymbol{p_i^n}) \quad (2)$$

In this equation, $\boldsymbol{p_i}$ is a point on the simplex mesh, n is the iteration number, f_{ext}, f_{int} and f_{reg} are the external, internal and regularizing forces, and γ is the weighting parameter. Fig. 4cd) show a visual description of each of the forces. In this study we employed the internal and regularizing forces. In particular, the regularizing forces f_{reg} act on the simplex mesh to provide smoothness while the internal forces $f_{int}(\boldsymbol{p_i^n}) = f_{length}(\boldsymbol{p_i^n}) + f_{angle}(\boldsymbol{p_i^n})$ model the intrinsic properties of the stent and enforce the targeted dimensions, that is the strut lengths and characteristic angles observed in the expanded shape.

By integrating the knowledge obtained from the previous estimation step. We model the external forces $f_{ext}(\boldsymbol{p_i})$ such that they drive the stent template towards the detected strut crossing points: $f_{ext}(\boldsymbol{p_i}) = \boldsymbol{c}_j - \boldsymbol{p_i}$, where $\boldsymbol{c}_j$ is a detected strut crossing and $\boldsymbol{p}_i$ is its corresponding crossing on the template. The correspondence is determined automatically, and updated at every iteration, within local bins determined in the cylindrical parameterization of the stent according to the following rule: $(\boldsymbol{c}_j, \boldsymbol{p}_i)$ is paired, if $(\boldsymbol{c}_j - \boldsymbol{p}_i) \cdot \boldsymbol{t}_i^u < d_i^u \wedge (\boldsymbol{c}_j - \boldsymbol{p}_i) \cdot \boldsymbol{t}_i^v < d_i^v$, where $\boldsymbol{t}_i^u$, $\boldsymbol{t}_i^v$ are tangents along circumferential and longitudinal directions of the stent mesh at $\boldsymbol{p}_i$ and d_i^u, d_i^v are the distances to the neighbors of $\boldsymbol{p}_i$. The algorithm iterates until convergence is detected by $\sum_i ||\boldsymbol{p_i^{n+1}} - \boldsymbol{p_i^n}||/N_i < \epsilon$, where $\epsilon = 0.02$ showed best results in our experiments.

3 Experimental Results & Discussion

The validation of the proposed framework was done on 28 patients with post operative single-phase cardiac CT data. Scans are acquired from different patients with various cardiovascular diseases (including ascending aortic root aneurysm, regurgitation, calcific stenosis and bicuspid aortic valves), using different protocols, resulting in volumes with 80 to 350 slices and 153x153 up to 512x512

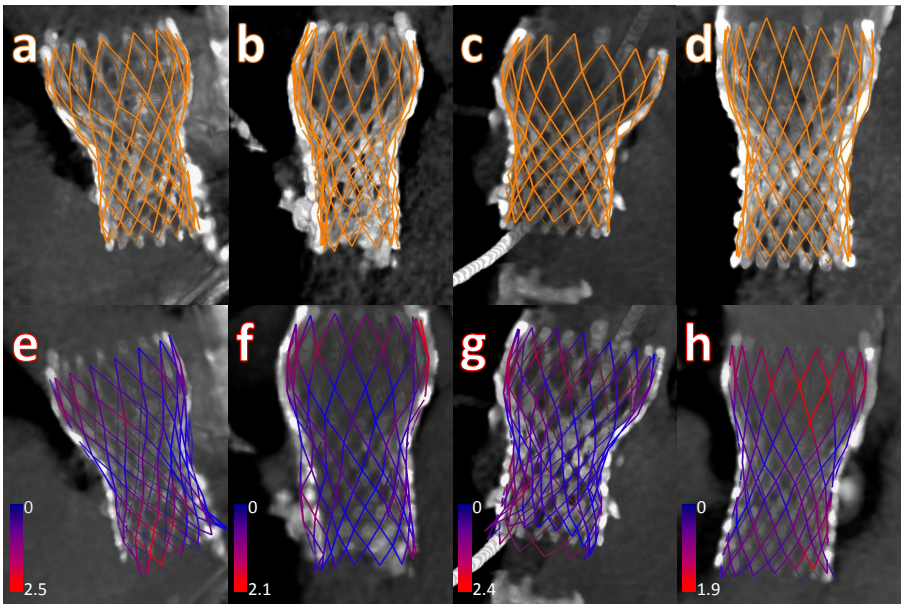

Fig. 7. Example results of ground truth stents (a-d) vs. detected stents (e-h) showing color coded point-to-mesh distance measured in mm

voxel grid resolution and an average spatial resolution of 1 mm. Each data set is associated with an expert annotation used as ground-truth.

The accuracy of the method was obtained using leave-one-out cross validation. The algorithm performed at an average speed of 10.2 seconds on a standard desktop machine (Intel Xeon 2.66Ghz, 2GB RAM). Quantitive evaluation of estimation results is provided in Table. 3. The accuracy of the method was analyzed with two metrics computed on estimation result and ground truth annotation: the point-to-mesh distance across the whole stent mesh and the point-to-curve distance among points on three levels of the stent mesh, namely on the level of the ostia, annulus and in the ascending aorta. These levels have been selected as they are most relevant for detecting critical conditions such as blockages of coronary ostia, paravalvular leakages at the annular level or vessel dissection within the ascending aorta (Fig. 6). To guarantee a symmetric measurement, those distances were calculated in both directions, i.e. from estimated result to ground truth annotation and vice versa. The accuracy is close to the mean image resolution of 1 mm and acceptable regarding the fact that CT imaging displays the struts with a diameter of about 2 mm. A selection of estimation results vs. ground truth annotations are displayed in Fig 7, where estimation results are overlayed with color coding of point-to-mesh error.

Fig. 8 highlights the robustness of our method in three cases with heavy calcification and artifacts and displays two-dimensional reformation of the image

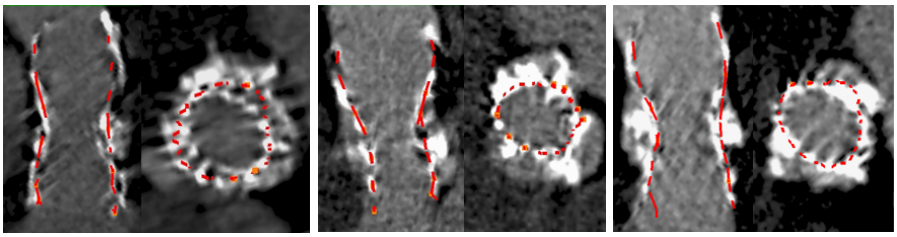

(a) (b) (c)

Fig. 8. Estimation results in cases with strong calcifications and image artifacts. The algorithm produces plausible results despite considerable image distortion.

data overlayed with estimation results. Our algorithm still produces plausible results despite the presence of considerable image artifacts, which would harm the performance of purely data-driven approaches.

4 Conclusion

In this paper a framework for postoperative assessment of aortic valve implantation was presented based on a fast and robust estimation of a detailed stent model. Our approach enables precise modeling of the patient-specific stent morphology from clinical images. The validation on 28 patients showed promising within the range of image resolution. Our framework, being automatic, may thus constitute a surrogate tool for quantitative and systematic assessment of deployed stents, potential device migration and defects during long term follow up examinations.

References

1. Leon, M.B., et. al.: Transcatheter aortic-valve implantation for aortic stenosis in patients who cannot undergo surgery. New England Journal of Medicine **363**(17) (2010) 1597–1607
2. Langs, G., et. al.: Learning deformation and structure simultaneously: In situ endograft. (2010)
3. Klein, A., et. al.: Automatic segmentation of the wire frame of stent grafts from ct data. (2011)
4. Ewe, S.H., et. al.: Role of computed tomography imaging for transcatheter valvular repair/insertion. In: Springerlink.com. (2011)
5. Tu, Z., et. al.: Probabilistic boosting-tree: Learning discriminative methods for classification, recognition, and clustering. In: ICCV. (2005) 1589–1596
6. Zheng, Y., et. al.: Fast automatic heart chamber segmentation from 3d ct data using marginal space learning and steerable features. In: ICCV. (2007)
7. Tu, Z., et. al.: Probabilistic 3D polyp detection in CT images: The role of sample alignment. In: IEEE CVPR. (2006) II: 1544–1551
8. Larrabide, I., et. al.: Fast virtual stenting with deformable meshes: Application to intracranial aneurysms. In: MICCAI (2). (2008) 790–797

Landmark-based registration of OCT image sequences for the follow-up of stent coverage and apposition

Laurent Sarry[1], Romain Dumas[1], Florian Dubuisson[1], Emilie Péry[1], Nicolas Combaret[2], Pascal Motreff[1,2]

[1]Clermont Université, Université d'Auvergne, ISIT, BP 10448, F-63000 Clermont-Ferrand.
CNRS, UMR6284, BP 10448, F-63000 Clermont-Ferrand.
[2]CHU Gabriel Montpied, Département de Cardiologie, BP 69, F-63003 Clermont-Ferrand.

{laurent.sarry@u-clermont1.fr}

Abstract. We propose a new landmark-based registration method designed to take into account the specific geometry of OCT endovascular acquisition. B-spline approximation is used to recover probe trajectory and angular offsets between two image sequences from a few landmarks pinpointed out by the cardiologist. The well-posedness of the control point estimation is assured by a bending regularization energy automatically weighted by leave-one-out cross-validation. The accuracy of the algorithm is validated on phantom datasets and its clinical interest illustrated on patient datasets by comparing coverage and apposition score maps for registered image volumes.

Keywords: optical coherence tomography, landmark registration, coronary artery stenting

1 Introduction

Optical Coherence Tomography (OCT) is an intravascular imaging technique that provides *in vivo* high-resolution transversal views of coronary artery segments allowing to control the outcome of interventional therapies. It can accurately differentiate the most superficial layers of the arterial wall as well as the stent wire and the vascular tissue surrounding them [1].

OCT appears to be the most efficient technique to confirm correct apposition of a stent mesh immediately after the procedure [2]. OCT can also evaluate the remote implantation of stent neointimal coverage, and corresponding good arterial healing. Finally, during fading of rare thrombotic complications, the high-resolution endoluminal images allow to define the remaining part of obstructive thrombus and its evolution under drug treatment, or after mechanical thrombectomy. In each of those situations, it is important to compare automatic pullbacks obtained at different times on the same arterial segment. Comparative measurements of surfaces and volumes (either of the vessel lumen area, or the media overlying the stent, being a case of neointima or thrombus depending on the context) require accurate registration in longitudinal and axial views. To our knowledge, there is no existing literature on direct

adfa, p. 1, 2011.

OCT to OCT registration, some works have dealt with its registration to IVUS [3] or with IVUS to IVUS registration [4]. These are 2D iconic registration frameworks based on cross-correlation similarity measure that applies to key frames matched by the user.

The proposed method is also based on anatomical landmarks such as the birth of collateral branches on selected frames, but our contribution is to compute a non-rigid robust transformation between the two OCT pullbacks from the landmarks with a B-spline geometric model comparable to the one used in angio-IVUS or OCT registration frameworks (see for instance [5]). It accounts for the variations in probe trajectory and pullback angular speed. Accuracy of the registration algorithm is assessed using several phantom acquisitions. Score maps of malapposition and neointimal coverage are also compared for registered pullbacks of two patients [10,11].

2 Material and methods

2.1 OCT acquisition protocol

The OCT probe is made of a Michelson interferometer integrated at the tip of a fiber optic segment. The lumen ray is split in two halves. The first half is reflected by the reference mirror and the other half by the coronary artery itself. The state-of-the-art technology (ImageWire C7, LightLab Imaging, Westford, MA) is frequency-domain OCT (FD-OCT) uses the Fourier transform to provide a back reflection profile as a function of depth [6]. The main advantage of OCT over other invasive techniques as IVUS (IntraVascular UltraSound) are improved axial and lateral resolutions up to 12µm and 19µm respectively at a maximum rate of 100 frames per second. Penetration depth and pullback speed are the main limitations of this technology, but they have significantly improved with the FD-OCT generation up to 10mm and 20mm/s respectively. Therefore, a pullback of length L=53.8 mm only takes 2.69s; short enough so that the physiological saline flush, used to make the lumen transparent to red light, can be performed without stopping blood circulation using an occlusive balloon. The OCT final frame stack is made of nsl=268 transversal slices, but, the actual acquisition has a helical geometry (at 100 max RPS and a typical pitch of 0.2mm) that corresponds to the rotation of the probe along the pullback trajectory [6]. As shown by Fig. 1, each frame is computed from the polar to Cartesian transformation of lpf=504 lines per frame (for the C7 system) of one helical helix revolution.

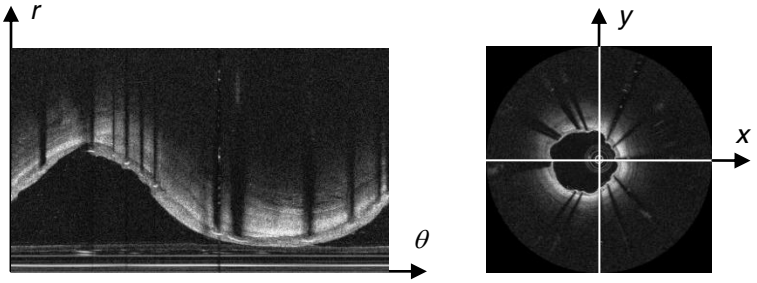

Fig. 1. OCT raw image slice and the corresponding slice after transformation from polar coordinates (r,θ) to Cartesian coordinates (x,y).

2.2 Geometrical transformation between image volumes

As it can be observed in phantom acquisitions (Fig. 2), the differences between the source image volume $S(x,y,z)$ (Fig. 2a) and the target image volume $T(x,y,z)$ (Fig. 2b) are threefold:

- Acquisition pullbacks never start at the same point leading to offsets between slices in longitudinal direction z;
- The position of the acquisition probe with respect to lumen and stent features is not perfectly reproducible due to temporal changes in vessel geometry during cardiac cycle and between acquisitions;
- The angular origins of OCT acquisitions are not in correspondence because they depend on when the acquisitions start. Moreover, angular offsets are likely to occur between two acquisition pullbacks due either to vessel slight torsion during heart contraction, or to temporal changes in friction between the rotating probe and its guide that influences angular speed.

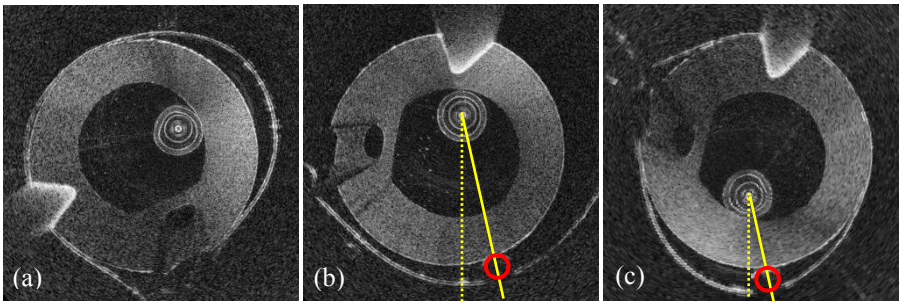

Fig. 2. A given slice of the source (a and c) and target (b) OCT image for the phantom in case of torsion constraint. The source slice before registration (a) shows several discrepancies with regard to the target slice: longitudinal offset of several slices, off-center displacement and variable angular offset. The position of the spherical metallic markers is highlighted by a red circle and yellow lines mark that the angles between markers and vertical direction with respect to the probe are preserved.

The transformation described by the first two points is a translation the vector of which can be interpolated by a 3D nonperiodic B-spline curve of parameter $t \in [0,1]$ and degree p:

$$\Delta\mathbf{P}(t) = \sum_{i=0}^{n} \Delta\mathbf{P_i} N_{i,p}(t), \tag{1}$$

where $\Delta\mathbf{P_i}$ are the $n+1$ control points defined over the non-decreasing sequence of $n+p+2$ knots, $0=t_0=\ldots=t_p<\ldots<t_{n+1}=\ldots=t_{n+p+1}=1$ and $N_{i,p}$ the $n+1$ basis functions of degree p.

The angular offset $\Delta\theta$ of the deformation is also described by a B-spline of parameter t and degree p, sharing the same knot sequence as the curve $\Delta\mathbf{P}(t)$:

$$\Delta\theta(t) = \sum_{i=0}^{n} \Delta\theta_i N_{i,p}(t), \tag{2}$$

where $\Delta\theta_i$ are the n+1 control values defined over the knots.

2.3 Landmark-based Euclidean constraint

The unknowns of the deformation model are the control points $\Delta\mathbf{P_i}$ and the angular control values $\Delta\theta_i$, namely 4 scalars times n+1. One practical way to estimate them is to ask the cardiologist for a few point correspondences between the source and target image volumes.

Usually, for a five-cm long segment, it is feasible to find few invariant features such as bifurcations with small collateral branches. The stent itself and the metallic echoes of its wire, called struts, cannot be used as landmarks because of the impossibility of visually pairing them as they all look like light echoes. With the exception of very specific cases, e.g. the presence of plaque or thrombus with distinctive geometry, there will never be more than 10 landmarks, being the usual case less than 5. Therefore the model must adapt itself to the given number of landmarks: the more landmarks the user provides, the more accurate the description will be. Towards this end n was chosen equal to 10, giving enough degree of freedom to the representation. In the case where there are less landmark constraints than unknowns, additional regularization constraints are mandatory.

In practice, the m landmark points are picked out in the source and target Cartesian coordinate systems, then converted into helical coordinates $\mathbf{S}(t_s,r_s)$ and $\mathbf{T}(t_t,r_t)$, where t is the normalized B-spline parameter (nearly proportional to the curvilinear abscissa given the fact that the curve is almost rectilinear) and r is the distance to the axis curve (Fig. 3).

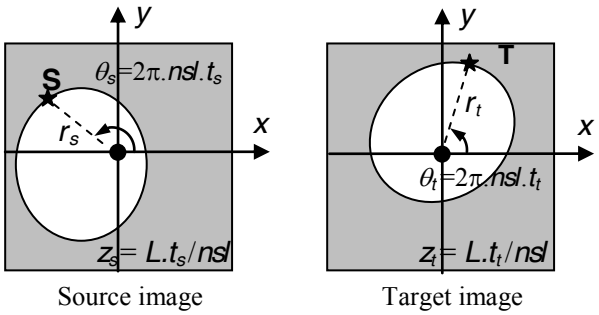

Fig. 3. Schematic view of two paired points **S** and **T** picked out from two slices at respective longitudinal positions z_s and z_t.

The deformation defined by the curve and the angular B-spline model allow transforming target image coordinates to source image coordinates. They can be constrained by the translation vectors $\Delta\mathbf{P}$, and angular offsets $\Delta\theta$, computed at m different target parameter values t_j from the landmark pairs given by the user:

$$\Delta\mathbf{P}(t_j) = \begin{pmatrix} (r_t - r_s)\cos\theta_s \\ (r_t - r_s)\sin\theta_s \\ z_t - z_s \end{pmatrix} \text{ and } \Delta\theta(t_j) = \theta_s - \theta_t \tag{3}$$

Minimizing the distance between the pairs of landmarks turns into finding the control points $\mathbf{\Delta P_i}$ and angular values $\Delta\theta_i$ respectively written in matrix and vector form $\mathbf{\Pi}$ and $\mathbf{\Theta}$ that minimize the data energy terms:

$$\varepsilon_{d\mathrm{P}}(\mathbf{\Pi}) = \|\mathbf{N\Pi} - \mathbf{D}_\mathrm{P}\|^2 \text{ and } \varepsilon_{d\theta}(\mathbf{\Theta}) = \|\mathbf{N\Theta} - \mathbf{D}_\theta\|^2, \tag{4}$$

$$\text{with } \mathbf{N} = \begin{bmatrix} N_{0,p}(t_0) & \cdots & N_{n,p}(t_0) \\ \vdots & N_{i,p}(t_j) & \vdots \\ N_{0,p}(t_m) & \cdots & N_{n,p}(t_m) \end{bmatrix}, \tag{5}$$

$$\mathbf{D}_\mathrm{P}^\mathrm{T} = \begin{bmatrix} \mathbf{\Delta P}(t_0) & \cdots \mathbf{\Delta P}(t_j) \cdots & \mathbf{\Delta P}(t_m) \end{bmatrix} \text{ and } \mathbf{D}_\theta^\mathrm{T} = \begin{bmatrix} \Delta\theta(t_0) & \cdots \Delta\theta(t_j) \cdots & \Delta\theta(t_m) \end{bmatrix}. \tag{6}$$

2.4 Bending energy for regularization

To make the minimization problems of $\varepsilon_{d\mathrm{P}}$ and $\varepsilon_{d\theta}$ well-posed, bending energy terms $\varepsilon_{b\mathrm{P}}$ and $\varepsilon_{b\theta}$ are added to them, and weighted by regularization factors λ_P and λ_θ. They are defined by the integral of the second derivative over the natural domain of the B-splines:

$$\varepsilon_{b\mathrm{P}}(\mathbf{\Pi}) = \int_0^1 \left(\frac{\partial^2 \mathbf{\Delta P}(t)}{\partial t^2}\right)^2 dt \text{ and } \varepsilon_{b\theta}(\mathbf{\Theta}) = \int_0^1 \left(\frac{\partial^2 \Delta\theta(t)}{\partial t^2}\right)^2 dt. \tag{7}$$

In the cubic case (p=3), they can be expressed in matrix form [7]:

$$\varepsilon_{b\mathrm{P}}(\mathbf{\Pi}) = \left|\mathbf{\Pi}^\mathbf{T}\mathbf{B}\mathbf{\Pi}\right|_1 \text{ and } \varepsilon_{b\theta}(\mathbf{\Theta}) = \mathbf{\Theta}^\mathbf{T}\mathbf{B}\mathbf{\Theta}, \tag{8}$$

where $\mathbf{B}$ is a (n+1)×(n+1) matrix, called the bending matrix, built from summing over the diagonal n–3 times the matrix $\mathbf{b}$ of dimensions 4×4 corresponding to the elementary bending over the intervals between successive internal B-spline knots:

$$\mathbf{b} = \begin{bmatrix} 2 & -3 & 0 & 1 \\ -3 & 6 & -3 & 0 \\ 0 & -3 & 6 & -3 \\ 1 & 0 & -3 & 2 \end{bmatrix}. \tag{9}$$

The solution of the regularized problem is given by:

$$\mathbf{\Pi} = \mathbf{H}(\lambda_\mathrm{P})\mathbf{D}_\mathrm{P} = (\mathbf{N}^\mathrm{T}\mathbf{N} + \lambda_\mathrm{P}\mathbf{B}^\mathrm{T}\mathbf{B})^{-1}\mathbf{N}^\mathrm{T}\mathbf{D}_\mathrm{P}, \tag{10}$$

$$\mathbf{\Theta} = \mathbf{H}(\lambda_\theta)\mathbf{D}_\theta = (\mathbf{N}^\mathrm{T}\mathbf{N} + \lambda_\theta\mathbf{B}^\mathrm{T}\mathbf{B})^{-1}\mathbf{N}^\mathrm{T}\mathbf{D}_\theta. \tag{11}$$

The hyperparameters λ_P and λ_θ are estimated using the leave-one-out cross-validation criterion defined in [8] that has been proved to have a closed-form solution in case of linear least-square problem:

$$\mathrm{LOOCV}(\lambda_P) = \frac{1}{n}\left\|\mathrm{diag}\left(\frac{1}{\mathbf{1}-\mathrm{diag}(\mathbf{H}(\lambda_P))}\right)(\mathbf{N\Pi}-\mathbf{D}_P)\right\|^2, \quad (12)$$

$$\mathrm{LOOCV}(\lambda_\theta) = \frac{1}{n}\left\|\mathrm{diag}\left(\frac{1}{\mathbf{1}-\mathrm{diag}(\mathbf{H}(\lambda_\theta))}\right)(\mathbf{N\Theta}-\mathbf{D}_\theta)\right\|^2. \quad (13)$$

As a first approximation, these functions are minimized using the Powell's conjugate gradient descent algorithm [9]. Global search appears also as a sensible approach since local minima could arise as the function is not perfectly convex.

2.5 Helical ray casting for source image deformation

Simulated rays were sampled along the estimated 3D curve. They served as support for the target image voxels, and are stuck into the source image volume. As target voxels usually do not fall onto the grid of source voxels, a trilinear interpolation scheme was used to compute approximate gray levels. For the C7 OCT system, the number of rays is $n_r = nsl \times lpf = 135{,}072$. Ray number k corresponds to the parameter $t_s = k/n_r$ and to the normal pullback rotation angle value of $\theta_s = 2\pi.nsl.t_s$ with an offset equal to $\Delta\theta(t_s)$.

2.6 Validation

To validate the registration algorithm, two kinds of OCT data were used:

- A simple phantom was build using a urinary probe injected with water in order to adjust optical indices at the lumen wall. Six experiments were carried out: from 5 to 16 small metallic balls of diameter 0.6 mm evenly and non evenly spread were stuck outside the probe using adhesive tape. Different amounts of bending and/or torsion of the probe were manually induced between the two OCT acquisitions in order to mimic the constraints imposed by coronary artery deformation during the cardiac cycle. One half of the markers were used as landmarks for registration and the other half as test points to assess the accuracy of the process.
- Two datasets of patient OCT sequences, the first before and after stent apposition correction during the same implantation procedure, and the second before and after stent neointimal coverage at 3 months delay. A comparison between apposition and coverage score maps with respect to the same referential after registration was made. The way cylindrical maps are obtained is fully detailed in [10,11].

3 Experimental results and discussion

Figure 2 shows good visual correspondence between the target slice (b) and the source slice after deformation (c).

The landmarks are perfectly superimposed as confirmed by the distance between test markers that decreases from (8.29±2.53) mm before registration to (0.34±0.30) mm after registration (1.5 order of magnitude of the interslice resolution). The error is

inversely proportional to the number of constraint points used, ranging from 0.81 mm (3 points) to 0.11 mm (10 points). As expected, the spacing between points influences results, by increasing the error when points are non evenly spread (up to 0.9mm in our case for 3 points with the second not in the middle). Certainly with one landmark in a given slice, only the angle between the marker itself and the probe can be recovered exactly, and small errors in object orientation may occur if the probe moves with respect to the vessel. The phantom case of Fig. 2 is one of the most pejorative cases as the probe has moved in the opposite diametrical direction due to the imposed torsion deformation. Nevertheless, the result is accurate enough and visually consistent in the opinion of the cardiologist.

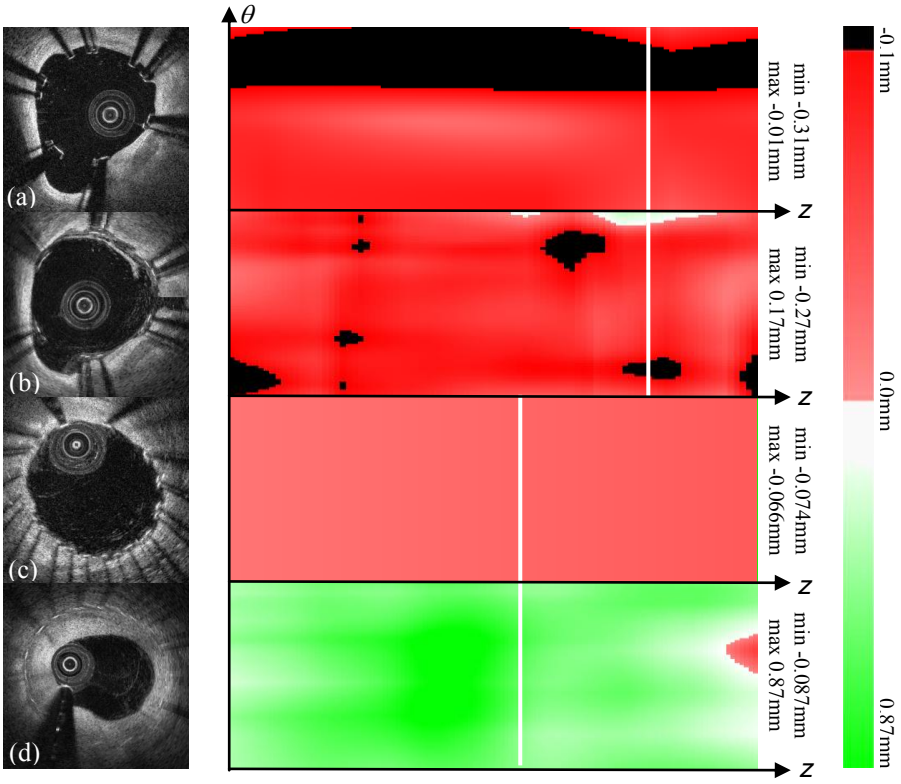

Fig. 4. Comparison of registered slices and score maps in cylindrical coordinates ($z\theta$) of the distance between stent and lumen wall (ill-placed stent in black, perfectly apposed but naked stent in red and covered stent with increasing thickness in green levels): before (a) and after (b) malapposition correction and before (c) and after (d) stent coverage. The white vertical lines indicate the location of the selected slices. Minimum and maximal distances between stent and lumen walls are given for the four color maps (negative if the strut echo lies inside the lumen).

Another major benefit of this kind of transformation is that it perfectly matches score maps built in cylindrical coordinates. As shown in figure 4, it is possible to compute distance maps between stent and lumen wall, and to compare them point by point, thanks to the performed registration. Distance greater than the mesh thickness, defines an ill-placed stent in black. Figures 4(a) and (b) show that post-dilatation has

significantly enhanced stent apposition and that only a few residual black spots remain. Figures 4(c) and (d) show the evolution between a very homogeneous apposition distance map to a very important and heterogeneous restenosis map in only 3 months. For patient data, distance errors computed at the landmarks were (11.1±2.1) mm before registration and (0.15±0.12) mm after registration.

Registration of a 976×504×268 raw target OCT volume with a 976×976×268 cartesian source OCT volume takes about one minute. The present software was implemented in C++ using ITK (Kitware Inc., New York, USA). The major computational cost stands in the ray casting process that is for now implemented in a multithreaded way but on CPU. Speed would be greatly increased if 3D texture capabilities on GPU were used.

4 Conclusion and perspectives

An accurate landmark-based method to superimpose OCT image sequences was described; it is based on a few landmarks pointed out by the cardiologist. Comparative analysis based on this registration algorithm will allow for extensive studies targetting tissue repair process in the vicinity of the stent, and also evaluate the impact of corrective treatments such as thrombo-aspiration after thrombotic occlusion or post-dilatation in case of suboptimal initial deployment.

References

1. T.L. Pinto and R. Waksman. Clinical applications of optical coherence tomography. *Journal of Interventional Cardiology*, 19:566-573, 2006.
2. F. Prati, E. Regar, G.S. Mintz et al. Expert review document on methodology, terminology, and clinical applications of optical coherence tomography: physical principles, methodology of image acquisition, and clinical application for assessment of coronary arteries and atherosclerosis, *European Heart Journal*, 31(4):401-415, 2010.
3. G. Unal, S. Lankton, S. Carlier, G. Slabaugh and Y. Chen. Fusion of IVUS and OCT through semi-automatic registration, in *Proc. International Workshop on Computer Vision for Intravascular Imaging* (CVII), pp. 163-170, 2006
4. J. Amores and P. Radeva. Non-rigid registration of vessel structures in IVUS images, IbPRIA 2003, LNCS 2652, pp. 45–52, 2003.
5. B. Godbout, J.A. de Guise, G. Soulez and G. Cloutier. 3D registration of vessel structures from IVUS data on biplane angiography, *Academic Radiology*, 12(1):10-16, 2005.
6. M. E. Brezinski. Optical Coherence Tomography: principles and applications. Burlington, MA: Elsevier, 2006.
7. F. Brunet. Contributions to parametric image reconstruction and 3D surface reconstruction, PhD thesis, 2011.
8. A. Bartoli. Maximizing the predictivity of smooth deformable image warps through cross-validation. *Journal of Mathematical Imaging and Vision*, 31(2-3):133–145, 2008.
9. M.J.D. Powell. An efficient method for finding the minimum of a function of several variables without calculating derivatives. *Computer Journal*, 7:155–162, 1964.
10. F. Dubuisson, C. Kauffmann, P. Motreff, L. Sarry. In vivo OCT coronary imaging augmented with stent reendothelialization score, MICCAI 2009, Part I, LNCS 5761:475–482, 2009.
11. C. Kauffmann, P. Motreff, L. Sarry. In vivo supervised analysis of stent reendothelialization from Optical Coherent Tomography. *IEEE Trans. Medical Imaging*, 29:807–819, 2010.

Semi-automatic Measurement of Vessel Wall Support from Implanted Stents in IVOCT Image Sequences

Ancong Wang, Jeroen Eggermont, Niels Dekker, Johan H.C. Reiber, Jouke Dijkstra

Image Processing Division, Leiden University Medical Center, Leiden, Netherlands

Abstract. Intravascular stents are devices that are used for supporting vessel walls to improve the blood flow. Intravascular optical coherence tomography (IVOCT) provides very high resolution images which can be used to evaluate the support of implanted stents to vessel walls during the percutaneous coronary intervention (PCI) and at follow up. The stent cell structure is important for stent support analysis and its full size and maximum circular unsupported surface area (MCUSA) are commonly used to measure the degree of vessel wall support. We present two different methods (*A* and *B*) to compute full stent cell area and one method to compute the MCUSA. These methods include stent strut detection and transformation, stent cell detection, stent surface reconstruction, cylinder fitting to stent cells and MCUSA detection. To measure full stent cell size, method *A* uses the reconstructed stent surface, while method *B* uses the cell contours after cylinder fitting. The MCUSA method determines the largest circle in this contour using distance transform. The evaluation on two phantom datasets shows accurate measurements of the stent cells. Based on our phantom data set, the accuracy of methods *A* and *B* are 99.3% and 99.1% respectively and the results from both methods are consistent. The methods were also applied to real IVOCT image sequences for support analysis.

1 Introduction

Coronary stents are widely used to treat coronary artery diseases. During a PCI, a stent is extended by an inflated balloon to support the vessel wall and to keep the vessel open. Clinical research has demonstrated that the support of implanted stents to the vessel wall positively influences the outcome of the PCI [1]. Stents should be flexible and be able to provide enough support. The full size of each cell structure of the implanted stent is one of most common feature used to compute the stent support. Recently, the maximum circular unsupported surface area (MCUSA) was proposed as a new feature to evaluate the stent support [2] and it is defined as the maximal circle area that can be fit inside a stent cell structure.

Stent cell measurements can be used to evaluate the stent design for its distribution after implantation, or to compute the coverage of an implanted stent to side-branches. It also provides the possibility to evaluate the mechanism of controlled drug release from drug-eluting stents as well.

IVOCT is a relatively new 3D optical imaging technique which provides very high resolution (10 – 20 μm) images of the coronary vessels [3]. It is increasingly being

used for the evaluation of stent placement. Because IVOCT images are the tomographic cross-sections of vessels, implanted stents are visible as individual bright spots (struts). IVOCT data can be used for the support analysis of implanted stents by providing precise location of the individual struts. To the best of our knowledge, there is no published method to compute the full cell size or MCUSA of implanted stents in IVOCT image sequences.

The challenging part of the support measurements is to identify the stent cells and to calculate their area in the 3D space. In order to reduce the complexity when identifying the stent cell, we convert the stent strut position from 3D to 2D and keep the conversion mapping, so that the final calculation can be based on the original 3D cell contour. In this paper, we present two different methods to compute the full stent cell size and one method for MCUSA estimation. In section 2, the measurement methods are presented, while the empirical results of two phantom datasets and two real IVOCT datasets are presented in section 3. The analysis of the results is described in section 4 and the conclusions in section 5.

2 Methods

The new approach consists of five parts: (1) stent strut detection and transformation; (2) 3D stent cell contour generation; (3) full cell area measurement method *A*; (4) full cell area measurement method *B*; (5) MCUSA estimation. All the measurements can be performed as the flow chart illustrates in Fig. 1.

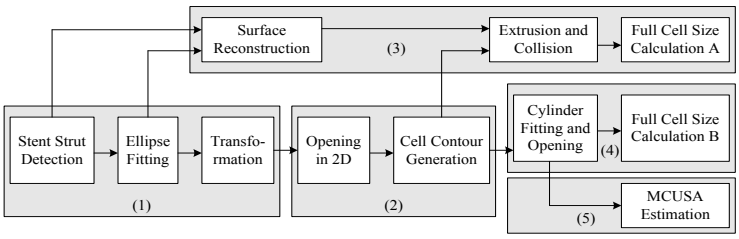

Fig. 1. The flow chart of the implanted stent cell measurement methods

2.1 Stent Strut Detection and Transformation

Bare metal and drug-eluting stent struts can be detected automatically following recently published methods [4, 5, 6]. As Fig.2 (a) shows, the stent center is not the image center, so struts in (b) are transformed and then projected onto the surface of a cylinder like (c) which can be opened in 2D for strut cell recognition.

Because a stent is extended by an inflated balloon in the vessel, its cross-sections are more or less elliptical. Therefore, the stent struts in each frame are fitted with an ellipse using a modified least-squares ellipse fitting method [7 More struts can lead to better fitting, so the struts from 3 continuous frames are used to fit the ellipse in the middle frame. Infrequently, if there are still less than 5 struts for ellipse fitting, this stent contour will be generated by interpolation. Ellipse centers are transformed to the

center of IVOCT images together with stent struts. After transformation, all the struts can be projected onto a cylinder based on their angles. Each strut in (c) matches the corresponding strut in (d), therefore, after detecting the stent cell from opened stent (e), the original 3D stent cell contour (f) can be generated.

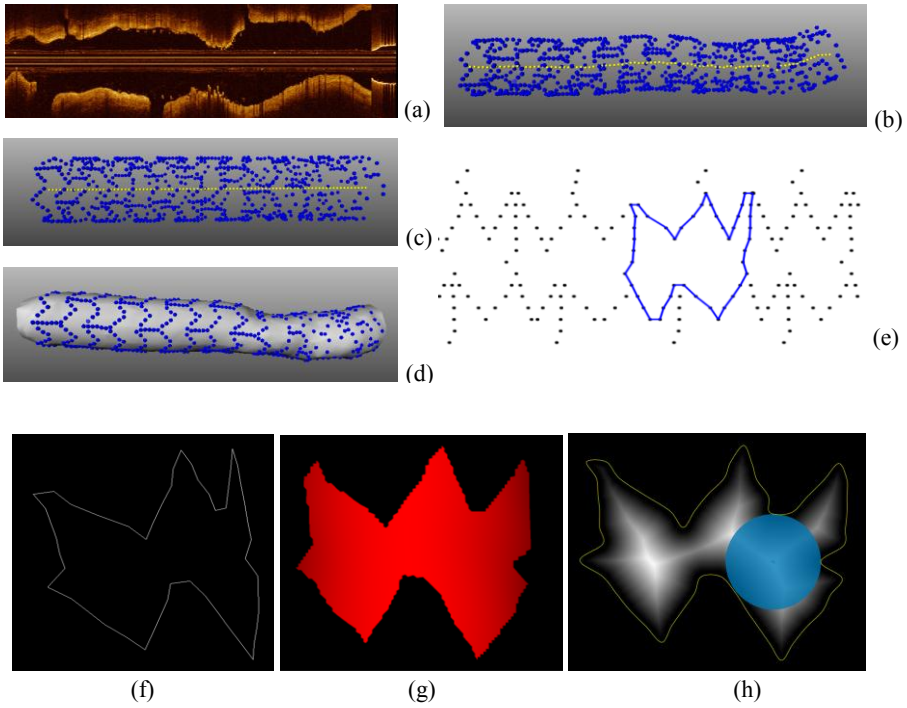

Fig. 2. In (a) a longitudinal IVOCT image is presented and (b) shows the stent struts (blue dots) and the stent contour centers (yellow dots) of a real IVOCT image sequence. Fig. 2(c) shows the transformed and projected struts on a cylinder surface. Fig.2(d) is the reconstructed surface with struts. Fig. 2(e) shows a part of an opened 2D stent with clear cell structures. A stent cell is shown in blue and (f) shows the corresponding 3D stent cell contour; with (g) the selected cell surface piece, while (h) shows the opened cell contour and the detected MCUSA by the blue circular area. The white area is the result of the distance transformation.

2.2 Stent Cell Contour Generation

There is a large variety in the shapes of cell structures of different stents and a stent cell can be distorted during the expansion. Additionally, each stent cell structure consists of many stent struts. Without any a-priori information, it is challenging to classify automatically the struts that belong to each cell. However, after having opened the stent into a 2D mesh as Fig. 2(e), the stent cell patterns can be recognized better. This mesh shows a clear structure but the real area still needs to be derived, so a mapping is required between the struts in the 2D mesh and the struts in the original 3D space.

To generate the stent cell contour, we need to identify the struts that belong to each individual cell. Our method requires the user to observe the pattern in the 2D mesh and then select the struts on the scaffold junctions in the proper order. Usually, it takes about 5 seconds to recognize a stent cell. Users can select two key struts and the struts between these two key struts are found and linked automatically based on the shortest distance. Once all the struts from the 2D mesh are recognized, through the mapping, the corresponding struts in the original 3D space are selected in the same order. Finally, the 3D stent cell contour can be generated by linking the struts using a B-spline. A cell contour is shown in Fig. 2(f).

2.3 Full Cell Size Measurement *A*

The cell contour defines the cell area of the implanted stent, so the surfaces for the stent cells are generated. With the stent struts detected as described in section 2.1, the stent surface can be reconstructed using the method proposed by Hoppe [8], which can reconstruct an accurate, piecewise smooth surface from a group of points. However, the guide wire can cause breaches on the reconstructed stent surface, since no information can be collected in its shadow area. In this case, we fill this blank gap with artificial points on the fitted stent ellipse. With the guide wires detected by strut detection method [4] and the fitted ellipse from section 2.1, imaginary points are added on the ellipse arcs behind the guide wires. It should be noted that any stent cell that contains such artificial points cannot be used for measurements. They only support the stent surface reconstruction to compute the other cells.

Next, the cell surface can be selected using 3D stent cell contours. The cell contour may not exactly be located on this stent surface, because the interpolated points on the contour can be located above or below the stent surface. To solve this problem, the cell contour can be projected on the surface and then the cell area can be cut from the surface. For projection, the cell contour is extruded to generate a hollow object to intersect with the stent surface. The contour extrusion direction and length is indicated by a calculated vector. The vector is orthogonal to the centerline of the stent and passes through the center of the boundary box of the stent cell contour. The collided part is selected from the stent surface as the cell surface using VTK [9] as Fig.2 (g) shows. It is represented by many small triangles and its area can be calculated by summing the areas of these triangles.

2.4 Full Cell Size Measurement *B*

A second method B to calculate the full size of stent cells was also implemented by fitting the stent struts with a cylinder. However, to fit the whole stent to a single cylinder can introduce big errors, because stents can be bended or distorted during the placement. In order to reduce the errors that are introduced by cylinder fitting, we only use the struts belonging to one stent cell instead of all the struts. Because the cell struts do not cover the whole surface of the cylinder, we need to use a good guess for initialization to guide the cylinder fitting in case it fails. The guessed initial cylinder has the same origination and the radius as the whole fitted cylinder. The fitting is

based on the least-squares method [10] which can minimize the sum of the absolute distance between struts to the fitted surface.

After cylinder fitting, the stent cell is opened into 2D as Fig. 2 (h) shows. Compared to the opening in section 2.1, this time the real stent cell area is reserved. Attention is paid to this procedure, because it may separate the stent cell into two halves. If the opening starts from the middle of the stent cells, we need to rotate the start position to the outside of the stent cells. Besides, the new resolution of the opened contour should be calculated. The pixel size in the angle-axis direction should be calculated from the radii of fitted cylinders, while the pixel size in the cylinder orientation direction should be calculated based on the angle of cylinder orientation. With the size of each pixel, the full size of the opened stent cell can be calculated.

2.5 MCUSA Estimation

MCUSA is the maximal circle that can be fitted inside the opened 2D stent cell from section 2.4. It is usually used together with the full cell size during the research for stent support analysis. The center of MCUSA should be the point that has the maximum shortest distance to its surrounding boundary. We first generate an image from the 2D cell contour and then apply a distance transformation algorithm. The pixel having the highest intensity should be the center of the MCUSA and the intensity value is the maximum shortest distance. There may be more than one maximum circle, but they all have the same size. Using the pixel size from section 2.4, the size of MCUSA can be calculated.

3 Evaluation

All the IVOCT image sequences that we have tested were acquired with a C7-XR frequency-domain OCT intravascular imaging system using a C7 Dragonfly imaging catheter (LightLab Imaging, Inc., Westford, MA, USA). During the imaging, blood was flushed with contrast medium. The pullback speed was 20.0 mm/s and the frame rate was 100 frames/s. Two randomly selected polar IVOCT image sequences were used in our research. One data set contains a guide wire while the other one does not. The image sequence size is 960 pixels × 504 pixels × 271 frames and they were converted into 1024 pixels × 1024 pixels × 271 frames Cartesian image sequences. After the conversion, the axial resolution is 6.85 μm and the distance between the frames is 0.2 mm.

A phantom data set was generated by scanning a 3.0 × 8.0 mm coronary stent using Micro-CT. The CT data set also contains cross-sections of stent as the IVOCT, but with higher resolution. Its size is 1024 pixels × 1024 pixels × 1240 frames with a voxel size of 5.86 μm × 5.86 μm × 6.62 μm. In this phantom data set, the extended stent is almost a cylinder of which the average diameter is 3.0 mm and has a length of 8.2 mm. By fitting the saw-shape part in one side of the stent to the saw-shape part in the other side, we can treat this stent as a cylinder. The saw-shape part is about 0.8 mm, so the new cylinder length is 7.4 mm. The stent surface area is about 69.7mm^2.

Due to its high resolution, stent cell results from method *B* were used as the ground truth. To estimate whether methods *A* and *B* work accurately on data sets with the same slice distance as IVOCT, we re-sampled the phantom data set with the slice distance of 0.2 mm (one frame out of every thirty frames).

Table 1. Maximum value, minimum value, mean value with standard deviation and the sum of the stent cell size from method *A*, *B* and MCUSA measurement. Original dataset is the phantom dataset with all slices. Resampled dataset is the phantom dataset with fewer frames, so that it has the same slice distance as real IVOCT data sets.

Data set	Method	Max (mm^2)	Min (mm^2)	Mean ± SD (mm^2)	Sum (mm^2)
Original dataset	*A*	5.50	3.85	4.59 ± 0.41	68.82
	B	5.74	3.96	4.75 ± 0.44	71.27
	MCUSA	1.70	0.95	1.29 ± 0.22	19.28
Re-sampled dataset	*A*	5.64	3.97	4.72 ± 0.44	70.77
	B	5.74	3.99	4.79 ± 0.45	71.90
	MCUSA	1.70	0.87	1.25 ± 0.22	18.76

Table 2. Maximum value, minimum value, mean value with standard deviation and the sum of the stent cell size from method *A*, *B* and MCUSA measurement. IVOCT1 contains a bioabsorbable stent without guide wire, IVOCT2 contains a metal stent and a guide wire.

Data set	Method	Max (mm^2)	Min (mm^2)	Mean ± SD (mm^2)	Sum (mm^2)
IVOCT1	*A*	3.78	1.00	2.54 ± 0.78	137.11
	B	3.96	1.07	2.66 ± 0.79	143.40
	MCUSA	1.40	0.25	0.76 ± 0.30	40.87
IVOCT2	*A*	2.92	1.39	2.20 ± 0.43	22.01
	B	3.00	1.45	2.30 ± 0.45	22.97
	MCUSA	1.21	0.52	0.86 ± 0.25	8.55

Stent struts from both original and re-sampled phantom data sets were detected automatically. First, our methods were applied to the original phantom dataset to compute the ground truth. Next, the methods were tested on the re-sampled phantom dataset that has the same slice distance as IVOCT to determine the possible changes in performance. As a last test, our methods were evaluated with two clinical IVOCT datasets.

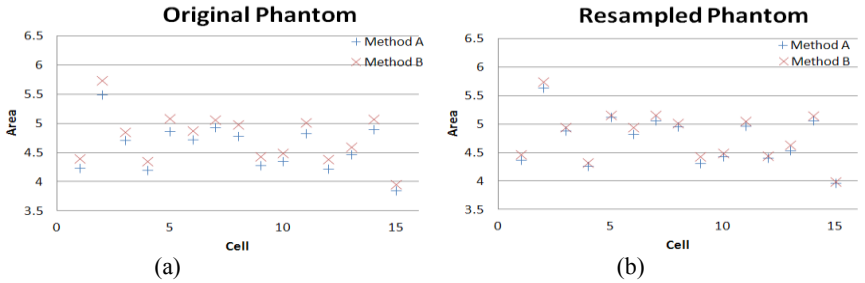

(a) (b)

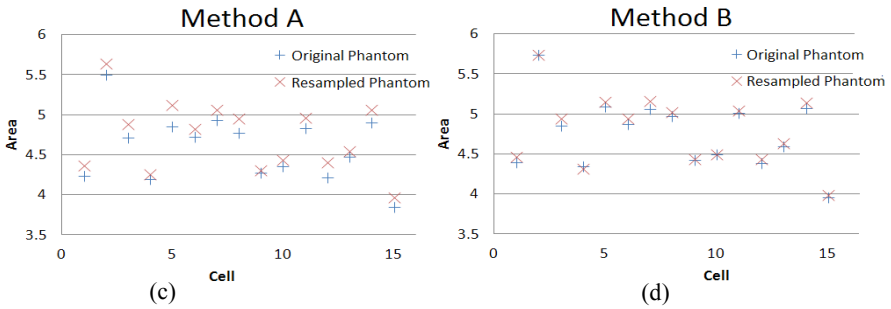

(c) (d)

Fig. 3. (a) shows the results of method *A* and *B* for the cell in the original phantom data set, and (b) the results from methods *A* and *B* for the re-sampled phantom data set. (c) shows the results from method *A* for the corresponding cells in both original and re-sampled phantoms, while (d) compares the results from method *B* for the corresponding cells in original and re-sampled phantoms

4 Analysis and Discussion

Table 1 shows that the ground truth of the whole stent surface area from method *B* is 71.27 mm^2 and the estimated result from method *A* is 68.82 mm^2. They are both close to the theoretical value (69.7 mm^2). Table 2 shows the quantitative analysis results of the cell area of the two clinical implanted stents. Compared with the original phantom data set, our methods present almost the same results from the re-sampled phantom data set. It suggests that our methods could be used to calculate the stent cell size in real IVOCT image sequences.

Fig. 3 shows that the results from method *A* are usually a little smaller than the ground truth results from method *B*. A possible explanation is that method *A* calculates the full cell size from the reconstructed stent surface that consists of thousands of small triangles, while method *B* calculates the stent cell using the opened surface from cylinder. For a curved surface, the opened surface should be bigger than the surface with triangle polygons.

Because the distributed stent struts do not fit to any common shape in 3D space, it is difficult to get the ground truth of cell area. Our methods provide an intuitive approximate measurement of the stent support to vessel walls.

IVOCT image sequences provide the longitude image data of the implanted stent along the imaging catheter. In practice, the imaging catheter may be bent with different angles. Without the 3D tracking of the imaging catheter, the cell area in IVOCT data may contain an error when the imaging catheter bends. However, in most cases, the trajectory of the imaging catheter has only smooth curvatures so that the error for distortion should be limited. Therefore, this method is expected to give out a good approximation of the stent cell area.

5 Conclusion and Future Work

The proposed methods can compute the full cell size and the MCUSA accurately for the support analysis of implanted stents. First a full resolution phantom dataset and its resampled dataset were used to evaluate the feasibility and the accuracy of our methods. Next, our methods were applied to two real IVOCT datasets. Quantitative evaluation results reveal that the methods have achieved high accuracy for the stent cell structure measurement and can be used for stent support analysis.

After automatic stent strut and guide wire detection, the imaginary stent contours are aligned using the stent centerline and then opened as a 2D mesh. This compensates for the difference in catheter position in the vessel during the pullback. Stent cells are then generated using this stent mesh.

In the future, we will work on stent distortion corrections, such as cardiac motion, take the width of the stent wire into account, detect the stent cell fully automatically and test our methods with more IVOCT data sets. We also plan to use these methods to calculation the coverage of the implanted stent to the side-branches.

References

1. Bosiers M, de Donato G, Deloose K, etc. Does free cell area influence the outcome in carotid artery stenting? Eur J Vasc Endovasc Surg. 2007;33(2):135-41
2. Gomez-Lara J, Brugaletta S, Diletti R, etc. A comparative assessment by optical coherence tomography of the performance of the first and second generation of the everolimus-eluting bioresorbable vascular scaffolds. Eur Heart J. 2011 Feb;32(3):294-304.
3. Meissner OA, etc. Intravascular optical coherence tomography: comparison with histopathology in therosclerotic peripheral artery specimens. J Vasc Interv Radiol. 2006;17:343-9.
4. Wang A, Eggermont J, Dekker N, Garcia-Garcia H, Pawar R, Reiber J.H.C., Dijkstra J Automatic stent strut detection in intravascular optical coherence tomographic pullback runs. Int J Cardiovasc Imaging 2012
5. Unal G., Gurmeric S., Carlier S.G., "Stent implant follow-up in intravascular optical coherence tomography images", The International Journal of Cardiovascular Imaging, Vol 26, No: 7, pp. 809-816, 2010.
6. Gurmeric S., Isguder G.G., Carlier S., Unal G., "A New 3-D Automated Computational Method to Evaluate In-Stent Neointimal Hyperplasia in In-Vivo Intravascular Optical Coherence Tomography Pullbacks", Lecture Notes in Computer Science, LNCS 5762, p. 776-786, MICCAI 2009.
7. Rosin PL, A note on the least squares fitting of ellipses, Pattern Rec. Lett., 14:799-8, 1993.
8. Hoppe H, DeRose T, Duchamp T, McDonald J, Stuetzle W. Surface reconstruction from unorganized points. ACM SIGGRAPH 1992 Proceedings, 71-78.
9. Lawlor G, http://www.bioengineering-research.com/software/vtkbioeng
10. Eberly D, Fitting 3D Data with a Cylinder. http://www.geometrictools.com/

Virtual deployment of pipeline flow diverters in cerebral vessels with aneurysms to understand thrombosis.

Leonardo Flórez-Valencia[1], Eduardo E. Dávila Serrano[2], Juan G. Riveros Reyes[1], Olivier Bernard[2], Jonas Latt[3], Orestis Malaspinas[3,4], Bastien Chopard[3], Guy Courbebaisse[2], and Maciej Orkisz[2]

[1] Grupo Takina, Departamento de Ingeniería de Sistemas, Pontificia Universidad Javeriana, Bogotá, Colombia
florez-l@javeriana.edu.co
[2] Université de Lyon, CREATIS; CNRS UMR 5220; INSERM U 1044; INSA-Lyon; Université Lyon 1, France
[3] University of Geneva, Computer Science Department, 1211 Geneva 4, Switzerland
[4] Institut Jean le Rond d'Alembert, CNRS UMR 7190; Université Pierre et Marie Curie - Paris 6, 4 place Jussieu - case 162, F-75252, France

Abstract. We present a prototype software to virtually deploy pipeline flow diverting stents in intracranial vessels with aneurysms. The final objective is to understand the biological and biomechanical mechanisms underlying the stent-induced clot formation within the aneurysm. The weaving pattern of the selected pipeline stent is described w.r.t. cylindrical coordinates. Patient-specific 3D vascular geometry is extracted by a level-set image segmentation algorithm. A deformable cylindrical simplex mesh model is used to simulate the virtual stent positioning. A continuous Right Generalized Cylinder model is then used to obtain the mapping of the stent geometry onto the deformed cylindrical surface. Meshes representing the vessel/aneurysm surface and the filaments of the stent are used as input to simulate the fluid dynamics without and with the virtual stent. Lattice Boltzmann method is used to solve the equations. We show preliminary visual results on a first patient.

1 Introduction

Rupture risk of intracranial aneurysms (IA) has been studied at length [23,25,7]. However, very little is known about the healing mechanism, namely the formation of a clot (thrombus) inside the aneurysm cavity after insertion of a stent. Spontaneous thrombosis has been observed and modeled in giant aneurysms [6], where it can reduce the risk of rupture and lead to healing, but has never been reported in smaller IA that can nevertheless disrupt with catastrophic consequences. In medical practice, various blood-flow diverting stents are used in an attempt to induce the thrombus onset. The physicians empirically choose the stent parameters and often superimpose more than one stent in order to achieve what they expect to be the appropriate density of the filaments.

Our project [4] aims at modeling multiscale interactions between biological and hemodynamic processes to better understand the thrombosis mechanisms in IA and how blood-flow diverting stents can influence the healing process. Here we focus on the part of the project related to the virtual insertion of a pipeline stent into the patient's vessels. Similarly to previous initiatives [10,12,17], our workflow starts by a patient's image segmentation to extract the vessel geometrical shape represented by a discrete three-dimensional mesh bound and a central axis. While the mesh represents the vessel wall, the axis is used to guide an interactive insertion of a virtual catheter that delivers the stent. Once the catheter has reached the delivery zone, a deformation algorithm "inflates" the model of the stent until it "touches" the vessel wall. A combination of the meshes representing the vessel endoluminal surface and the stent is then used as input for CFD simulations. The deformation of the stent model is controlled by internal and external forces. The former preserve the continuity and smoothness of the stent shape. They often are quite generic, based on parametric surface derivatives, like in [10], where a classical active surface model has been used. More sophisticated models, can include internal forces based on real properties of the filaments [17]. The external forces can include a "balloon" force that "inflates" the model, a force that attracts the model towards the edges in the image and/or a collision force that stops the evolution on the boundary of a presegmented vessel. We use the same deformable cylindrical simplex model as in [17], but we focus on a different type of stents, namely the pipeline flow diverters. Our prototype is based on CreaTools software development framework [1,2].

2 Method

The virtual insertion of the stent into the patient's vessels can be subdivided into three steps: preprocessing, generation of stent geometrical characteristics and virtual stent deployment. These steps build on two generic models that will be described prior to the presentation of the actual simulation.

2.1 Models

Static representations use a continuous model denoted by RGC (right generalized cylinder), whereas dynamic representations use a deformable model denoted by cylindrical simplex mesh.

Right Generalized Cylinder model. The RGC model [5,11,21] puts together a *continuous* axis and a *continuous* surface calculated from a stacking of discrete planar contours orthogonal to the centerline. It assumes that the cylinder segments between two contours are short enough to be described by constants. The very first contour of the stacking is described by its Fourier coefficients, the number of coefficients depending on the details desired. When only two coefficients are used, the cross-sectional shape of the cylinder is forced to be elliptical or

circular. The very first point of the axis is defined by an associated orthonormal frame, possibly rotated w.r.t. the Frenet frame. The axial shape (*i.e.* the evolution of the reference frame) between the consecutive contours is defined by a constant curvature, torsion and rotation, which means that such an axis segment is a helix. As for the Fourier coefficients describing the contours, they are assumed to evolve linearly within a given cylinder segment, so only their finite difference between two contours is needed to describe the surface of the whole segment, regardless its complexity. The RGC model has been used in the past both to generate computer phantoms of various cylindrical shapes and to reconstruct such shapes from image data, when associated with appropriate contour extraction method and tracking strategy.

Deformable Cylindrical Simplex mesh. This *discrete* model also associates an axis and a surface. Both are represented using N-dimensional k-simplex meshes [9,12,13], where each vertex has exactly $k+1$ neighbor vertices. To represent the surface we use a 3D 2-simplex mesh $\mathcal{S}_v = \left\{\mathbf{g}_j \in \mathbf{R}^3, 0 \leq j < J\right\}$, while a 3D 1-simplex mesh with radius r_i associated to each vertex $\mathbf{a}_i$ is used to represent the axis $\mathcal{C}_v = \left\{(\mathbf{a}_i, r_i) \in \mathbf{R}^3 \times \mathbf{R}^+, 0 \leq i < I\right\}$. The complete model includes $\mathcal{C}_v$, $\mathcal{S}_v$ and the spatial relationships between $\mathbf{a}_i$ and $\mathbf{g}_j$. According to the classical deformable model framework, the mesh deformation is controlled by two types of forces: 1) internal $\mathbf{f}_{int}(\mathbf{g}_j)$, the computation of which benefits from the specificity of the simplex-meshes formalism and uses a criterion enforcing the regularity of the surface curvature, and 2) external $\mathbf{f}_{ext}(\mathbf{g}_j)$ that can attract the model towards the edges in the image or push it outwards like a balloon force. Each surface vertex $\mathbf{g}_j$ is associated with the 3 closest axis vertices $\mathbf{a}_k$. When the surface undergoes a deformation, the axis bends accordingly through an external force $\mathbf{f}_{ext}(\mathbf{a}_k)$ resulting from the surface forces reported onto the axis. Conversely, the axis bending is reported onto the surface to ensure a homogeneous deformation behavior of the cylinder surface. The corresponding external force acting on the surface is a weighted sum of an axial component $\mathbf{f}_{axial}(\mathbf{g}_j)$ (each vertex tends to follow the axis global motion) and of a radial component $\mathbf{f}_{radial}(\mathbf{g}_j)$ (each vertex tends to align on a circle around the axis). The advantages of simplex-meshes are: fast computation (particularly when associated with QuadEdge implementation [15], possibility of managing the surface and the centerline within the same formalism, easy control of the 3D continuity and regularity of the surface, duality with triangulation (easy display). This model is therefore very well suited to the simulations.

2.2 Preprocessing

The preprocessing begins by manually selecting a volume of interest (VOI) within the original image, both to facilitate the visualization and interaction at the subsequent stages of the workflow, and to reduce the computational time. Subsequently, a segmentation algorithm automatically separates the aneurysm and vessels from the remaining tissues within the VOI. Various vessel segmentation

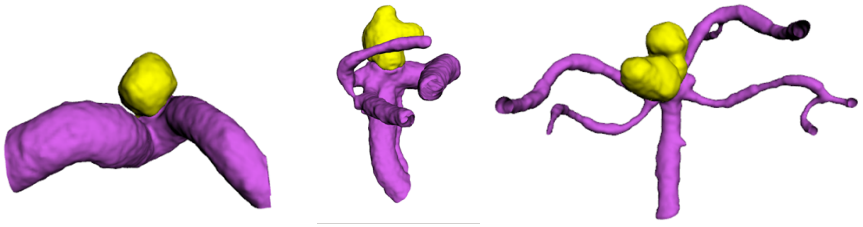

Fig. 1. Segmentation results with the aneurysm separated from the vessels.

algorithms can be tested at this stage. We have implemented three different level-set techniques based on different data attachment terms: optimal threshold [14], minimal variance [8] and a term specifically devised to extract thin structures [16]. Each of these methods only needs an interactive definition (click) of an initial point inside the aneurysm to start the segmentation process. The separation between the aneurysm and the vessels is performed by an improved version of the subjective-surface method from Sarti et al. [24] (Fig. 1).

Our simulation of the stent insertion needs the centerline of the vessel of interest to be used as guide-wire. Since some vessel-segmentation methods directly provide the centerline (see [18] for an overview), while others do not, we have included an option to extract the necessary centerline from the binary result of the segmentation. Actually, the extraction is performed within the segmented vessels after the exclusion of the aneurysm by the subjective-surface method. Usually, more than one vessel is present in the VOI. The vessel of interest is interactively selected by pointing its ends. The centerline is extracted between these points. To be consistent with the remaining steps, we used the formalism of the RGC model, although many other solutions might fit this step. Hence, contours of the binary vessel are progressively extracted, starting from one of the ends, and the RGC parameters are deduced from the consecutive contour pairs. In this way, both a centerline and a continuous surface representation closely fitting the vessel boundary become available.

2.3 Generating the stent geometry

Let us note that the stent geometry is needed at the very end of the virtual deployment process. Until that stage, only the overall cylindrical shape of the stent is manipulated, in order to simplify the interaction and display. However, both to graphically represent the final detailed shape of the stent, and to generate the corresponding mesh needed for further simulations, the actual geometry of the stent is to be defined. At that stage, the radius R and length L of the deployed stent (possibly different from the nominal values R_N and L_N) are already known. Before displaying a stent inserted into vascular structures and bent according to the vessel axial shape, it is necessary to generate a representation of a right stent, i.e. with an axis represented by a straight line.

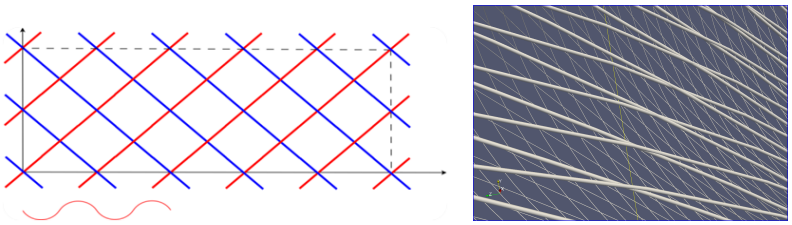

Fig. 2. Generating the stent geometry: schematic planar representation of filament centerlines (left), close-up of the 3D representation (right).

Here, the focus is on a specific type of pipeline stents, where the filaments are interlaced according to a predefined pattern. In addition to the interlacing pattern, a given stent is characterized by the number of filaments and by their thickness $2r$. We reproduce these characteristics in three steps. All these steps are performed using a planar rectangle $2\pi R \times L$ that bijectively maps onto a cylinder of length L and radius R. First, the centerlines of the filaments are drawn on the rectangle (Fig. 2 left). Each loop of each filament is represented by a straight line segment and these lines are parallel for all filaments turning in the same sense. These lines cross those representing the filaments that turn in the opposite sense. The angles formed by these lines between them and with the borders of the rectangle can easily be deduced from the number of filaments and the rectangle dimensions [20]. Second, the position of the lines is modulated in the direction orthogonal to the rectangle surface, to take into account the interlacing pattern. In the simplest case, where each filament alternatively passes above then below the other crossed filaments, this modulation can be sinusoidal with a magnitude equal to the filament radius r. The last step is to generate a cylindrical mesh around each filament's centerline, (Fig. 2 right).

2.4 Virtual stent deployment

Simulating the stent deployment involves two main steps: interactive choice of the delivery location and automatic "inflation" of the stent until its size fits the vessel diameter. An additional step maps the representation of the interlaced filaments onto the cylinder representing the deployed stent. While the first step is very simple and consists in sliding a thin cylinder along the vessel centerline until the desired location, as described in [12], the second step differs from the seminal work [12,13], although it also uses the same deformable cylindrical simplex model. As the stent is expected to keep the axial shape of the vessel, we relaxed the external force $\mathbf{f}_{ext}(\mathbf{a}_k)$. In the generic implementation of the model, this force transmits onto the axis a combination of external forces acting on the surface. Additionally, in the seminal work, the external force attracting the surface of the model was linked to the image intensity gradient. In our case, the vessels are already segmented, so this force was replaced by a "balloon" force that "inflates" the surface mesh. The inflation does not involve axial displacements of

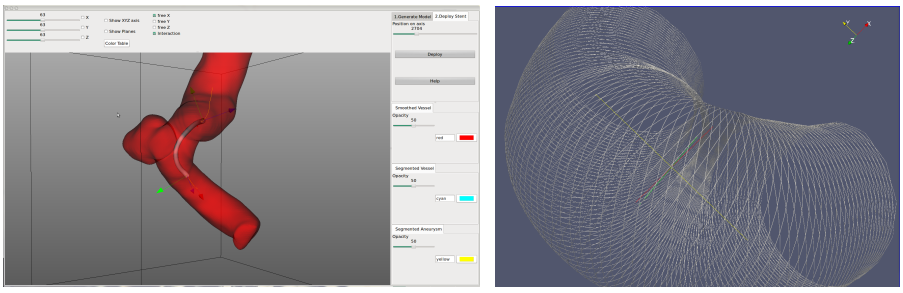

Fig. 3. Stent deployment. Left: graphical user interface with a display of a segmented vessel, aneurysm and folded stent placed along the centerline. Right: unfolded stent.

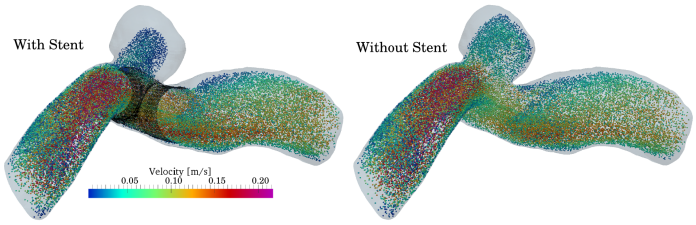

Fig. 4. Example of CFD simulation with and without stent.

the surface nodes, so the force component $\mathbf{f}_{axial}(\mathbf{g}_j)$ also became useless, while the component $\mathbf{f}_{radial}(\mathbf{g}_j)$ is driven by the nominal radius R_N and enforces a circular cross-sectional shape. The evolution of the deformable model stops when one of the surface nodes collides with the vessel boundary. The final radius, length and axial shape of the simplex mesh are used to calculate a continuous cylindrical surface described by the RGC model. This in turn is used to infer the actual spatial coordinates of the filaments, according to the bijective mapping between the previously described planar representation and the cylindrical surface (Fig. 3). The resulting mesh representation is combined with the mesh representing the vascular surface, so that the whole can be used to simulate the blood flow modified by the presence of the stent.

3 Results

The first experiments aimed at demonstrating the correct interoperability of all the components of the workflow leading to plausible results. To this purpose, we first simulated the insertion of a pipeline stent with 48 wires, filament diameter 0.027 mm, $R_N = 1.36$ mm then the Navier-Stokes equations were solved by using the lattice Boltzmann method [22] implemented in Palabos software [3]. More precisely, 3D and 4D BGK lattice Boltzmann codes were used with the Carreau-Yasuda constitutive law [19]. Figure 4 shows a result of a BGK D3Q19 simulation with the following parameters: mean velocity 0.05 m/s, Reynolds number 200,

inlet diameter 4 mm, number of lattice grid nodes larger than 40 million, number of cores for parallel computation 120. Particles virtually injected into the blood are displayed with colors representing their velocity. As expected, the presence of a virtual stent significantly reduced the velocities within the aneurysmal cavity. Indeed, densely woven filaments constitute an obstacle for the blood flow, despite their very tiny diameters. The calculated surface coverage was 31.1%.

Our numerical simulation fully resolved the structure of the stent and the flow around the filaments of the stent, unlike a more common approach, in which the effect of the stent was approximated by a model of porous media. A huge resolution of the flow mesh was necessary to achieve this aim, because the diameter of the stent filaments differs from the diameter of the artery by three orders of magnitude. The code used for the simulations was efficiently parallelized: not only the actual CFD simulation, but also the generation of the computational mesh and the post-processing of the data.

4 Conclusions and Perspectives

We have implemented a complete workflow to perform a virtual stenting of intracranial aneurysms using pipeline flow diverters. The prototype used generic components both to construct the models and to build up the graphical user interface. The first results demonstrated a good interoperability of these components and the resulting meshes proved to be exploitable in CFD simulations. These simulations have been carried out using software based on the Lattice Boltzmann method. The resulting flow patterns clearly depict the influence of the stent on the blood velocities within the aneurysm. These results now need to be correlated with the findings in the biological and clinical domains. It is expected that these experiments will allow us to use the simulations to predict *a priori* the outcome of various stenting strategies.

Acknowledgements

This work has been partly funded by the E.C. via VPH STREP Thrombus FP7-ICT-2009-6-269966, as well as by the ECOS Nord Commitee grant C11S01.

References

1. `http://toolkit.vph-noe.eu/home/tools/imaging/creatools.html`.
2. `http://www.creatis.insa-lyon.fr/site/en/CreaTools_home`.
3. `http://www.palabos.org`.
4. `http://www.thrombus-vph.eu`.
5. J. Azencot and M. Orkisz. Deterministic and stochastic state model of right generalized cylinder (RGC-sm): application in computer phantoms synthesis. *Graph. Models*, 65(6):323–350, 2003.
6. R. D. Brownlee, B. I. Tranmer, R. J. Sevick, G. Karmy, and B. J. Curry. Spontaneous thrombosis of an unruptured anterior communicating artery aneurysm : an unusual cause of ischemic stroke. *Stroke*, 26(10):1945–1949, 1995.

7. J. R. Cebral, M. A. Castro, J. E. Burgess, R. S. Pergolizzi, M. J. Sheridan, and C. M. Putman. Characterization of cerebral aneurysms for assessing risk of rupture by using patient-specific computational hemodynamics models. *Am. J. Neuroradiol.*, 26(10):2550–2559, 2005.
8. T. F. Chan and L. A. Vese. Active contours without edges. *IEEE Trans. I.P.*, 10(2):266–277, 2001.
9. H. Delingette. General object reconstruction based on simplex meshes. *Int. J. Comput. Vision*, 32(2):111–146, 1999.
10. J. Egger, S. Grosskopf, C. Nimsky, T. Kapur, and B. Freisleben. Modeling and visualization techniques for virtual stenting of aneurysms and stenoses. *Comput. Med. Imaging Graph.*, 36(3):183–203, 2012.
11. L. Flórez-Valencia, J. Azencot, and M. Orkisz. Algorithm for blood-vessel segmentation in 3D images based on a right generalized cylinder model: application to carotid arteries. In *Int. Conf. Comput. Vision Graph.: Part I, Warsaw, Poland*, volume 6374 of *LNCS*, pages 27–34, Berlin, Heidelberg, 2010. Springer-Verlag.
12. L. Flórez-Valencia, J. Montagnat, and M. Orkisz. 3D graphical models for vascular-stent pose simulation. *Mach. Graph. Vis.*, 13(3):235–248, January 2004.
13. L. Flórez-Valencia, J. Montagnat, and M. Orkisz. 3D models for vascular lumen segmentation in MRA images and for artery-stenting simulation. *Innov. Technol. Biol. Med. - IRBM*, 28(2):65–71, 2007.
14. R. Gan, W. C. K Wong, and A. C. S. Chung. Statistical cerebrovascular segmentation in three-dimensional rotational angiography based on maximum intensity projections. *Med. Phys.*, 32(9):3017–3028, 2005.
15. A. Gouaillard, L. Flórez-Valencia, and E. Boix. ItkQuadEdgeMesh: a discrete orientable 2-manifold data structure for Image Processing. *Insight Journal*, 2006.
16. M. Holtzman-Gazit, R. Kimmel, N. Peled, and D. Goldsher. Segmentation of thin structures in volumetric medical images. *IEEE Trans. I.P.*, 15(2):354–363, 2006.
17. I. Larrabide, M. Kim, L. Augsburger, M. C. Villa-Uriol, D. Rüfenacht, and A. Frangi. Fast virtual deployment of self-expandable stents: method and in vitro evaluation for intracranial aneurysmal stenting. *MedIA*, 16(3):721–730, 2012.
18. D. Lesage, E. D. Angelini, I. Bloch, and G. Funka-Lea. A review of 3D vessel lumen segmentation techniques: models, features and extraction schemes. *MedIA*, 13(6):819–845, 2009.
19. O. Malaspinas, G. Courbebaisse, and M. O. Deville. Simulation of a generalized Newtonian fluid by the Lattice Boltzmann Method. *Int. J. Modern Phys. C*, 18(12):1939–1949, 2007.
20. P Mortier, M De Beule, D Van Loo, P Verdonck, and B Verhegghe. Parametric stent design using pyFormex. In *ASME 2008 Summer Bioeng. Conf.*
21. M. Orkisz, L. Flórez-Valencia, and M. Hernández Hoyos. Models, algorithms and applications in vascular image segmentation. *Mach. Graph. Vis.*, 17(1):5–33, 2008.
22. R. Ouared and B. Chopard. Lattice Boltzmann simulations of blood flow: non-Newtonian rheology and clotting processes. *J. Stat. Phys.*, 121(1-2):209–221, 2005.
23. G. J. E. Rinkel, M. Djibuti, A. Algra, and J. van Gijn. Prevalence and risk of rupture of intracranial aneurysms: a systematic review. *Stroke*, 29(1):251–256, 1998.
24. A. Sarti, R. Malladi, and J. A. Sethian. Subjective surfaces: a geometric model for boundary completion. *Int. J. Comput. Vision*, 46(3):201–221, 2002.
25. D. O. Wiebers. Unruptured intracranial aneurysms: natural history, clinical outcome, and risks of surgical and endovascular treatment. *The Lancet*, 362(9378):103–110, 2003.

Intracranial stent visualization for image guided interventions and therapy

Daniel Ruijters, Peter van de Haar, Ruben Roijers, Niels J. Noordhoek, Jan Timmer, and Drazenko Babic

interventional X-Ray, Philips Healthcare, the Netherlands,
danny.ruijters@philips.com

Abstract. In intracranial interventional treatment there is currently an increased interest in applying stents with a very low X-ray radiopacity. These types of stents are nearly invisibility in standard 2D imaging. Flat Detector Computed Tomography (FDCT) CT offers a solution in imaging these stents peri-interventionally, and has become increasingly popular within minimally invasive endovascular interventions. Recent innovations in FDCT acquisition and 3D reconstruction techniques have considerably improved the feasibility to visualize stents that possess very little radiopacity. However, stents that are placed adjacent to aneurysms filled with coils lead to reconstructed images that are severely distorted by streaking artifacts, caused by the metal coils. In this article, results are presented regarding the FDCT acquisition and visualization of intracranial stents and the reduction of streaking artifacts in a second pass reconstruction.

1 Introduction

In recent years the imaging capabilities of flat-detector C-arm X-ray systems have been improved. These systems are essentially the eyes of the physician during stent navigation, placement and deployment. Technical developments such as Flat-Detector Computed Tomography (FDCT) for imaging of the vasculature and soft-tissue offer a previously unprecedented high quality visualization of anatomy and devices during interventional treatment [1, 2]. Also algorithmic developments, like metal artifact reduction techniques, have contributed to the advances with respect to intracranial stent visualization. These developments offer the possibility to inspect the stent deployment with respect to the vessel lumen and intravascular plaques. On the other hand, recent developments in stent technology have lead to stents, e.g. Nitinol stents, which are increasingly difficult to visualize. In this article, we will discuss the technological advances with respect to intracranial stent placements and the associated challenges.

2 FDCT for soft-tissue imaging

Flat-detector cone-beam CT is primarily used to assess the soft-tissue structures during interventional treatment. The FDCT data is acquired using a neuroangiographic X-ray C-arm (Allura Xper FD20; Philips Healthcare, Best, the

Netherlands), equipped with a cesium iodide - amorphous silicon flat panel detector. The sensor area of the flat detector measures approximately 30 x 40 cm and consists of 1920 x 2480 pixels. The cone beam acquisition protocol consists of a rotational trajectory over a 200 arc while acquiring 620 projection images. The source-to-detector distance is 1195 mm. The objects of interest should be positioned in the center of rotation, 810 mm from the source. The X-ray tube voltage is set to 120 kV, the focal spot to 0.7 mm, and a copper filter of 0.4 mm is used. The associated radiation dose ranges from 45 to 49 mGy CTDI dose. Pre-processing steps of the projection images include gain correction, scatter correction, water beam-hardening correction, and Parker weighting [3]. The 3D reconstruction is obtained using the Feldkamp-Davis-Kress method [4]. Figure 1 presents a reconstruction of a Catphan phantom showing the contrast resolution for inserts of various sizes. As can be observed, 5 HU differences are still visible for larger inserts [5].

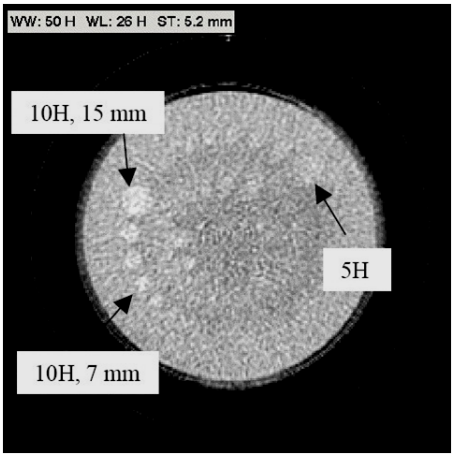

Fig. 1. XperCT reconstruction of a Catphan phantom with inserts of different contrast and sizes [5].

3 High resolution FDCT

While the previously described cone-beam CT protocol is very well suited for soft-tissue imaging, it is sub-optimal for stent imaging. For the purpose of imaging intracranial stents and their surrounding vasculature a dedicated acquisition protocol and reconstruction settings were developed (VasoCT; Philips Healthcare, Best, the Netherlands). The high resolution protocol also consists of 620 projection images, but the imaged detector area is fixed to a diameter of 22 cm with a pixel size of 0.154 mm, allowing very high spatial resolution 3D reconstructions. The X-ray tube voltage is set to 80 kV, the focal spot to 0.4 mm,

while no copper filter is being used. Figure 2 compares the soft-tissue and the high resolution protocols in a porcine in-vivo acquisition [3]. Figure 3 shows a stent acquired in an in-vitro setup, using the soft-tissue and the high resolution protocols [6]. The high resolution protocol can be combined with the injection of iodine contrast medium (either an intravenous injection, or an on-site intracranial injection of diluted contrast), in order to inspect the interface of the stent and vessel lumen. In this manner it is possible to assess whether the stent has been properly deployed.

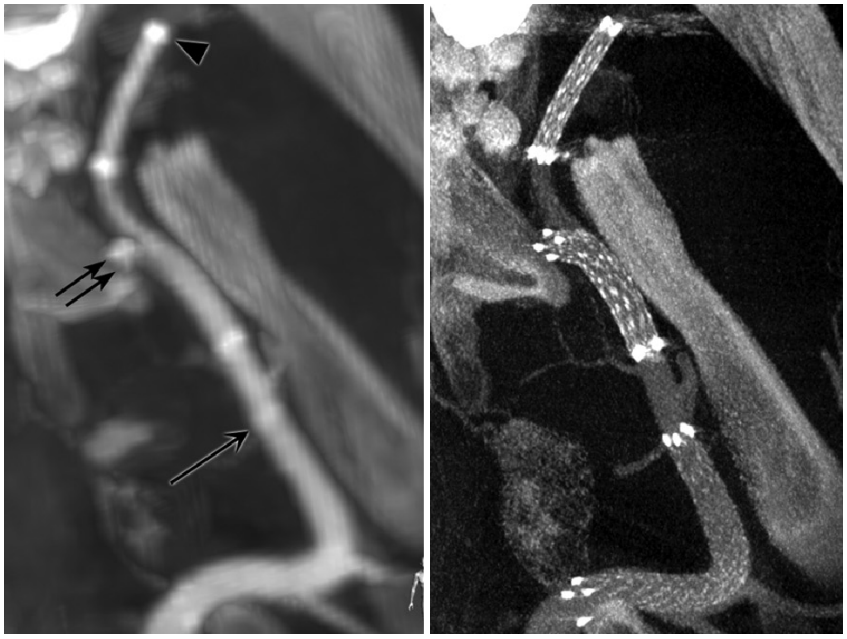

Fig. 2. Left: standard XperCT acquisition of stents placed in a swine model, Right: high resolution acquisition of the same part. Adapted from Patel *et al.* [3].

4 Metal Artifact Reduction

In the first step of the Metal Artifact Reduction (MAR) algorithm [7] a regular filtered back-projection reconstruction is produced [4]. From this reconstruction the volumetric regions that display high X-ray absorption are isolated, using a predefined threshold. These regions are then forward projected [8] on the original X-ray images, in order to identify the high-absorption areas in the images. In the second pass, the identified areas in the original X-ray images are replaced by linearly interpolated grey-values from the surrounding scan lines (see Figure 4).

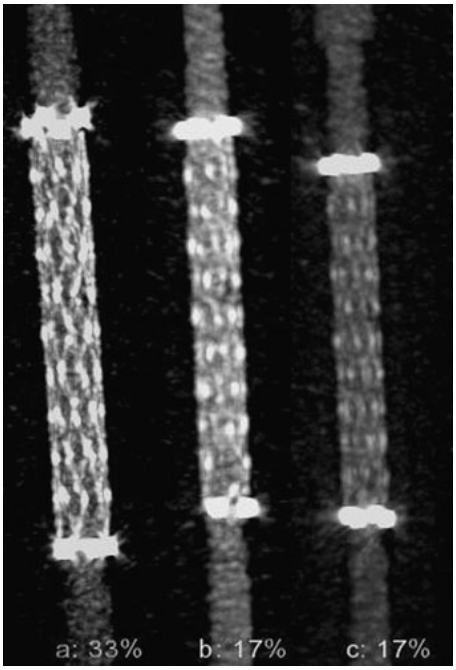

Fig. 3. A Wingspan nitinol stent. A comparison between a high-resolution/high-contrast case, b standard resolution/ high-contrast case, and c the standard resolution/standard contrast case. In all cases, an intra-tube high-density contrast agent of 550 HU was applied [6].

Fig. 4. The high-absorption areas in the rotational X-ray acquisition images (arrows: coils, teeth fillings) have been replaced by linear interpolation of their surrounding scan line values.

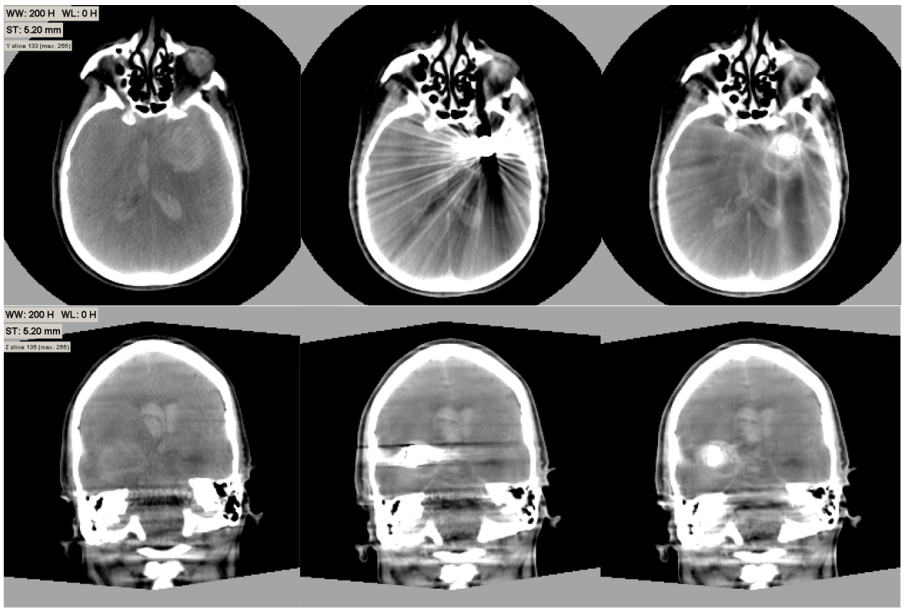

Fig. 5. Left images: reconstruction prior to coiling. Middle images: reconstruction post coiling, without MAR. Right images: same acquisition in the middle, but the reconstruction has been performed with MAR.

From these merged images a new filtered back projection reconstruction is calculated in the second pass. The entire process of two passes is performed within about 150 seconds.

The effect of the MAR technique is illustrated in Figure 5. From the same patient a FDCT acquisition was made prior and post coiling an aneurysm. The 3D reconstruction of the prior coiling acquisition obviously does not display any streaking artifacts. The post coiling reconstruction is severely distorted with streaking artifacts in the reconstruction without MAR. The post coiling reconstruction with MAR clearly suffers far less from streaking artifacts.

The MAR procedure significantly reduces the presence of metal streaking artifacts caused by coils placed in aneurysms. This allows the investigation of the tissues and anatomical structures adjacent to the coiled volume. In case of stent/coils combinations this is especially valuable, since the streaks tend to obscure the intracranial stent in the reconstruction plane.

MAR cannot fully remove all metal artifacts. Typically, some streak-artifacts remain. The intensity of the remaining streaks depends on complexity of nearby anatomy (like bone structures), size of metal object etc. Soft-tissue imaging of very low-contrasts will still suffer from artifacts, but the artifact level is significantly reduced. Overall the diagnostic value of the MAR reconstructed images is greatly enhanced.

Fig. 6. High resolution reconstruction with coiled aneurysm and stent. Left: without metal artifact reduction, Right: with metal artifact reduction applied.

Particularly, when diluted iodine contrast medium has been administrated, enabling the examination of the vascular morphology, the streaking artifacts severely disturb the evaluation of the aneurysm neck. Furthermore, false vessel bifurcations and branches may be introduced by the streaking artifacts. The MAR procedure largely resolves these disturbing phenomena. It removes the false bifurcations and branches, and enables the clear visualization of the aneurysm neck, see Figure 6. The high resolution reconstruction also allows assessing the stent placement and deployment with respect to the vessel lumen.

5 Conclusions

Several technical advancements have been presented with respect to intracranial stent imaging during minimally invasive image guided interventional treatment. Flat Detector cone-beam CT enables to assess the soft-tissue structures in a peri-interventional setting. Though the contrast resolution up to 5 HU is already acceptable for many applications, it is still not good enough to detect fresh small hemorrhages, although larger bleedings can be observed.

The high resolution protocol enables an unprecedented high spatial 3D resolution for assessment of intracranial stent deployment. Vessel lumen, plaque, and intravascular devices are clearly visualized with well defined interfaces with as result better outcome control leading to a more successful endovascular treatment.

The employment of metal artifact reduction in coiled aneurysms combined with stent placement significantly increases the accuracy of the procedure, since it enables, for the first time, a correct assessment of stent location and deployment in the catheterization laboratory.

Especially, the combination of the high resolution acquisition protocol together with metal artifact reduction proves to be valuable during minimally invasive endovascular intracranial stent placement for stents that are placed adjacent to coiled aneurysms (as can be seen in Figure 6), since the high resolution protocol enables the visualization of the very fine stent struts, while the metal artifact reduction considerably reduces the streaking artifacts which otherwise may hamper the inspection of the deployment of the stent.

References

1. Söderman, M., Babic, D., Holmin, S., Andersson T: Brain imaging with a flat detector C-arm, Technique and clinical interest of XperCT. Neuroradiol 50:863-868 (2008)
2. Kamran, M., Nagaraja, S., Byrne, J.V.: C-arm flat detector computed tomography: the technique and its applications in interventional neuro-radiology. Neuroradiol 52:319-27 (2010)
3. Patel, N.V., Gounis, M.J., Wakhloo, A.K., Noordhoek, N., Blijd, J., Babic, D., Takhtani, D., Lee, S.-K., Norbash, A.: Contrast-Enhanced Angiographic Cone-beam CT of Cerebrovascular Stents: Experimental Optimization and Clinical Application. AJNR 32:137-144 (2011)
4. Feldkamp, L.A., Davis, L.C., Kress, J.W.: Practical cone-beam algorithm. J Opt Soc Am A1:612-19 (1984)
5. Noordhoek, N.J., van de Haar, P.G., Timmer, J.: Direct comparison of commercially available C-arm CT to multislice CT image quality. Proc. RSNA, Chicago, USA (2006)
6. Snoeren, R.M., Söderman, M., Kroon, J.N., Roijers, R.B., de With, P.H.N., Babic, D.: High-resolution 3D X-ray imaging of intracranial nitinol stents. Neuroradiology 54(2):155-162 (2012)
7. Prell, D., Kyriakou, Y., Struffert, T., Dorfler, A., Kalender, W.A.: Metal Artifact Reduction for Clipping and Coiling in Interventional C-Arm CT. AJNR Am J Neuroradiol 31:634-39 (2010)
8. Ruijters, D., ter Haar Romeny, B.M., Suetens, P.: GPU-Accelerated Digitally Reconstructed Radiographs. Proc. IASTED BioMed:431-435 (2008)

3D+t/2D+t CTA-XA registration using population-based motion estimates

N. Baka[1,2], C.T. Metz[1], C. Schultz[1], L. Neefjes[1], R.J.van Geuns[1], B.P.F. Lelieveldt[2,4], W.J. Niessen[1,4], M. de Bruijne[⋆1,3], and T. van Walsum[⋆1]

[1] Erasmus MC, Rotterdam, The Netherlands n.baka@erasmusmc.nl
[2] Leiden University Medical Center, Leiden, Netherlands
[3] University of Copenhagen, Denmark
[4] Delft University of Technology, The Netherlands

Abstract. Success rates of minimally invasive coronary interventions for chronic total occlusions may increase if the pre-operative cardiac CT angiography (CTA) could be overlayed on the intra-operative X-ray coronary angiography images. It was previously shown that incorporating patient specific coronary motion extracted from 4D CTA in the CTA-XA registration increases the robustness of the alignment. However, pre-operative CTA is often acquired with gating at end-diastole, in which case patient specific motion is not available.
Therefore, we investigate the possibility of using population based coronary motion estimates rather than the CTA based motion for the 3D+t/2D+t registration. We propose a methodology for building population based average and predicted motion from 4D CTA datasets, and use these models to perform 3D+t/2D+t registration on one cardiac cycle of 12 monoplane XA sequences. The registration performance of the population based motion estimates was better than the static no motion case, but not as good as the patient-specific 4D CTA based motion.

1 Introduction

Percutaneous coronary intervention (PCI) is routinely performed for treating coronary artery stenosis. High success rates (99%) have been reported for PCI on non-occluding stenosis. These rates drop to 60-80% in the case of treatment of chronic total occlusions (CTOs) [10]. CTOs can not be fully visualized with XA as the contrast agent does not pass the occluded segment, which hampers percutaneous treatment. Pre-operative 3D CT angiography (CTA) can be used to visualize the entire cardiac vasculature including occluded segments, and calcifications. The combined visualization of the information from CTA and XA during the PCI procedure may increase the success rate of CTO treatment. As a prerequisite, the spatial relation between the pre-operative 3D and intra-operative 2D+t imaging data needs to be known.

Many authors have addressed registration of a 3D coronary artery tree with its monoplane projection images. Non-rigid registration techniques have been

⋆ Both last authors contributed equally.

proposed for single time-frame reconstructions [5, 9], though their performance has not been evaluated on sequences. Bouattour et al. performed frame-by-frame B-spline based 2D-3D registration of a sequence, using the previous frame's fit as initialization for the next [3]. They reported a success rate of 56% on the evaluated three sequences. Metz et al. proposed simultaneous registration of all frames of a cardiac cycle, using the cardiac motion derived from 4D CTA data [7]. They showed an increase in registration robustness compared to 2D-3D fitting of only the end-diastolic XA frame. In clinical practice, however, information on the motion of the coronary arteries is often not available, as CTA images are typically acquired within a limited part of the cardiac cycle in order to minimize radiation dose. Previous work showed that the patient specific *cardiac* motion could be predicted to a certain accuracy using population based estimates and the end-diastolic cardiac shape [6]. In this work we developed a methodology to create population based *coronary artery* motion estimates, and investigate the applicability of the so calculated mean and predicted motion for 3D+t/2D+t registration of 3D end-diastolic CTA images and XA sequences.

2 Method

Two population based motion estimates are investigated. The first is the mean motion from a set of training data. The second is a motion estimate based on the shape of the heart. We first describe how we derived these motion estimates from the training data (Section 2.1) and then explain the registration framework (Section 2.2) in which the different motion estimates were evaluated.

2.1 Mean and predicted coronary motion

Estimating population based coronary artery motion from a training set of 4D centerlines is very challenging due to variations in coronary topology. Therefore, we propose to model the coronary motion in terms of nearby cardiac surface landmark points, with the pre-requisite, that all training shapes are represented by landmark points corresponding to the same anatomical positions. Every training shape containing the four cardiac chambers and the aorta was segmented from 4D CTA scans, by segmenting the end diastolic phase using atlas-based segmentation and propagating this segmentation to the entire 4D sequence using 4D image registration [6]. This procedure results landmarked surface segmentations, as all atlases were represented by corresponding landmark points. Subsequently, a temporal alignment based on left ventricular volume curves was applied to accommodate for heart rate differences. For every test patient, the cardiac structures were segmented in the end diastolic image by atlas-based segmentation resulting in a surface with point correspondence to the training shapes. Coronary centerlines were extracted using a minimum cost path approach between manually defined start and end points [7], and were refined using lumen segmentation [8]. For every centerline point the 30 closest surface landmark points were selected, as illustrated in Figure 1. The training surfaces were then rigidly

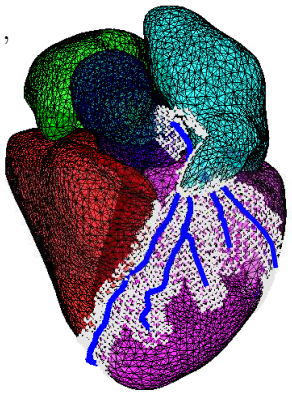

Fig. 1. End diastolic heart segmentation with coronary arteries (blue) and the selected nearby landmark points (white).

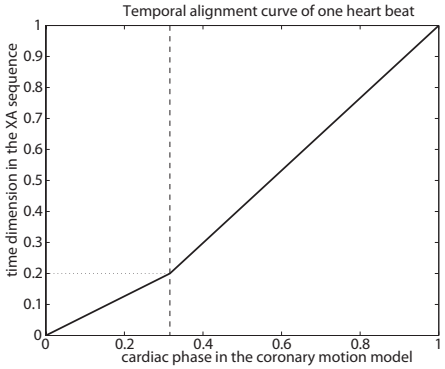

Fig. 2. Temporal transformation function relating time points in the motion model frames in the XA sequence. Intermediate phases and frames are calculated with linear interpolation.

(+isotropic scaling) aligned on these selected landmark points. The coronary artery motion was subsequently estimated from all 4D training segmentations by calculating for every centerline point the weighted average motion of the selected closest surface landmarks. Motion was defined as the coordinate deviation from the end diastolic position, and weights were defined by a negative exponential function of the landmark-centerline distance.

Finally, we calculated the mean coronary artery motion by averaging the motion estimates for the training set. We also calculated the predicted coronary artery motion based on the end diastolic shape, which was shown to outperform mean motion for cardiac motion estimation [6]. We employed ridge regression for prediction, as that was shown to be most accurate in the high dimensional low sample size setting [2].

2.2 2D+t/3D coronary centerline registration

During registration we minimize the distance between the projected 3D vessel centerline and automatically extracted 2D vessel centerlines in the XA image. The 3D vessel centerline is projected to the image plane based on the geometry of the X-ray imaging system and the patient position. The 2D vessel centerlines were extracted from the X-ray images by first enhancing dark longitudinal structures with a Frangi vesselness filter using three scales [4]. Subsequently, ridges were found via local non-maximum suppression, and hysteresis thresholding. Finally, single pixel long centerlines were removed. An example of this procedure is shown in Fig. 3.

,

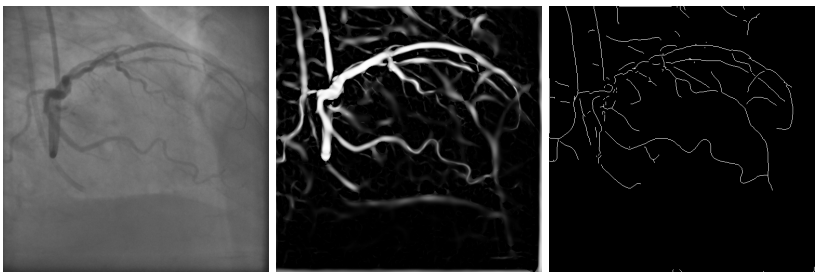

Fig. 3. An example of an XA frame, its veselness filtered image, and the automatically extracted centerline image.

We register a complete cardiac cycle by minimizing a cost function G, which is the sum of all frame-wise 2D-3D distances:

$$G = \sum_{t=1}^{L} G_T(t) \quad , \tag{1}$$

where L is the number of frames in the cardiac cycle, and $G_T(t)$ is calculated as the weighted average of minimal distances between projected 3D centerline points, and extracted 2D centerline points at time point t

$$G_T = \frac{1}{\sum_{i=1}^{N} w_i} \sum_{i=1}^{N} w_i \min_j \Theta_{ij} \quad , \tag{2}$$

where Θ_{ij} is the distance function, N is the number of 3D centerline points, and weights w_i encode the distance of the vessel point i from its neighbors in the projection. This weighting ensures that all vessels have a similar influence on the optimization, independent of their orientation with respect to the projection direction. Centerline points outside the FOV are disregarded. The distance function Θ_{ij} is adapted from [1], and comprises a 2D Euclidean distance and an orientation difference. We enriched this measure with the Frangi vesselness score F_j at extracted centerline points j, such that

$$\Theta_{ij} = \alpha(1 - F_j) + (1 - |\cos\gamma_{ij}|\ e^{-\frac{D_{ij}^2}{\sigma^2}}) \quad , \tag{3}$$

where D_{ij} is the 2D Euclidean distance between projected vessel point i and centerline point j, and γ_{ij} is the angle between the 2D centerline direction and projected 3D vessel direction. The constant α regulates the importance of the vesselness term in the distance measure. Due to the exponential function all distances D_{ij} are mapped to the [0,1] interval, resulting in small gradients for large distances. The parameter σ regulates this non-linear behavior.

Minimization of the distance G is performed by optimizing three groups of parameters: heart pose parameters relating the CT coordinate system with the angiography coordinate system, respiratory motion parameters, and temporal

alignment parameters. The temporal alignment relates the cardiac phases of the motion model to the XA frames, accounting for differences in temporal resolution and heart rate. As heart rate influences the relative duration of systole and diastole, a piecewise linear function is proposed for the temporal alignment, with one parameter representing the relative length of systole in a cardiac cycle. The function is shown in Figure 2, with phases parameterized between 0 and 1.

We model the respiration induced coronary artery movement as a quadratic function through time. The induced rigid motion from the first frame is set by the optimizer at the center and the end of the cardiac cycle, and interpolated in-between.

3 Data

Training data The 4D heart segmentations from [6] were used to build the statistical motion models of the coronary arteries. The data consisted of 151 ECG-gated 4D CTA images reconstructed at every 5% of the cardiac cycle, acquired as part of the clinical diagnosis of patients, at voxel sizes of approximately 0.7x0.7x0.9 mm^3.

Test data For evaluation, 12 XA datasets of 10 patients (two patients underwent two interventions) were used [7], five of which contained the right, the others the left coronary artery. Every patient in the test set underwent a 4D CTA scan prior to PCI. These CTA scans were also part of the training data described in the previous subsection. The 4D coronary artery centerlines were extracted by first extracting the centerlines at end diastole (see Section 2.1), and then propagating these to the other cardiac phases [7].

4 Experiments and results

4.1 Coronary motion model evaluation

We first investigated the mean and predicted coronary artery motion estimates, independent of the task of 2D+t/3D registration. In these experiments, the coronary artery locations extracted from the 4D CTA datasets of the 10 test patients, were used as ground truth.

First, we evaluated how well the cardiac surface based motion estimate approximated the 4D CTA derived motion. The frame-wise root mean square (RMS) point-to-point distance seemed to be independent of cardiac phase, and averaged to 0.53 mm.

Second, we evaluated how well the mean and predicted motion is able to approximate the 4D CTA motion. The parameter λ of the ridge regression was optimized on the training set excluding the test subjects. Resulting lambda values were around 250. Results, including the static case in which motion is completely ignored, are shown in Tab. 1, and indicate that the predicted motion may outperform the mean motion, however, the difference was not statistically significant at the 5% significance level according to a paired t-test.

Table 1. 3D-4D reconstruction accuracy of the motion estimates. We report the average and standard deviation of the 3D point-to-point errors of all phases.

	Accuracy [mm]
Predicted motion	2.29 ± 0.43
Mean motion	2.52 ± 0.74
Static	4.4 ± 1.39

4.2 2D+t/3D registration evaluation

All registrations were performed nine times with different manual initializations. For initialization, three observers translated the end-diastolic coronary artery in the projection plane (2 DoF) to optimize the match with the first angiographic frame of the cardiac cycle.

The XA data contained images of patients with metallic stitches from previous heart surgeries, and in some cases the guiding catheter was visible in the field of view (FOV). We therefore performed semi-automatic stitch and catheter removal in a preprocessing step using morphological closing on the image intensities.

For evaluation purposes, we adapted the centerline distance measure from [7]. First, centerline segments were manually drawn on the XA frames. The corresponding closest projected 3D centerline branch for every annotated centerline segment was determined, and subsequently the distances of all points in the annotated centerline segment to the projected 3D centerline branch were calculated. The root mean square (RMS) distance of all annotated centerline points resulted in the corresponding centerline distance measure for each frame.

Figure 4 shows the median centerline distance of all frames, and their spread. To check for statistical significance, we averaged all results per patient, and applied a paired Wilcoxon signed rank test on these averages. Significant differences between the proposed methods and the 4D CTA motion based fitting are reported at the 5% significance level in Tab. 4 as bold typeset. All results were significantly different from the initialization, which had a median centerline distance of 3.88 mm when applying the mean motion. An example frame is shown in Fig. 5.

5 Discussion and Conclusions

We investigated the possibility of replacing patient-specific 4D CTA derived coronary motion by population based average and predicted coronary motion in the context of 3D+t/2D+t alignment of pre-operative CTA and intra-operative X-ray images.

We proposed to build the population based motion estimates by interpolating coronary artery motion from the motion of nearby cardiac structures. Using this representation, coronary artery motion could be represented with an average root mean square point-to-point accuracy of about half a mm, which is smaller than the voxel size of the CTA scans.

,

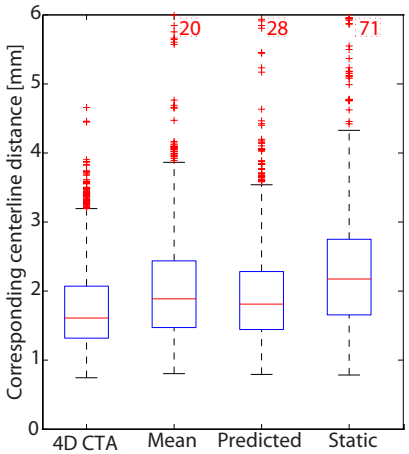

Motion	Accuracy [mm]
4DCT	1.82
Mean	**2.15**
Predicted	2.09
Static	**2.65**

Fig. 4. The 2D corresponding centerline distances after 3D+t/2D+t registration. Left: boxplot of all frames, red numbers give the number of frames outside the shown range, Right: Median distance values. Bold numbers indicate significant differences with the 4DCT results.

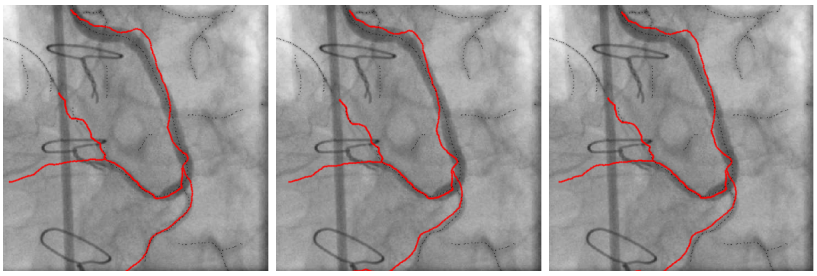

Fig. 5. Example registrations on an end-systolic frame. From left to right: 4D CTA based motion, mean motion, predicted motion. Accuracies: 1.31, 1.55, 1.51 mm

In the context of the 2D+t/3D registration task, the predicted motion estimate resulted in slightly better results than the mean motion estimate. While the mean motion performed statistically significantly worse than the 4D CTA based motion for registration, the predicted motion did not show a statistically significant difference. However, its median error was larger than that of the 4D CTA based motion.

Future work will focus on building and registering statistical coronary artery motion models rather than fixed motion estimates. Also, further investigation is needed to ensure the generality of the obtained results to other 2D-3D distance metrics.

This paper proposed the construction of population based mean and predicted coronary motion estimates. We evaluated the registration performance of these estimates, and conclude that population based motion estimates outper-

form the static no motion case, but are not as good as the patient-specific 4D CTA based motion.

This work was financially supported by ITEA project 09039, Mediate, and NWO grant numbers 612.065.618 and 639.022.010.

References

1. N Baka, M de Bruijne, T van Walsum, B Kaptein, J Giphart, M Schaap, W Niessen, and B Lelieveldt. Statistical Shape Model Based Femur Kinematics from Biplane Fluoroscopy. *IEEE Transactions on Medical Imaging*, accepted, April 2012.
2. Nora Baka, Coert Metz, Michiel Schaap, Boudewijn P. F. Lelieveldt, Wiro J. Niessen, and Marleen de Bruijne. Comparison of Shape Regression Methods under Landmark Position Uncertainty. In Gabor Fichtinger, Anne Martel, and Terry Peters, editors, *Medical Image Computing and Computer-Assisted Intervention MICCAI 2011*, volume 6892 of *Lecture Notes in Computer Science*, pages 434–441, Berlin, Heidelberg, 2011. Springer Berlin Heidelberg.
3. S. Bouattour, R. Arndt, and D. Paulus. 4D Reconstruction of Coronary Arteries from Monoplane Angiograms. In André Gagalowicz and Wilfried Philips, editors, *Computer Analysis of Images and Patterns*, volume 3691 of *Lecture Notes in Computer Science*, pages 724–731–731, Berlin, Heidelberg, 2005. Springer Berlin Heidelberg.
4. Alejandro F. Frangi, Wiro J Niessen, Koen L Vincken, and Max A Viergever. Multiscale vessel enhancement filtering. In *Medical Image Computing and Computer-Assisted Interventation MICCAI98*, volume 1496, pages 130 – 137, 1998.
5. Martin Groher, Darko Zikic, and Nassir Navab. Deformable 2D-3D registration of vascular structures in a one view scenario. *IEEE Transactions on Medical Imaging*, 28(6):847–60, June 2009.
6. C.T. Metz, N. Baka, H. A. Kirisli, M. Schaap, S. Klein, L. Neefjes, N.R.A. Mollet, B.P.F. Lelieveldt, M. de Bruijne, W.J. Niessen, and T. van Walsum. Regression-based cardiac motion prediction from single-phase CTA. *IEEE Transactions on Medical Imaging*, 31(6):1311–1325, 2012.
7. C.T. Metz, M. Schaap, S. Klein, P. Rijnbeek, L. Neefjes, N.R.A. Mollet, C. Schultz, P.W. Serruys, W.J. Niessen, and T. van Walsum. Alignment of 4D Coronary CTA with Monoplane X-Ray Angiography. In *MICCAI workshop: Augmented Environments for Computer assisted interventions*, 2011.
8. Michiel Schaap, Theo van Walsum, Lisan Neefjes, Coert Metz, Ermanno Capuano, Marleen de Bruijne, and Wiro Niessen. Robust shape regression for supervised vessel segmentation and its application to coronary segmentation in CTA. *IEEE Transactions on Medical Imaging*, 30(11):1974–86, November 2011.
9. Eduard Serradell, Adriana Romero, Ruben Leta, Carlo Gatta, and Francesc Moreno-Noguer. Simultaneous correspondence and non-rigid 3D reconstruction of the coronary tree from single X-ray images. In *International Conference on Computer Vision ICCV2011*, pages 850–857, 2011.
10. Kean H Soon, Joseph B Selvanayagam, Nicholas Cox, Anne-Maree Kelly, Kevin W Bell, and Yean L Lim. Percutaneous revascularization of chronic total occlusions: review of the role of invasive and non-invasive imaging modalities. *International Journal of Cardiology*, 116(1):1–6, March 2007.

Fast AAA Thrombus Segmentation from CTA Images for Endovascular Repair Follow-up

Iván Macía[1,2,3], María Arenas[1,2], Jon Haitz Legarreta[1,2], Isabelle Robin[1,2], Manuel Graña[3], and Sabarinath Rajasekharan[1,2]

[1] Vicomtech Foundation, San Sebastián - Donostia (Spain)
http://www.vicomtech.org
[2] Biodonostia Health Research Center, San Sebastián - Donostia (Spain)
http://www.biodonostia.org
[3] Computational Intelligence Group, University of the Basque Country UPV/EHU (Spain) http://www.ehu.es/ccwintco

imacia@vicomtech.org

Abstract. Segmentation and quantification of AAAs in CTA images is a relevant task for primary diagnosis and follow-up after EVAR. This paper describes and evaluates a refined version of a fast and accurate method for the segmentation of the aneurysm thrombus based on a radial model approach. It uses a priori knowledge and spatial coherency for obtaining an initial thrombus contour which is then refined by removing spurious sectors. The method provides a fast segmentation and easy parameter setup while maintaining a high degree of accuracy, which makes it suitable for clinical routine. Thrombus segmentation results are presented in real clinical CTA images used for EVAR follow-up which demonstrate the high speed and accuracy of the method.

Keywords: Abdominal aortic aneurysm, AAA, endovascular aneurysm repair, EVAR, Computed Tomography Angiography, CTA, lumen, thrombus, segmentation, radial model

1 Introduction

Abdominal aortic aneurysms (AAAs) are focal enlargements of the aortic wall in the abdominal region of the aorta whose rupture has a high risk of mortality. Endovascular Aneurysm Repair (EVAR) is the preferred surgical procedure, which requires periodic follow-up using CTA images. It has been suggested [1] that the aneurysm volume change is the best indicator to determine positive evolution, which requires a prior segmentation of the thrombus. Segmentation of the aneurysm thrombus is mainly hindered by the presence of adjacent structures with similar intensity on the images and some irregularity in its shape. Thrombus segmentation strategies proposed in the literature include, among others, deformable models [2,3,4], level-set methods [5,6,7] or Active Shape Models (ASM) [8]. Some of these methods give reasonable good results but either they

are too complex to be setup or controlled by a non-expert or depend on the availability of a good set of training data. Moreover, they are time consuming and require some degree of user interaction, sometimes difficult to be implemented within an interface for clinical routine. Dehmeshky *et al.* [9] proposed a grayscale and geometric appearance model [9]. Similarly, we use prior knowledge on the appeareance of the aneurysm, but their method requires masking of several adjacent structures. Recently, segmentations with active contours using polar representations where proposed in [10].

We present some improvements and experimental evidence on our algorithm for AAA thrombus segmentation described in [11]. The proposed method, based on a radial model approach with appearance priors and spatial constraints, is very fast and needs little human interaction for initialization or parameter tuning. An initial thrombus segmentation is obtained starting from the detected lumen or stent boundaries. This segmentation is then corrected using geometrical constraints in order to avoid leakage in adjacent structures where no apparent aneurysm boundary is visible. Its simplicity and speed makes it suitable for clinical routine allowing easy parameter setting with visual feedback, as it is designed as a part of a complete system for EVAR follow-up.

The remainder of this paper is organized as follows. The basic method is described briefly, with some remarks from our recent experience, in Section 2; Section 3 describes some initialization issues. Section 4 describes the general procedure for thrombus contour correction; Section 5 provides experimental results with a discussion in Section 6. Finally, Section 7 presents our conclusions.

2 AAA Segmentation

The complete AAA segmentation method consists of the following stages:

1. *Lumen Segmentation*: an initial lumen segmentation is obtained using a region growing algorithm based on confidence measures from a pair or more seed points as implemented in [12].
2. *Lumen Centerline Extraction*: performed slice by slice using 2D image moments on the connected components (CCs). CCs not corresponding to the lumen are discarded by calculating centroid distances to adjacent slices.
3. *Polar Reformatting*: a slice-based polar reformatting is generated, in order to obtain a linear representation of the radial model which is faster to process. Strictly, this does not constitute a reformatting on cylindrical coordinates but, rather, a generalized cylinder. This allows to adapt to the shape of the centerline, taking into account its curvature. The presence of a dominant vertical direction makes the method still valid.
4. *Initial Thrombus Segmentation*: based on the analysis of connected components (CCs) described both radially and at slice level using run-length encoding. The result is a set of radial contours describing the thrombus outer boundary starting from the inner boundary. It requires a pre-processing step consisting of median filtering, in order to remove noise, and a raw thresholding which removes the hyperintense structure corresponding to the stent

and other spurious structures. Note that, differently from other methods, we do not remove any structure outside the thrombus region. The result is a good approximation of the external thrombus contour, with the exception of some areas where the thrombus region invades adjacent structures.

5. *Thrombus Contour Correction*: based on the analysis of discontinuities in the initial contours and statistical information, outlier sectors in radial contours are identified and replaced by interpolation between valid contour segments.
6. *3D Reconstruction and Smoothing*: introduces some regularization in the axial direction by removing remaining spurious edges.
7. *Volume Quantification*: corresponds to the region from the external part of the stent to the segmented outer thrombus boundary.

We refer the reader to our article on [11] for details on the first four stages. In the next sections, we will focus on the initialization and correction stages which were improved in order to obtain more accuracy and robustness.

3 Initialization Issues

The segmentation of the thrombus may start from a prior lumen segmentation or by automatic detection of the lumen boundaries, as in the experiments performed in this paper. In routine EVAR follow-up CTA images two problems arise during initialization severely affecting the thrombus segmentation: the presence of the stent and the iliac arteries bifurcation.

In our method, we do not deal with the problem of an accurate stent segmentation. However, the segmentation based on CC analysis is less problematic if we first detect the stent and consider the region outside its boundaries. We simply detect the stent as CCs of high intensity in the close vecinity of the lumen. After removal, it is assumed that the thrombus region corresponds to the adjacent area extending radially.

One major problem found during our initial experiments, was the presence of double iliac arteries in the thrombus region as can be seen in Figures 2a and 2c. Most of the methods assume that the thrombus is only present in the aortic area, where there is a single lumen branch. However, the bulge may be present in the area where the iliac arteries start, even when the aneurysm itself was not present in this area before the intervention. In this case, the stent forces the two branches of the iliac arteries to be close to each other and there exist two centerline branches. One solution consists of first segmenting the lumens of both iliac arteries and then extend this segmentation in order to create a convex contour by filling the concave areas between both branches at each slice. This allows us to apply the rest of the segmentation algorithm for the thrombus without further modification. The convex contour may be obtained easily using open and close morphological operations. In practice, complete convexity is not always needed for the algorithm to work (see Figure 2c where the mask is overlaid).

4 Thrombus Contour Correction

Thrombus contour correction has been improved from the implementation in [11], by introducing a bias correction in the thrombus center position, which improves results when the lumen is not centered with respect to the thrombus, and two parameters that control the correction of spurious radial sectors.

The external thrombus contour correction is based on a continuity constraint imposed over the external contour T_{ext}.We assume that the thrombus is radially smooth, allowing for small discontinuities which are first identified as significant radial changes from point to point by using a discontinuity parameter δ.

In the initial radial function, there exist some bias due to the offset of the centerline with respect to the geometric center of the thrombus, which is unknown. In order to partially remove this bias, we first recompute the centroid of the initial contour and update the angles, which yields a new radial function T'_{rext} for the external contour in which discontinuities are easier to identify.

After the identification of discontinuities, the contour is divided in radial sectors $S_i(\theta_i, \theta_{i+1})$ defined as

$$\begin{gathered} S_i(\theta_i, \theta_{i+1}) = \{T'_{rext}(\theta) : \theta \in [\theta_i, \theta_{i+1})\} : \\ |T'_{rext}(\theta_i) - T'_{rext}(\theta_{i-1})| > \delta, \quad |T'_{rext}(\theta_{i+1}) - T'_{rext}(\theta_i)| > \delta \end{gathered} \tag{1}$$

Next we identify the spurious radial sectors. We calculate their average values comparing them with the standard deviation from the median of all radial values. That is, we mark a sector S_i as spurious if:

$$\mu(S_i) > \kappa \sigma_{median}(T'_{rext}) \tag{2}$$

where κ is a scaling factor and $\sigma_{median}(T'_{rext})$ is the standard deviation of the median of radius values. Using the median instead of the mean, prevents outlier values from influencing the calculations. Confirmed contiguous radial sectors are joined to obtain new sectors. Finally, discarded radial sector values are replaced by linearly interpolating the radius between the boundary values of adjacent valid sectors. The procedure is depicted in Figure 1. Note how the correction removes the spurious sectors and how some small discontinuities are preserved, that appear naturally in the thrombus due to the presence of adjacent structures. If necessary, this can be adjusted with the discontinuity parameter δ.

5 Experiments and Results

Our method has been initially tested on 5 CTA datasets from real patients under follow-up after EVAR, obtained from a LightSpeed16 CT scanner (GE Medical Systems, Fairfield, CT, USA) with an average 0.725x0.725x0.8 mm. spatial resolution. Average computation times for thrombus segmentations obtained on an Intel Core 2 Quad CPU at 2.4 Ghz are shown in Table 1. We obtained an average computation time of 0.045 s. per slice demonstrating the high speed of the method. From this total time, on average, 15% was spent calculating the polar reformatting, 47% in the median filtering and 38% in the contour estimation.

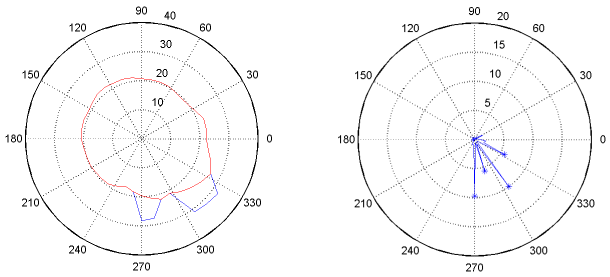

(a) (b)

Fig. 1: Contour correction procedure. (a) Initial (blue) and corrected (red) contours of two slices in a polar plot. (b) Corresponding derivative of initial contour and identified discontinuities.

Manual segmentations were carefully delineated by a single expert for comparison. A volume of interest was defined to reduce memory requirements and two seed points inside the lumen were selected for the segmentation of the lumen. The polar representation of the image was obtained in an area of 10 mm around the centerline. The described radial approach was used to segment the thrombus contours and finally a mask was obtained by rasterization of the contour. In all our experiments, we used 40 angular and 250 radial samples respectively (0.4 mm. radial resolution) for the polar reformatting.

The parameters for the initial thrombus segmentation *were not changed* in our experiments. For the correction step we used values of δ in the range 1.5-3.5. The scaling factor κ was fixed to 1.5 except in one dataset which was 2.5. This allowed us to verify that the parameter sensitivity is low, which is good for routine applications. The results were accurate except in some slices with spurious structures that showed no visible boundaries with respect to the thrombus.

Average overlapping ratios of automated A and manual B segmentations are shown in Table 2. The first dataset is a typical case of a thrombus segmentation that our method solves with high accuracy (overlapping ratios of 93.52% and 86.76%). The four other datasets are from the follow-up of a single patient and can be considered a difficult scenario. The thrombus has a region with double lumen in the iliac arteries and the lumen is very eccentrical. Yet good values are obtained. We also present some filtered values where we removed the slices were the contour was leaking in a few contour points in order to test the accuracy in the remaining slices. This can be done either by changing the parameter values for those slices or by manual correction of the contour. Finally, we present a 3D reconstruction of the contours, depicted in Figure 3. We do not provide comparison of volumetric quantifications, since the external stent contour was not available on the manual segmentations. In any case, the focus of this paper is on the external contour, which is the most complicated task.

Dataset	Slices	Time(s.)
1	19	0.87±0.02
2	19	0.87±0.02
3	22	1.02±0.02
4	21	1.01±0.04
5	207	7.68±0.08

Table 1: Computation times for thrombus segmentations in 5 datasets calculated as averages of 10 executions.

Dataset	(a)	(b)	(c)	(d)
1	93.5±2.5	86.8±5.2	-	-
2	89.9±7.3	83.6±7.1	95.4±2.7	89.8±3.4
3	94.0±8.9	83.9±10.5	96.1±2.3	89.1±3.5
4	89.9±9.3	81.9±10.3	95.0±2.4	88.8±3.0
5	92.1±6.7	79.7±9.6	94.0±5.7	86.7±4.3

Table 2: Overlapping areas in % between proposed method segmentations and ground-truth manual segmentations. (a) = B/A$\bigcup$B, (b) = A$\bigcap$B/A$\bigcup$B. (c)=(a) and (d)=(b) both after removing incorrect contours. Table shows average values for all slices in each datasets.

6 Discussion

One of the main advantages of the described method is its efficiency, as it can process a large number of slices in a few seconds with high accuracy (Figure 2). The parameter setting is minimal and most of our experiments have used the same set of parameters. The value of δ could be changed in order to allow for some tolerance in discontinuities. Increasing the value of κ allows more deviation from the median radius value, in cases where the thrombus is very eccentrical with respect to the centerline.

The method provides accurate results where other methods would fail due to absence of visible thrombus boundaries (Figure 2). It also allows for some discontinuities that improve the accuracy with respect to some methods based on smooth curves or deformable models which involve complex calculations.

We emphasize that the method is oriented for the segmentation of AAAs by non image processing experts. The use of a radial approach, makes it very easy to develop a user interface for fast segmentation of CTAs. Parameter setting is relatively simple and the speed of the method allows for quick visual feedback. In case of failure, δ and κ could be adjusted for single slices (however, note that, in our experiments, we used fixed values of δ and κ for all slices of each dataset). If the problems persist, the user simply would have to invalidate possible incorrect regions of the contour and mark only a few radial points at each erroneous section, either manually or by providing the radius value. This has been a major

consideration in the design of the method, since we expect it to be part of a software for follow-up of EVAR interventions.

The method works on a slice-by-slice basis in order to take into account the symmetry with respect to the centerline and to reduce the possibility of large leaks at volumetric level, where some coherence is introduced by the 3D polygonal smoothing. The polar representation is also advantageous, since it presents the data in the form of a generalized cylinder VOI around the centerline, which implicitly takes into account the radial symmetry, and allows fast calculations based on CCs and run-length encoding.

7 Conclusions

We have developed a method for fast segmentation of AAAs after EVAR interventions. First, the lumen of the aorta is segmented and a centerline is obtained. The thrombus segmentation uses a radial model and is obtained by analysis of connected components subject to spatial constraints and prior knowledge. The thrombus correction stage is based on dividing the initial external contours obtained from the thrombus in radial sectors according to discontinuities found along the contour. Then the incorrect sectors are discarded according to statistical measurements and the gaps interpolated according to adjacent sectors. We show initial experimental evidentce on five real CTA datasets. We also consider the case where the iliac artery bifurcation is inside the thrombus region. The method is very fast while maintaining a high degree of accuracy, requires minimal parameter setting, since most of the possible parameters remain fixed and thus is suitable for clinical routine. Future work will be oriented to further improve the robustness of the method, regularize resulting contours on a final stage and perform a more exhaustive clinical validation.

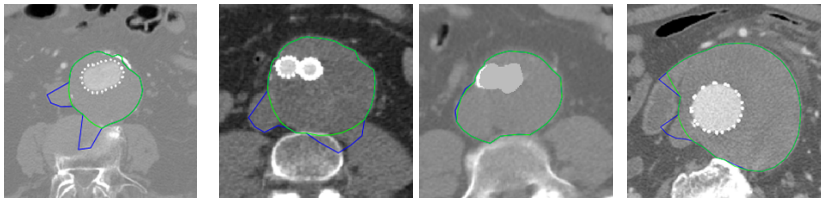

(a) (b) (c) (d)

Fig. 2: Segmented slices by our approach showing the initial (blue) and the corrected (green) contours. Figure (d) shows some problems found.

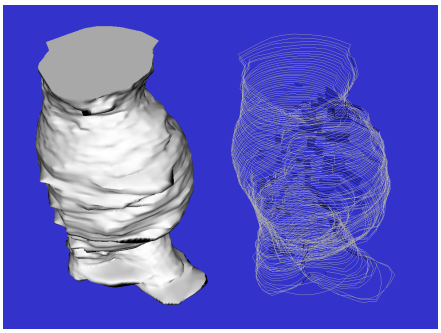

Fig. 3: 3D polygonal reconstruction (left) and 3D contours (right) for dataset 1.

References

1. Wever, J., Blankensteijn, J., Mali, W., Eikelboom, B.: Maximal aneurysm diameter follow-up is inadequate after endovascular abdominal aortic aneurysm repair. European J. of Vasc. and Endovasc. Surg. **20** (2 2000) 177–182
2. Subasic, M., Loncaric, S., Sorantin, E.: 3d image analysis of abdominal aortic aneurysm. In: Proc. SPIE Med. Imag. Proc. Volume 4684. (2002) 1681–9
3. Olabarriaga, S., Rouet, J., Fradkin, M., Breeuwer, M., Niessen, W.: Segmentation of thrombus in abdominal aortic aneurysms from cta with nonparametric statistical grey level appearance modelling. IEEE Trans. Med. Imag. **24** (4 2005) 477– 485
4. Demirci, S., Lejeune, G., Navab, N.: Hybrid deformable model for aneurysm segmentation. In: IEEE Int. Symp. on Biomedical Imaging: From Nano to Macro, Boston, Massachusetts, USA (June/July 2009)
5. Zohios, C., Kossioris, G., Papaharilaoub, Y.: Geometrical methods for level set based abdominal aortic aneurysm thrombus and outer wall 2d image segmentation. Computer Methods and Programs in Biomedicine **107**(2) (2012) 202–217
6. Zhuge, F., Rubin, G., Sun, S., Napel, S.: An abdominal aortic aneurysm segmentation method: level set with region and statistical information. Med. Phys. **33** (5 2006) 1440–53
7. Das, B., Mallya, Y., Srikanth, S., Malladi, R.: Aortic thrombus segmentation using narrow band active contour model. In: Proc. IEEE Eng. Med. Biol. Soc. Volume 1. (2006) 408–11
8. de Bruijne, M., van Ginneken, B., Viergever, M., Niessen, W.: Interactive segmentation of abdominal aortic aneurysms in cta images. Med.Im.An **8** (2004) 127–38
9. Dehmeshki, J., Amin, H., Ebadian-Dehkordi, M., Jouannic, A., Qanadli, S.: Automatic detection, segmentation and quantification of abdominal aortic aneurysm using computed tomography angiography. In: Proc. Med. Image Understanding and Analysis. (2009)
10. Baust, M., Yezzi, A., Unal, G., Navab, N.: A sobolev-type metric for polar active contours. In: Proc. Comp. Vis. Pattern Recognition (CVPR). (2011) 1017–24
11. Macía, I., Graña, M., Maiora, J., Paloc, C., de Blas, M.: Detection of type ii endoleaks in abdominal aortic aneurysms after endovascular repair. Computers in Medicine and Biology **41**(10) (Oct 2011) 871–89
12. Ibanez, L., Schroeder, W., Ng, L., Cates, J.: The ITK Software Guide 2nd Ed. Kitware, Inc. ISBN 1-930934-15-7. (2005)

Rapid Prototyping of Silicone-based Phantom Models for Stent Simulation Validation

Christoph Russ[1], Michael Gessat[1 2], Volkmar Falk[2], and Gabor Székely[1]

[1] Computer Vision Laboratory, ETH Zürich,
Sternwartstr. 7, 8092 Zürich, Switzerland
{russc,mgessat,szekely}@ethz.ch
http://www.vision.ee.ethz.ch
[2] Division of Cardiac and Vascular Surgery, University Hospital Zürich,
Rämistr. 100, 8093 Zürich, Switzerland
http://www.herzgefaesschirurgie.usz.ch

Abstract. Robust and reliable development of stent designs and materials is an important aspect for medical device manufacturing in relation to procedures such as Transcatheter Aortic-Valve Implantation. It is essential to perform a variety of experiments at an early stage of this process to define suitable material requirements and stent geometry. Mechanical simulation of realistic use case scenarios is a cost and time effective approach to optimize this task. In silico experiments can assist the device development phase and successively support patient-specific procedure planning. To establish confidence in the predictive power of in silico models and the corresponding simulation results, we therefore present a validation framework for stenting simulations. Our workflow allows the comparison of finite element analysis with actual mechanical response tests using optical tracking of stent deformation in artificial vessel phantom models. The results indicate that stent and vessel deformation can be analysed and validated across well-defined tissue properties within the presented framework.

Keywords: vessel, aorta, phantom, stent, simulation, validation, rapid prototype, finite element analysis

1 Introduction

1.1 Background and Previous Work

Stent placement is a minimal-invasive medical procedure to treat pathologies within the vascular system. It is commonly used to increase the diameter of blood vessels at narrow sections, treat artery enlargement and weakening due to aneurysms or replace dysfunctional heart valves, which show abnormal blood flow behaviour. Devices used in these procedures can be divided into two groups: self-expanding and balloon-expanding stents. Medical device manufacturers release a growing number of stent designs in variable sizes [1]. Creating an accurate simulation environment for their experimental validation can reduce development time and help to optimize design aspects. It can furthermore guide the choice of a specific stent type and size for an individual patient.

Mechanical validation of stents is commonly achieved through tensile loading experiments. Force measurement of crush tests between parallel plates as shown in [2] allows global material deformation modelling, but fails to provide testing scenarios similar to the stent's actual use cases. Finite element anaylsis (FEA) of stent deformation has been performed at a large variety of applications [3],[4],[5], but is commonly not validated against real world experiments. Image-based experiment tracking of vessel phantoms to analyse contact areas was shown in [6], however, local stent deformation measurements have not been performed. Other studies [7],[8] use phantom models for stent validation, but do not relate the results to simulated experiments.

1.2 Motivation

The central goal of this work is to outline a systematic approach to procedural validation of in silico experiments in relation to stent simulation within vascular structures. Initially, phantom modelling of common vascular structures in human anatomy allows experimenting with related medical procedures in a controlled environment. The ascending aorta and aortic root are of great interest for analysis of advanced stent design, where the focus is set on the replacement of heart valves. In this scenario the positioning and stent deformation after implantation are of critical importance to guarantee functional artificial valves and reduce potential leakage as well as conduction abnormalities. Predictive simulation based on numerical models of the mechanical behaviour could be an important aid in procedure planning. However, validation of these commonly simplified, abstract virtual models is required to establish confidence in the predicted results. Therefore, a flexible and robust validation framework for experimental validation of simulated stenting is required.

As mechanical vessel properties are patient-dependent, a rapid prototyping approach to generate artificial vessels can supply a variety of test cases for validation of simulated stenting procedures. A modular framework design allows to increase complexity of individual components iteratively. Simplified models support the controlled design of a predictable and robust experimental environment, which is required initially to validate proposed experiments before increasing material or model complexity.

2 Methods

2.1 Phantom Material Specification

For rapid prototyping of vessel-like phantom structures with mechanical properties in the range of soft tissue, a suitable material with adjustable elasticity parameters is required. The material needs to match mechanical properties of a common aortic vessel and enable the stable, homogeneous design of an arbitrary, hollow, cylindrical shape. The construction process has to offer repeatability and flexibility for versatile phantom model design to generate a suitable subset of vessel phantoms at different configurations. For further validation and experimental

analysis, the model is preferred to be transparent to expose the behaviour of an inserted object, such as a stent.

Silicone rubber compounds are used in medical phantom models to represent soft tissue due to comparable mechanical properties. Dependent on the type of silicone, it is commonly available as a translucent material, which can be modelled in an arbitrary form with variable mechanical properties. Figure 1 shows tensile strength of multiple silicone compounds available for rapid prototyping to generate phantom models of vascular structures, such as the aorta. Using a variety of material strengths with different elasticity and hardness values allows for adoption of the validation model to specific test cases (e.g. involving validation against pathologic tissue changes). Silicone-based phantoms commonly feature a high tear resistance and low shrinkage over time. They retain their shape after multiple iterations of applying high load and can be stored without significant material decomposition or hardening over a long period of time.

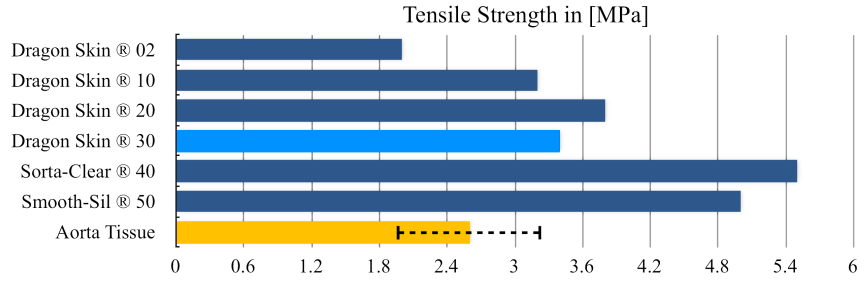

Fig. 1. Mechanical properties for silicone-based materials sold by Smooth-On, Inc. and their comparison to aortic vessel tissue.

2.2 Silicone Vessel Phantom Design Process

A vessel phantom is constructed by applying multiple layers of liquid silicone rubber onto a three dimensional structure representing the lumen of the vessel. Particular care is required to achieve an appropriate thickness of the material. By using a representation of the inner lumen, any artificial or patient-specific vessel structure can be reconstructed with this procedure in a chosen vessel thickness with variable mechanical properties. Figure 2 shows initial prototypes of vessel phantoms and corresponding material samples, which were used to determine mechanical properties of each silicone compound.

2.3 Image-based Stent Deformation Measurement

One solution to validate the deformation results of the described setup, is to use micro-CT imaging for accurate 3D reconstruction of the stent. However, the large density differences between metal and artificial vessel wall lead to metal

Fig. 2. Vessel phantom prototypes developed for experimental validation of stent deformation. Material samples for each silicone-compound have been tested repeatedly under uni-axial tensile loading.

streak artefacts in the images. As this framework aims for a rapid prototype development environment, we propose the use of a calibrated, high-resolution, dual-camera setup positioned with a 90 degree offset around the experiment to enable measurement of local stent and vessel deformation through optical tracking. We are using the "Caltech Camera Calibration Toolbox"[3] following a calibration approach presented in [9]. Using a camera-based setup, will allow the use of additional, larger mechanical equipment for load testing, which can not fit into a micro-CT. It does not require complex tracking equipment and simplifies the experimental design significantly.

By using translucent materials, the stent remains visible inside the vessel phantom. Marking the surface and stent points of interest allows their identification within corresponding images. If required, time dependent experimental analysis is possible in this setup, when using continuous image capturing. A strong limitation of this approach is the required accurate calibration, which constrains the resulting error. Figure 3 shows a standard calibration setup as used for deformation experiments and highlights two corresponding image points for reconstruction and tracking.

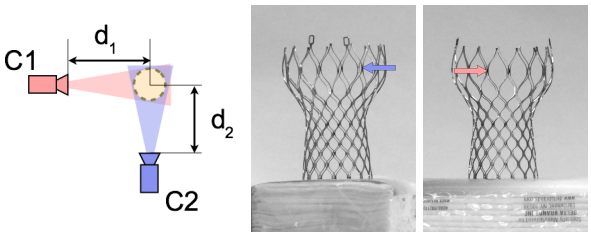

Fig. 3. Dual-camera setup for image-based local deformation measurement of stents. The arrows identify a matching image point seen from camera C1 and C2.

[3] `http://www.vision.caltech.edu/bouguetj/calib_doc/index.html`

3 Experiments

In this framework, preliminary experiments are required to ensure that the mechanical material model of the used silicone compounds has been characterized sufficiently as further deformation experiments will rely on these models.

3.1 Material Characterization

The silicone-based materials listed in Figure 1 have been analysed with robust uni-axial tensile loading tests to evaluate their elastic behaviour. Due to the homogeneous properties of silicone rubber, anisotropic effects are negligible. Within the maximal estimated strains, enforced in stent expansion experiments on the silicone phantom vessel structure, the mechanical response can furthermore be estimated with a linear elastic material model. However, as surface contact modelling will be essential, non-linearities have to be taken into account within the finite element simulation. The stent's material characterization is taken from literature [10] as well as using experimentally verified model parameters, acquired with a similar procedure as the load tests performed on silicone samples.

3.2 Stent Placement

For experimental validation, the stent is placed inside the vessel phantom as shown in Figure 4. At maximum level of expansion images are then being acquired to record the deformation. In the presented example, two different phantom vessels (V1 and V2) with different material thickness have been stented with a Medtronic CoreValve®. The self-expanding stent was inserted at the top end of the silicone tube, while the corresponding lower end of the phantom has been constrained in movement. In the final constellation the thinner vessel (V1) shows elastic deformation of 129.5% at its maximum diameter, while the thicker model (V2) deforms no more than 112.9 %, compared to the initial geometry configuration.

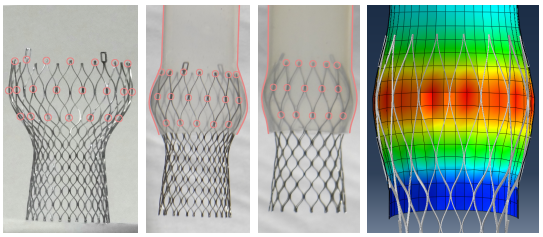

Fig. 4. 3D stent model reconstruction. Landmarks on the device are highlighted and used to generate a virtual stent representation. Point-based distance measurement between these markers define the amount of local deformation. FEA is used for stent simulation and allows the visualization of local deformation magnitudes for stent and vessel.

3.3 Simulated Stenting

Virtual experiments, assembled in correspondence to the validation setup, are performed using finite element solvers. An example FEA of the CoreValve® is presented in Figure 4. The outcome of these simulated experiments can then be compared with the previously measured deformation results to validate the material models and virtual simulation setup.

The simulation environment uses the Simulia® Abaqus Implicit and Explicit solvers. Finite element models of the vessel phantom as well as the virtual stent model are generated procedurally and by using common CAD applications.

4 Results

It is an essential aim of this validation framework to provide a controllable environment for experimental verification of simulated stent experiments. The vascular phantom is modelled using homogeneous silicone compounds to allow a high degree of control over the expected material behaviour and its experimental setup. A general validation method of virtual experiments has been described, which can later be used with more realistic and less predictable materials to provide a common platform for a variety of stenting experiments under predefined constraints.

4.1 Phantom Vessels

The generated silicone-based phantom vessels offer comparable mechanical properties in the same order of magnitude as common human vessels, such as the aorta. Strong non-linear and anisotropic characteristics as found in live tissue are not present. The homogeneous characteristics of silicone rubber can not imitate the complex muscular cell structure of vessels. It can, however, be constructed from multiple layers, which allow the combination of soft and hard silicone compounds to represent anatomical cell layers such as elastic membrane, muscle fibre and connective tissue as a step towards a more realistic soft-tissue model. Currently, the simplified material reduces uncertainties within the experiments and allows to focus the initial validation effort on stent behaviour. For advanced testing scenarios it remains to be determined if a more accurate material is required, which allows to model observed stress and strain values with higher realism.

The vessel phantom material used for Figure 4 is based on the DragonSkin® (Shore A: 30) compound. A corresponding finite element experiment with a linear elastic material model for both the CoreValve® stent and the silicone vessel, has found comparable deformation values with maximum vessel deformation of 125% (V1) and 110% (V2) compared to their original diameter.

4.2 Validation Framework

The complete, modular framework for validating stent simulation results is described in Figure 5. As seen within the presented diagram, real world experiments

and finite element simulation setup are aligned. The required virtual input model of a vessel lumen can be generated manually from generic CAD models or derived from segmentations of patient-specific imaging datasets. The actual vessel lumen can then be manufactured using a 3D printer. The volumetric model of the stent can be constructed in common CAD applications or acquired through imaging technologies. After performing the desired experiments in silico and within the vessel phantom, the deformation results can be compared directly.

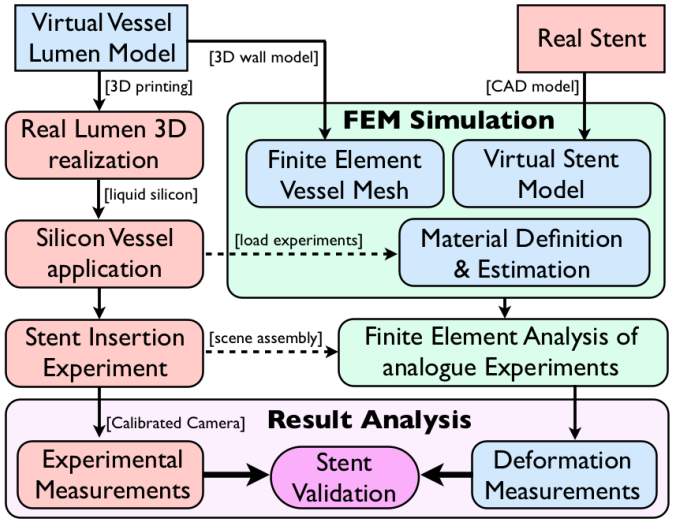

Fig. 5. Completed framework for experimental validation of stents within a rapid prototyping workflow for vessel phantom construction.

5 Conclusion

We have described a framework for rapid prototyping of silicone-based vessel phantoms and presented a workflow to validate a simulation environment for stenting procedures, which can be related to device design as well as patient-specific procedure planning. Our approach allows the consistent validation and initial testing of medical stenting simulations in a controlled and predictable environment. It is designed to offer flexibility towards geometric vessel structures and mechanical properties to support variability in the experimental setup and offer a potential for integrating pathologies into the phantom. Silicone models are suitable to establish a basic validation pipeline and allow the generation of an experimental test environment for a variety of simulation approaches. Due to their lack of material complexity, highly realistic results are not expected. For this purpose, mechanically more realistic materials for vessel simulation have been developed by companies, such as SynDaver™ Labs. However, silicone phantoms were used in this study with the target to establish an overall framework which can be used for the validation of more complex stenting models in the future.

Once the predictive performance of a specific model has been verified, it can be used as an in silico experimental environment for the systematic exploration of the effects of varying stent design parameters and therefore efficiently optimize new devices. At the same time it offers a rapid prototyping environment for fast-tracked testing and validation of stents. The presented workflow is furthermore suitable for the generation of patient-specific vascular geometries by extracting a model of the inner lumen from image based vessel segmentation as shown in [11]. This offers a powerful pre-operative surgical planning tool, when combined with the exploration of the dependency of the interventional outcome on inevitable uncertainties of relevant material parameters and boundary conditions.

Acknowledgements. This work was supported by the Swiss National Science Foundation (SNSF grant no. CR32I3_135044) and the Swiss Heart Foundation.

References

1. Webb, J. G., Binder, R. K.: Transcatheter aortic valve implantation: The evolution of prostheses, delivery systems and approaches. Archives of Cardiovascular Diseases. 105(3),153–159 (2012).
2. Labossiere, P., Perry, K.: Predicting Performance and Reliability of Nitinol Medical Implants. In: SEM Annual Conf. & Exp. on Expl. and Appl. Mech. (2007).
3. Kim, S. M., Park, S. Y. Finite Element Analysis of Stent Expansion Considering Stent, Artery and Plaque Interaction. In: Proc. of the 24th IASTED Intern. Conf. on Biomed. Eng. 143-146 (2006).
4. Egger, J., Großkopf, S., Freisleben. B.: Virtual Stenting for Carotid Stenosis with Elastic Artery Wall Modeling. In: 4th European Conf. of the Intern. Federation for Med. and Bio. Eng. (IFMBE). 22(22), 2499–2502 (2009).
5. Wu, W., Qi, M., Liu, X., Yang, D., Wang, W.: Delivery and release of nitinol stent in carotid artery and their interactions: a finite element analysis. J. Biomech. 40(13), 3034–40 (2007).
6. Takashima, K., Kitou, T., Mori, K., Ikeuchi, K.: Simulation and experimental observation of contact conditions between stents and artery models. Medical Engineering & Physics. 29(3),326–335 (2007).
7. Poerner, T. C., Ludwig, B., Duda, S. H., Diesing, P., Kalmár, G., Süselbeck, T., Kaden, J. J., Borggrefe, M., Haase, K. K.: Determinants of Stent Expansion in Curved Stenotic Lesions: An In Vitro Experimental Study. Journal of Vascular and Interventional Radiology. 15(7),727–735 (2004).
8. Kalejs, M., von Segesser, L. K.: Rapid prototyping of compliant human aortic roots for assessment of valved stents. In: Interactive Cardiovascular and Thoracic Surgery. 8(2),182–186 (2009).
9. Zhang, Z.: Flexible camera calibration by viewing a plane from unknown orientations. In: The Proceedings of the Seventh IEEE International Conference on Computer Vision. 666-673 (1999).
10. Petrini, L., Migliavacca, F.: Biomedical Applications of Shape Memory Alloys. Journal of Metallurgy. (2011).
11. De Santis, G., De Beule, M., Segers, P., Verdock, P., Verhegghe, B.: Patient-specic computational haemodynamics: generation of structured and conformal hexahedral meshes from triangulated surfaces of vascular bifurcations. Comput. Methods Biomech. Biomed. Eng. 14(9),797–802 (2011).

Multi-image Based Stent Visibility Enhancement

Yunqiang Chen, Ying Zhu, Ti-chiun Chang, and Tong Fang

Siemens Corporate Research,
755 College Rd East
Princeton, NJ 08536, USA
{yunqiang.chen,yingzhu,ti-chiun.chang,tong.fang}@siemens.com

Abstract. This paper presents a multi-image based algorithm to improve the stent visibility in dynamic fluoroscopic imaging. By explicitly modeling and separating the stent and background clutter (e.g., bones and organs), the algorithm can effectively improve the stent visibility and the non-rigid stent registration accuracy for the assessment of coronary stenting. Experimental results have demonstrated its effectiveness.

Keywords: image enhancement, layer separation, image sequence, stent visibility

1 Introduction

Coronary stenting based on real-time X-ray fluoroscopic imaging is a common interventional procedure. The signal to noise ratio is usually very low due to the low-dosage imaging condition during the procedure. To enhance stent visibility, various image processing techniques have been developed to integrate a temporal sequence of non-contrast stent images to produce a single enhanced stent image. In previous literature, it is usually handled in two steps. First, due to the constant movement of coronary arteries, motion correction is applied to align the stent structure between temporal images. Then, an improved stent image can be obtained based on the aligned images (usually, by simply averaging all the aligned images).

1.1 Related work

Most work has been focused on how to obtain good alignment of the stent structure based on the input sequences directly. Since the input images are usually generated with low dosage X-ray, the stent structure can be hardly detected. Most algorithms rely on the more visible structures to estimate stent motion. For example, in [3], balloon markers are detected and used to align the sequences to compensate for rigid stent motion. Due to cardiac motion and vessel geometry, stents can undergo deformable motion as well. To handle deformable motion, elastic registration is proposed in [2] to utilize both balloon markers and the guide wire, which usually have better visibility than stents.

1.2 Our method

Instead of addressing the stent visibility enhancement in two separated steps, we propose to handle the two steps jointly. It is apparent that better stent alignment can result in better final stent enhancement. However, reliable and accurate stent motion estimation can be quite challenging in X-ray imaging because the images are usually cluttered with human organs and bones which usually have different motion than the stents. They are all projected into the 2D imaging sensor to form the fluoroscopy sequence and can severely distract the stent motion estimation.

In our proposed method, we explicitly model both the stent image and the background clutter so that we can effectively remove the clutter layer from the sequence. The advantages of this method are two-fold. First, by removing the clutter layer, it can improve the accuracy and robustness of the image registration algorithms that rely on image patch similarity (e.g., [1]). Second, clutter cannot be effectively removed by just averaging over all the aligned images. Explicit separating it from the stent image can enhance the stent visibility dramatically.

2 Method

In previous literature, the images are modeled as additive signal. For X-Ray images, this can be satisfied by applying a log function to image intensity. Traditionally, the log compressed images are usually formulated as follows:

$$I_i = T_i(I_S) + N_i \quad i \in [1, K] \tag{1}$$

Where I_i is one of the observed images, I_S is the stent image we want to recover, T_i represents the motion of the stent image and N_i is noise. In our scenario, N_i includes anything that does not belong to the stent image, which might include the clutter (e.g., human organs or tissue) as well as imaging noise. Since the stent is moving during the acquisition, the observed image is a mixture of the deformed stent image (i.e., $T_i(I_S)$) and noise N_i. If we assume that the noise N_i is zero-mean and independent between observed images, we can recover the stent image by align-and-average method as in most other literature (e.g., [3]):

$$\hat{I}_S = \frac{1}{K} \sum_{i \in [1,K]} T_i^{-1}(I_i) \tag{2}$$

However, the clutter consists of patient organs and is usually not independent between images. The organs are deforming and overlaid onto the whole series of images and cannot be effectively reduced by simple averaging. A more realistic model hence should be formulated as follows:

$$I_i = T_i^S(I_S) + T_i^C(I_C) + N_i \quad i \in [1, K] \tag{3}$$

Where I_C is the clutter layer, $T_i^C()$ is the motion of the clutter layer and N_i is independent zero-mean imaging noise on the ith image.

This new model requires a different way to solve than the normal align-and-average. Traditional averaging can only provide a result that is a mixture of the true stent image and a blurred clutter layer. The quality of the averaging result highly depends on if the clutter layer satisfies the independent, zero-mean assumptions.

By explicitly modeling the clutter layer, we can handle the non-independent clutter layer and obtain much more accurate stent image. The solution to this model is further explained in the following sections.

2.1 Algorithm overview

Here is a summary of how to achieve the stent visibility enhancement, including the input/output and the processing steps. The processing steps are listed as follows:

1. Ballon marker detection: detect the location of the balloon marker pair;
2. Stent motion estimation: estimate stent motion based on detected balloon markers;
3. Stent motion estimation: estimate stent motion based on detected balloon markers;
4. Layer separation: based on the multiple images, decompose the image into stent layer and clutter layer;
5. Align stent/vessel images: align stent and vessel images for better inspection of stent placement;

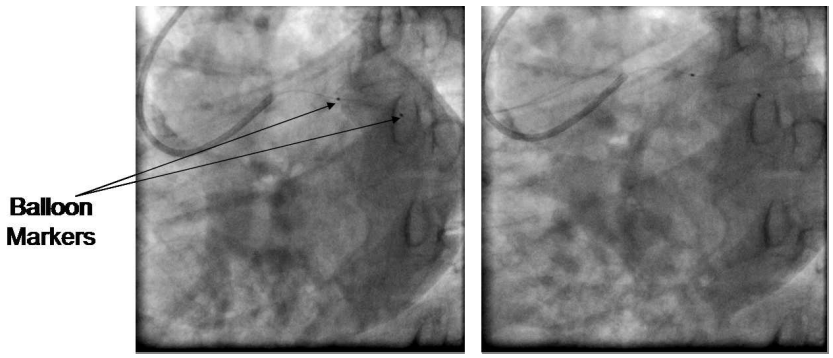

Fig. 1. Two frames of the input sequence is shown in the figure. The ballon markers can be used to estimate the rigid motion of the stent.

2.2 Balloon Marker Detection

Balloon markers can be generally characterized as small circular dot like shape. The major difficulty in marker detection is the interference from anatomical and

artificial structures, the low SNR nature in X-ray fluoroscopy, and the masking effect of the injected contrast agent. The application of template matching, which is a common first step for most detection algorithm [7], would results in quite a lot false detection.

In this work, we first design multiple directional filters based on Laplacian of Gaussian function to generate initial features (i.e., filter outputs), which indicate the strength of marker profile responses in different directions. These features provide evidences to confine with the circular marker characteristics. Together with the prior knowledge of maker pair appearance and the contextual information from neighboring frames in the image sequence, a confidence map for each frame can be calculated. Finally, for each candidate marker pair, the score is computed based on their distance, location relative to the previous detected marker pair, size, contrast, and confidence. The pair with the best score and passes a predetermined score threshold is claimed to be our target markers. We note that some of these features for marker couple detection is discussed in [8].

2.3 Stent Motion Estimation

For the frames that the balloon markers can be detected, we can estimate the motion of the stent (i.e., $T_i^S()$). Since we have the location of a pair of markers in 2D space, we can estimate the motion up to 4th degree of freedom (DOF), including 2D translation (2 DOF), rotation (1 DOF) and scaling (1 DOF). It is worth noting that the scaling should not be the traditional isotropic scaling. Instead, it should be a scaling along the long axis of the stent. The motion model we use can be calculated as follows:

- 2D Translation: translation can be calculated from the displacement between the center of the detected marker pairs on reference frame and current frame.
- Rotation: rotation angle can be calculated from the angle difference between the detected marker pairs.
- Axial Scaling: Because stent is actually moving in 3D space, there are several factors that can result in the change of the distance between the markers (e.g., zooming, out-of-plane rotation, and significant change of depth). We assume out-of-plane rotation is the major reason that causes the marker distance to change on 2D images. Base on this assumption, the scaling should only be applied along the length of the stent while the diameter of the stent should not change.

In addition to translation, rotation and scaling, an image based elastic registration method is applied to estimate the deformable motion of the stent [1]. The method uses local image information in the stent area to determine a 2D deformation field that characterizes how the stent deforms over time. The free-form deformation is represented by tensor product cubic B-spline [5, 6]. A series of stent images are then aligned non-rigidly according to the recovered deformation field. Different from the previous work [2] which relies on the in-stent guide wire to perform stent registration, this method utilizes weak image structures

from the stent profile to resolve the ambiguity of stent deformation along the guide wire.

2.4 Pre-processing

The pre-processing step consists of two parts. First, a remapping curve is applied to input image intensity to make the image more additive. Second, a lighting compensation procedure is done to compensate for the lighting changes during the acquisition of the series (mostly seen in first several frames in the series).

Since most image processing techniques assume the image to be additive signal, it is necessary to remap the image intensity to assure additive property. If input images are raw intensity images, a log function remapping can achieve this. If input images have been going through some remapping already, the remapping function needs to be adjusted accordingly.

To compensate for the lighting change, we apply a large neighborhood low-pass filtering on each frame to estimate the non-stationary lighting condition of that frame and subtract it. This way, the brightness of each frame in the series can be comparable.

2.5 Layer Separation

According to the model in Equation (2), we need to estimate the stent motion $T_i^S()$, clutter layer motion $T_i^C()$ and each layer jointly. Usually, it can be formulated as an energy optimization problem as follows:

$$\hat{I}_S = \arg \min_{T_i^S, T_i^C, I_C, I_S} \sum_{i \in [1,K]} \|I_i - T_i^S(I_S) - T_i^C(I_C)\|^2 \tag{4}$$

The idea behind this optimization objective function is straight forward. Assuming we can get an estimation of the stent motion $T_i^S()$, clutter motion $T_i^C()$ and the appearance of the stent and clutter layers (i.e., I_S and I_C), we should be able to predict how each acquired frame looks like without the imaging noise. Assuming the imaging noise is zero-mean independent Gaussian noise, we can derive the optimization objective function as shown in Equation (4).

This objective function is usually solved by iterative optimization steps. When we get close to the true solution, we can predict each frame more accurately and the error term is minimized. The steps are listed as follows to estimate the stent and clutter layers:

1. Estimate clutter layer motion: Since the stent usually has weak contrast, the initial clutter layer motion can be estimated based on the input images directly. In the later iterations, the estimated stent image can be removed from each input frame to improve the accuracy of the clutter layer motion estimation.
2. Estimate stent motion: the initial stent motion estimate can be obtained based on balloon markers as described in Section 2.3. In the later iterations, stent motion can be further refined with non-rigid stent motion estimation described in [1] to further refine the stent motion $T_i^S()$.

3. Clutter layer estimation: once we have the clutter layer motion estimated, we can get an initial estimation of the clutter layer as follows:

$$\hat{I}_C = \frac{1}{K} \sum_{i \in [1,K]} T_i^{C^{-1}}(I_i - T_i^S(\hat{I}_S)) \tag{5}$$

4. Stent layer estimation: based on the estimation of the clutter layer and its motion, we can obtain an estimation of the stent image as well:

$$\hat{I}_S = \frac{1}{K} \sum_{i \in [1,K]} T_i^{S^{-1}}(I_i - T_i^C(\hat{I}_C)) \tag{6}$$

5. Iterative refinement: based on the estimation results in previous steps, we can plug them into the objective function in Equation (4) for further refinement. We can further refine the estimation of $T_i^S()$, $\hat{I}_C$ and $\hat{I}_S$ iteratively. An iterative refinement of these estimation results can be achieved using gradient decent methods.

With explicit modeling of the clutter layer, we can separate the clutter layer from the stent image $\hat{I}_S$ and hence obtain a cleaner stent image than traditional averaging method.

3 Experimental Results

The algorithm is applied on more than 30 clinical sequences and very promissing results are obtained. Comparisons are done against traditional align-and-average method to see the improvements of our proposed algorithm.

The first sequence has rather good signal to noise ratio, with about 50 frames in the sequence. We can see that traditional averaging method can only blur the clutter layer, instead of removing them. The clutter structures are kind of disturbing for stent visibility. Thanks to the good signal to noise ratio, the stent can still be seen in averaging result. While our proposed layer separation method can successfully remove the unrelated clutter layer and improve the visibility of the stent dramatically.

In the second sequence, the stent has very low signal to noise ratio. We can see that the stent is just barely visible after averaging over 30 frames in the sequence. Our proposed layer separation method can successfully remove the unrelated clutter layer and enhance the visibility dramatically based on the same number of frames. The results are shown as follows:

From the experiments, we can see that our algorithm is robust to very low signal-to-noise ratio and can work in widely different imaging settings. The layer separation algorithm can successfully remove the unrelated clutter and enhance the stent visibility dramatically.

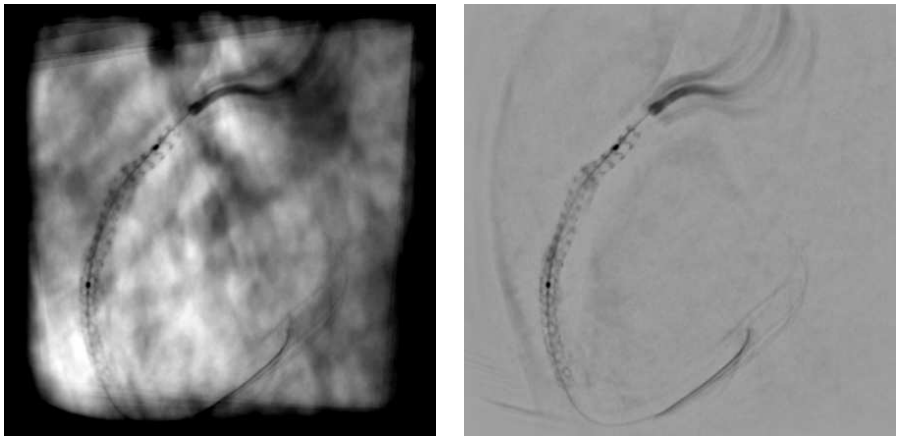

(a) (b)

Fig. 2. (a) Averaging of all frames aligned by balloon markers; (b) Our result based on layer separation.

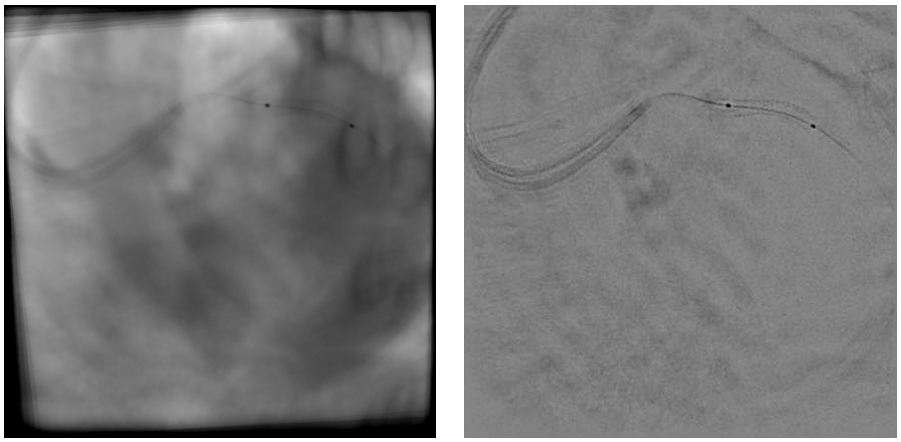

(a) (b)

Fig. 3. (a) Averaging of all frames aligned by balloon markers; (b) Our result based on layer separation.

4 Discussions

The main contribution of this work is to explicitly model and separate the stent image and the clutter layer. With this new model, we can improve the robustness and accuracy of the non-rigid registration algorithm based on the local image context. Hence we can exploit the information of the stent boundary as well as the stent strut rather than relying on guide wire detection and the assumption that the guide-wire deforms the same way as the stent. Furthermore, by separating the clutter layer, we can generate much better stent visibility than traditional align-and-average method. As a next step, further quantitative evaluation of this algorithm need to be carried out. In addition, clinical evaluation is also required to assess the clinical benefit of the proposed technique.

References

1. Ying Zhu and Christophe Chefd'hotel, "Deformable Motion Correction for Stent Visibility Enhancement", 3rd MICCAI Workshop on Computing and Visualization for (Intra)Vascular Imaging (CVII), 2011.
2. V. Bismuth and R. Vaillant, "Elastic registration for stent enhancement in X-ray image sequences", 15th IEEE Intl. Conf. Image Processing, pp. 2400-2403, Oct. 2008.
3. J.A. Garcia, N.H. Bakker, R. de Paus and J.D. Carroll, "StentBoost: a useful clinical tool", MEDICAMUNDI vol. 52 no.2, 2008.
4. G. Hermosillo, C. Chefd'Hotel, O. D. Faugeras, "Variational methods for multimodal image matching", International Journal of Computer Vision, Vol. 50, No. 3, pp. 329-343, 2002.
5. S. Lee, G. Wolberg and S. Y. Shin, "Scattered data interpolation with multilevel B-splines", IEEE Trans. Visualization and Computer Graphics, Vol. 3, No. 3, pp. 228-244, Jul-Sept 1997.
6. R. Szeliski and S. Lavallee, "Matching 3-D anatomical surfaces with non-rigid deformations using octree-splines", IJCV 18(2): 171-186, 1996.
7. Brunelli, R.: Template Matching Techniques in Computer Vision: Theory and Practice. John Wiley & Sons, (2009)
8. Gert Schoonenberg, Raoul Florent, Pierre Lelong, Onno Wink, Daniel Ruijters, John Carroll, Bart ter Haar Romeny, "Projection-based motion compensation and reconstruction of coronary segments and cardiac implantable devices using rotational X-ray angiography", Medical Image Analysis 13(4): 785-792, 2009.

Motion Adapted Catheter Navigation with Real-Time Instantiation and Improved Visualisation

Su-Lin Lee[1], Ka-Wai Kwok[1], Lichao Wang[1], Celia Riga[2], Colin Bicknell[2] and Guang-Zhong Yang[1]

[1] Hamlyn Centre for Robotic Surgery, Imperial College London, UK
[2] Academic Division of Surgery, Imperial College London, UK
su-lin.lee@imperial.ac.uk

Abstract. Robot assisted catheter navigation for endovascular intervention has improved catheter manipulation with increased precision, stability of motion, and operator comfort. However, reproducible navigation through the vasculature under fluoroscopic guidance is challenging, especially in the presence of branching vessels coupled with physiological motion. A motion adaptive catheter navigation scheme is proposed to compensate for these dynamic effects through shape modelling to permit predictive and dynamic navigations and ensure timed manipulations are synchronised with vascular motion. An effective shape modelling and real-time instantiation scheme based on sparse data for improved visualisation of the 3D anatomy during endovascular intervention is proposed. Furthermore, a simulated aortic branch cannulation procedure presented with a novel virtual endoscopic view with extensive user validation is presented to demonstrate how the derived dynamic model can be used to improve the navigation quality and efficiency during the procedure.

Keywords: shape instantiation, endovascular intervention, catheter navigation, intra-operative guidance, statistical shape modelling

1 Introduction

The introduction of robotic catheter navigation systems such as the Hansen Sensei (Hansen Medical, Mountain View, CA, USA) has facilitated the manipulation of catheters through complex anatomy with improved consistency and safety [1]. Before the full benefits of robotically assisted endovascular intervention are to be realised, however, several technical hurdles need to be overcome. Currently, most catheter navigation is performed under X-ray fluoroscopy, which provides a 2D projection of the 3D scene and is unable to show the boundaries of vessels without the use of nephrotoxic contrast. Any errors in navigation during an endovascular procedure, such as stent placement, can result in potential damage to the vessel walls, resulting in dissection, embolization or subsequent neointimal hyperplasia; likewise, excessive pressure could lead to blood vessel rupture with dire consequences.

Thus far, most existing systems relying on the use of pre-operative data for intra-operative guidance are based on co-registration of what is often a static 3D vascula-

ture, which makes them uninformative when applied to complex procedures such as those for deploying branched and fenestrated stents, usually in regions with motion and deformation. Recent advances in intra-operative imaging (e.g. fluoro-CT and XMR) have significantly simplified anatomical co-registration and localisation of dynamic details. Whilst all these techniques are able to provide detailed 3D coverage intra-operatively, their practical use for real-time continuous 3D imaging is limited by nephrotoxicity concerns or pulse-programming constraints. It is therefore more desirable to use sparse data coverage utilising optimised imaging planes taking into consideration the underlying information content or key anatomical features, combined with shape or dynamic priors to instantiate the full 3D shape.

For image guided intervention, the prediction of respiration and cardiac motion has been an ongoing research topic, corresponding to the significant need for intra-operative motion synchronization and adaptation. In dealing with cardiac and respiratory induced tissue deformation, 3D model-based registration [2, 3] and predictive adaptation during image-guided intervention have been developed [4]. During endovascular intervention, the vascular shape is affected by the cardiac cycle through two mechanisms: the first is due to the proximity of the aorta to the myocardium during contraction, and the second is the haemodynamic effects due to the pulsatile blood flow. In addition to patient specific effects, non-rigid vascular shift may also be induced during intervention, through interactions between the catheter and artery walls [5]. The presence of stent grafts, stiff wires and stent delivery devices will introduce additional vessel deformation due. Compensating for these dynamic effects through shape modelling would permit predictive dynamic modelling to ensure timed manipulations (e.g. around bifurcations) synchronised with vascular motion and deformation to ensure safety, consistency and efficiency.

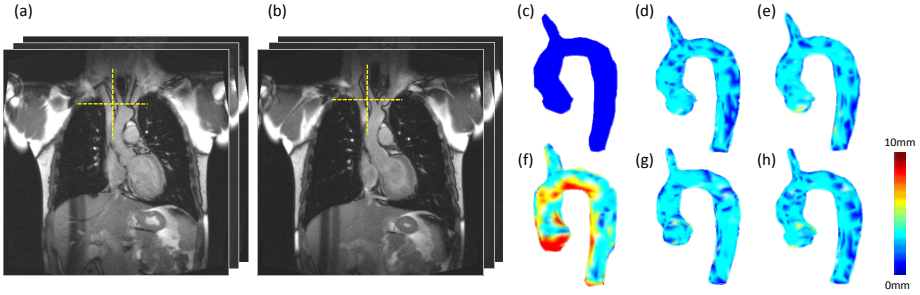

Fig. 1. An example of aorta motion as shown on one subject: (a-b) MR data from one subject at two positions in the respiratory cycle and (c-h) the aortic arch with brachiocephalic artery across the respiratory cycle, with the mesh differences to the first phase (c) displayed.

The purpose of this paper is to propose a model-guided framework for improved endovascular navigation. First, we present an effective shape modelling and real-time instantiation scheme based on sparse data for improved visualisation of the 3D roadmap during endovascular intervention. Second, a virtual endoscopic view using the model is introduced and demonstrated on a simulated aortic branch cannulation pro-

cedure with detailed user validation to show how the derived dynamic model can be used to improve the navigation quality and efficiency during the procedure.

2 Methods

2.1 Predictive Motion Model and Real Time Instantiation

The predictive motion model proposed in this paper is based on previous work on a dynamic shape instantiation framework [6]. The motion model starts with a statistical shape model (SSM) of the vasculature that can be built group-wise or on a subject specific basis. With the complexity of the aortic arch and variation in the arrangement of aortic branches arising from the aortic arch across subjects, it is desirable to create subject-specific models. For each phase of the respiratory cycle, a few landmarks were sampled on the hemi-diaphragm contour on the imaging data. These positions and the corresponding 3D models of the aortic arch were used to train the dynamic shape instantiation. Further models could then be obtained using other respiratory positions.

A Kalman filter [7] was used to predict the positions of the respiratory cycle across time. The measurements z_k are the diaphragm positions measured from the MR images and are used to update the Kalman filter for each state k:

$$\hat{x}_k = \hat{x}_k^- + K_k\left(z_k - H\hat{x}_k^-\right) \tag{1}$$

K_k is the Kalman gain, H is a matrix relating the state to the measurements z_k and $\hat{x}_k$ and $\hat{x}_k^-$ are the state estimate and *a priori* state estimate, respectively.

The filter was used with an input stream of respiratory positions to correct for and update the estimations of the current state of respiration. These predictions were then used as input to the shape instantiation to determine the 3D mesh at that respiratory phase.

With the dynamic shape instantiation framework [6], real-time instantiation is possible as the calculations reduce to a matrix multiplication. The method is based on partial least squares regression:

$$\hat{Y} = XB_{PLS} \tag{2}$$

$$B_{PLS} = \left(P^{T+}\right)DQ^T \tag{3}$$

New inputs X created by the predicted respiratory positions will be multiplied by matrix B_{PLS} to generate $\hat{Y}$, the vertices of the entire mesh shape. Q is the loading matrix on Y, D is a matrix with the regression weights on the diagonal, and P^{T+} is the pseudoinverse of the transpose of P, the loading matrix on X. The faces connecting the vertices do not change and are the same as those for each of the files in the training set.

2.2 Image Acquisition

Subject Study
MR images of the ascending and descending aortas from 8 normal subjects (4 male and 4 female) were acquired on a Siemens Avanto 1.5T scanner. Approximately 50 single-shot coronal images covering the entire lung field of each subject were acquired using a steady state free precession sequence (TR = 2.8ms, TE = 1.2ms, asymmetric echo, in-plane resolution = 1.6×1.6mm, slice thickness = 4mm, slice separation = 0.8mm). The subjects were free breathing and the scans were cardiac gated with imaging performed in diastole.

The location of the dome of the right hemi-diaphragm was determined using a MR navigator and recorded immediately before and after the acquisition of each coronal image. These were recorded into a text file for the timings to be determined subsequently. The multi-slice coronal acquisitions were repeated 40 times to cover a number of positions in the respiratory cycle. A respiratory feedback system was developed to avoid changes in the breathing cycle for the duration of the scan. The navigator positions were fed to a strip of LED lights that were visible to the subject being scanned; this encouraged the subject to keep their breathing constant. This imaging sequence was originally developed for imaging of the lungs [9].

The aortic arches and brachiocephalic arteries were segmented and meshed. A statistical shape model was built from the data and used in the predictive motion model and the mean errors of the predicted models were calculated.

Phantom Study
A silicone vascular phantom (Elastrat Sàrl, Geneva, Switzerland) was scanned in a GE Innova 4100 interventional X-ray machine. Five 3D CT scans were obtained at five different dynamic positions, generated by inserts next to the ascending aorta, simulating the respiratory motion observed in the subject study. The structure was segmented and meshed using Analyze (AnalyzeDirect, Inc., Overland Park, KS, USA).

The meshed data was input to the prediction motion model, with the number of inserts used in place of respiratory positions. The meshes along a respiratory cycle lasting 4 seconds, with diaphragm positions determined using the equation defined in [8], were predicted and mean errors were calculated for each of the five predicted meshes using a leave-one-out study. The optimal projection plane was determined accordingly.

2.3 User Evaluation with Virtual Endoscopic View

The meshes of the silicone phantom derived from the predictive motion model were used along with an estimated kinematic model of the robotic catheter based on its known tendon-wiring structure. This simulation environment allows for detailed assessment of the predicted motion model to perform timed manipulation through deforming bifurcations. With the predicted mesh deformation and the position of the

robotic catheter tip known, a virtual endoscopic view can be generated, where the operator can 'drive' through the vessels using a simulated camera on the catheter tip.

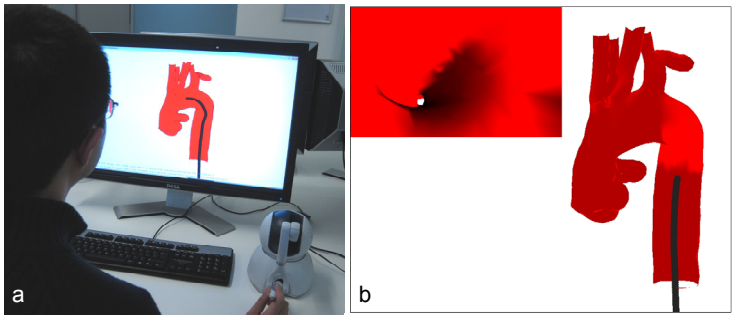

Fig. 2. The setup of the user evaluation experiments: (a) the user evaluation experiment setup with the Omni Phantom (without virtual endoscopy) and (b) a screenshot of the experiment with virtual endoscopy in the top left corner.

A total of 9 subjects (all right hand dominant and inexperienced operators) were recruited to assess the effect of visualizing the shape instantiated prediction of the aorta dynamics when performing a simulated cannulation of the left subclavian artery. The manipulation of the catheter was controlled by an Omni Phantom device (SensAble Tech. Inc., USA) and the operators were advised of the risks of making wall contact with the catheter tip. Each subject performed the procedure twice – with and without the virtual endoscopy – and operators were allowed to adjust the orientation of the 3D model during the procedure. The basic setup for user evaluation is shown in Fig. 2 with a screenshot of experiments without and with the virtual endoscopic view.

The experiments were performed with the phantom visualisation in the AP direction. The order in which the experiments were performed was randomised in order to remove any bias caused by the learning effect. The following performance indices were recorded:

- number of catheter tip-mesh collisions
- duration the catheter tip is along the mesh walls
- completion time
- path length of the catheter tip
- mean deviation of the catheter tip from the optimal path (defined by the centreline of the mesh)

A Kruskal-Wallis non-parametric test was used to assess differences between procedures performed with and without virtual endoscopy and to determine whether the results were statistically significant.

3 Results

In Fig. 3a, the range of the errors for the leave-one-out validation on the phantom data is shown. It was determined that visualization in the phantom's AP direction provided

the most information of the dynamics of the dynamic aorta phantom. The range of the errors across the respiratory cycle for each subject is shown in Fig. 3b. While most of the errors are within a few millimetres, the large errors shown in Subject 7 may be due to misregistration during data acquisition. The results of the prediction model on a single respiratory cycle of the eight subjects are shown in Fig. 4.

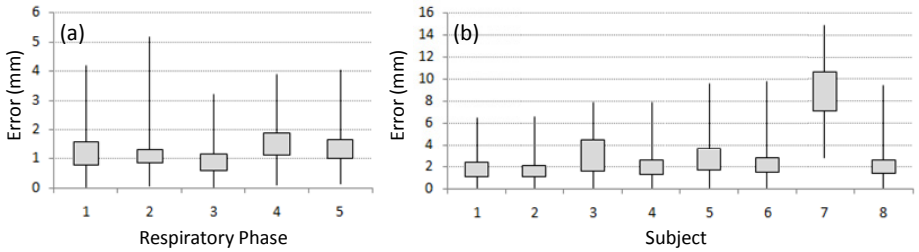

Fig. 3. The median, minimum, maximum and first and third quantiles are shown in the box and whisker plots for the data across (a) the leave-one-out study of the dynamic silicone phantom and (b) the respiratory cycles of the eight subjects.

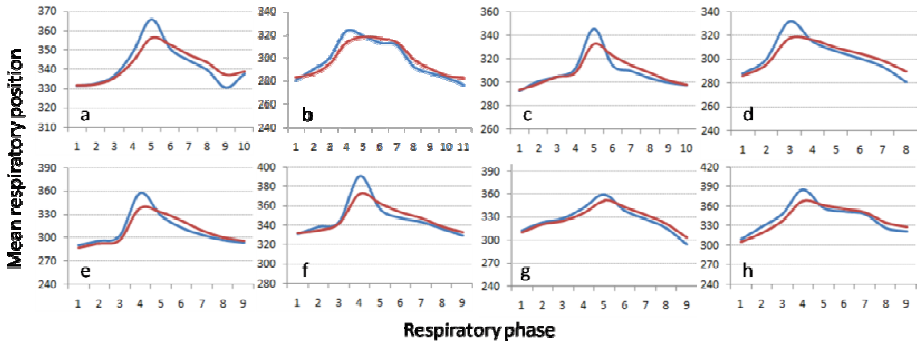

Fig. 4. Comparison of mean respiratory cycle landmark position for the prediction and ground truth inputs for each of the eight subjects (a-h are Subjects 1-8 respectively). The ground truth of the respiratory positions is shown in blue and the predicted cycle is in red.

A summary of the performance indices recorded is shown in Table 1; the means and standard deviations of each index are shown both with and without virtual endoscopy. Overall, performance metrics improved significantly during cannulation of the LSA using virtual endoscopy (Kruskal-Wallis; $p<0.05$). Most importantly, the number of mesh collisions and the duration of time the catheter tip was pressed against the vessel wall reduced markedly, suggesting improved safety of cannulation. All subjects commented on how virtual endoscopy made the procedure easier and all chose not to reorient the 3D model when using virtual endoscopy.

The performance results are shown in Fig. 5. It is evident that the overall performance of the users has improved significantly with the use of the virtual endoscopy view for guidance, with the catheter tip path becoming smoother and the procedure time and mean deviation of the centreline decreasing, suggesting safer catheterisation.

Table 1. Summary of the performance indices in the user evaluation experiments.

	Without Virtual Endoscopy		With Virtual Endoscopy	
	Mean	**SD**	**Mean**	**SD**
Completion time, s	107.8	46.3	**71.8**	**36.3**
Path length, mm	882.9	648.8	**395.0**	**147.0**
Path deviation, mm	10.9	4.0	**5.8**	**0.8**
No. of mesh collisions	8.4	9.5	**1.3**	**2.2**
Duration along walls, s	4.2	3.4	**0.6**	**0.9**

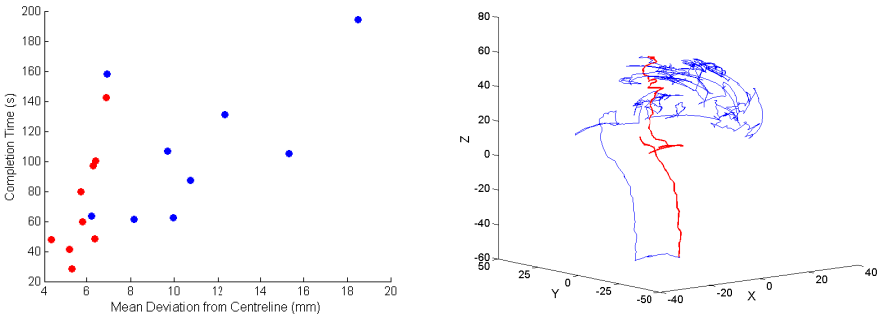

Fig. 5. (Left) A comparison of the performance of the users with (red) and without (blue) the virtual endoscopic view, showing the completion time and mean deviation from the centreline. (Right) A comparison of the catheter tip travel path for Subject 4 with (red) and without (blue) the virtual endoscopic view.

4 Discussion and Conclusion

In this paper, we have presented a motion adapted catheter navigation scheme with shape modelling and real-time instantiation. The benefit of the proposed framework is its ability to instantiate shapes outside the training set and its use as the basis of the predictive motion model for intra-operative navigation. The use of this predictive motion model can also be used for active constraints [10] for robotic catheter navigation, providing a dynamic pathways and safety margins. For endovascular intervention, the method can be used at other locations; in particular, this can be applied to the renal arteries, where there is great motion due to their proximity to the diaphragm.

A virtual endoscopic view was also demonstrated for intraoperative endovascular navigation. Detailed user evaluation results have shown that this visualisation of the dynamics of the vasculature can facilitate adaptive path planning and timed synchro-

nisation, thus improving the overall safety and consistency of the intervention procedures.

Acknowledgements

The authors wish to thank Mirna Lerotic and Jennifer Keegan for their assistance with data acquisition.

References

1. Riga, C.V., Bicknell, C.D., Hamady, M.S., Cheshire, N.J.W.: Evaluation of robotic endovascular catheters for arch vessel cannulation. Journal of Vascular Surgery 54 (2011) 799-809
2. Danilouchkine, M., Westenberg, J., van Assen, H., van Reiber, J., Lelieveldt, B.: 3D Model-Based Approach to Lung Registration and Prediction of Respiratory Cardiac Motion. In: Duncan, J., Gerig, G. (eds.): Medical Image Computing and Computer-Assisted Intervention (MICCAI), Vol. LNCS 3750. Springer Berlin / Heidelberg, Palm Springs, CA, USA (2005) 951-959
3. Yang, D., Lu, W., Low, D.A., Deasy, J.O., Hope, A.J., Naqa, I.E.: 4D-CT motion estimation using deformable image registration and 5D respiratory motion modeling. Medical Physics 35 (2008) 4577-4590
4. King, A.P., Rhode, K.S., Razavi, R.S., Schaeffter, T.R.: An Adaptive and Predictive Respiratory Motion Model for Image-Guided Interventions: Theory and First Clinical Application. IEEE Transactions on Medical Imaging 28 (2009) 2020-2032
5. Kesner, S., Yuen, S., Howe, R.: Ultrasound Servoing of Catheters for Beating Heart Valve Repair. Information Processing in Computer-Assisted Interventions (IPCAI), Geneva, Switzerland, LNCS 6135 (2010) 168-178
6. Lee, S.-L., Chung, A., Lerotic, M., Hawkins, M., Tait, D., Yang, G.-Z.: Dynamic Shape Instantiation for Intra-operative Guidance. In: Jiang, T., Navab, N., Pluim, J., Viergever, M. (eds.): Medical Image Computing and Computer-Assisted Intervention (MICCAI), Vol. LNCS 6361. Springer Berlin / Heidelberg, Beijing, China (2010) 69-76
7. Kalman, R.E.: A New Approach to Linear Filtering and Prediction Problems. Transactions of the ASME - Journal of Basic Engineering 82 (1960) 35-45
8. Lujan, A.E., Larsen, E.W., Balter, J.M., Ten Haken, R.K.: A method for incorporating organ motion due to breathing into 3D dose calculations. Medical Physics 26 (1999) 715-720
9. Lerotic, M., Lee, S.-L., Keegan, J., Yang, G.-Z.: Image constrained finite element modelling for real-time surgical simulation and guidance. Proceedings of the Sixth IEEE International Conference on Symposium on Biomedical Imaging: From Nano To Macro, Boston, Massachusetts, USA, (2009) 1063-1066
10. Kwok, K.-W., Mylonas, G., Sun, L., Lerotic, M., Clark, J., Athanasiou, T., et al.: Dynamic Active Constraints for Hyper-Redundant Flexible Robots. In: Yang, G.-Z., Hawkes, D., Rueckert, D., Noble, A., Taylor, C. (eds.): Medical Image Computing and Computer-Assisted Intervention (MICCAI), Vol. LNCS 5761. Springer Berlin / Heidelberg, London, UK (2009) 410-417

Reconstruction of Stent Induced Loading Forces on the Aortic Valve Complex

Raoul Hopf[1,*], Michael Gessat[3], Volkmar Falk[2], Edoardo Mazza[1]

[1]Institute of Mechanical Systems, Department of Mechanical Engineering, Swiss Federal Institute of Technology (ETH), Switzerland
{rhopf, emazza}@ethz.ch
[2]Division of Cardiovascular Surgery, University Hospital Zurich, Switzerland
volkmar.falk@usz.ch
[3]Computer Vision Laboratory, Department of Electrical Engineering, Swiss Federal Institute of Technology (ETH), Switzerland
mgessat@ethz.ch

Abstract. In order to evaluate the performance of stents used in transcatheter aortic valve implantation (T-AVI), finite element simulations are set up to reconstruct patient specific contact forces between implant and its surrounding tissue. The reference geometry of the stent is obtained using micro-CT scanning data. A procedure is defined to create a numerically efficient and robust model of the stent made of beam elements. The model is validated with experiments applying representative loading cases. Post-op CT image data provide patient specific displacement maps used to define kinematic boundary conditions for the finite element simulation. An approach to deal with the issue of spurious strains induced by measurement uncertainties from CT images is proposed. Maps of radial forces acting on the aortic tissue are obtained.

Keywords: tavi, aortic stent, corevalve, simulation, contact forces

1 Introduction

Knowledge about the contact forces between a medical implant and its surrounding tissue can provide essential information on the overall performance of the implant. In particular, in the case of transcatheter aortic valve implantation (T-AVI). Insufficient contact forces between stent and tissue might cause paravalvular leaks [1]. On the contrary, excessive contact forces are suspected to impair the conductibility of the atrioventricular (AV) node, the bundle of His, and/or the left bundle branch. All three result in bradicaridal arrhythmia, which is a common complication after T-AVI, usually requiring pacemaker implantation [2]. The two main risk factors which could be identified as significant in clinical studies are (i) the type of valve selected for implantation and (ii) valve oversizing (resulting in high radial loads) [2,3]. These findings indicate a connection between mechanical stress induced on the tissues and the necessity for a pacemaker after T-AVI. Nevertheless, there exists no quantitative investigation of this relationship, which would allow predicting or help reducing the onset of conduction abnormalities after T-AVI.

adfa, p. 1, 2011.

In order to provide clinical research with a tool for quantitative analysis of stent-tissue interaction, for T-AVI as well as for other applications, a general concept has been developed for the reconstruction of the state of deformation of the stent as well as the contact forces between implant and tissue in-vivo.
The novel procedure (M. Gessat, V. Falk, E. Mazza, R. Hopf, Swiss/EU patent application, submitted) is based on two key elements: force balance at the stent-tissue interface and the availability of high-resolution geometrical data of the stent before and after implantation. In fact, in order to obtain the stress field at the contact points, it is sufficient to determine the boundary conditions corresponding to the measured state of deformation of the stent. Modern medical imaging systems, such as CT, provide the possibility to acquire high-resolution image data, which can be used to reconstruct deformed implant geometries in three dimensions.

An exemplary implementation of the concept is shown for the determination of contact forces between stent and tissue after T-AVI. The procedure uses geometrical data obtained from high-resolution medical imaging systems and the force field is reconstructed through finite element simulations. The present analysis is performed for the Medtronic CoreValve Revalving System (Medtronic, Minneapolis USA).

2 Methods

In a first step, a micro-CT scan of the implant is acquired from which a finite element mesh is generated corresponding to its undeformed reference configuration. Experimental validation is used to evaluate the reliability of the stent model. To obtain the actual in-vivo displacement field after implantation, postoperative CT images are analyzed. With help of this data a discrete displacement map for all junction points of the stent is obtained. This nodal displacement field is used to impose kinematic boundary conditions at the corresponding nodes of the stent model. Due to the measurement uncertainty, directly applied boundary conditions lead to high noise in the reconstructed force field. Therefore a system using nonlinear connector elements is introduced, in order to apply boundary conditions with tolerances corresponding to the limits given by measurement uncertainties. All meshing and simulation set up is carried out in MATLAB (MathWorks) and then exported in form of a finite element input file. Subsequently, simulations are solved using the program ABAQUS/standard (Dassault Systèmes Simulia Corp., Providence, RI, USA). In post processing steps (MATLAB), the reaction force field is visualized. Lower bound thresholds are set to determine zones that can be regarded as stress-free due to weak or no contact between stent and tissue.

2.1 Modeling the Reference Geometry

Stent model implementations found in current literature are mostly set up using full three dimensional solid element formulations [4,5]. Meshes using a variety of element formulations, different resolutions and integration schemes can be found. Due to the slender substructure which is largely subject to bending, tension and torque states of

loading, three dimensional element formulations can yield numerical problems, such as shearlocking and hourglassing modes. In order to compare with the performance of the beam model formulation, first a full solid meshing system is implemented. This model then is used to perform a convergence study for three different states of deformation.

The geometry of the stent as extracted from CT images consists of 30 strings (Fig.1: green) and 165 intersection points (Fig.1: red). The strings have a rectangular profile with an average width and height of 0.2mm and 0.48mm. From micro-CT imaging data, Bézier splines defining the center line of each string of the undeformed stent can be fitted [8]. These splines are defined piecewise, using a 4-point control polygon. The first step in the meshing process is to discretize the string center lines as shown in Fig 1. The sampling rate to generate the center line nodes is adjustable.

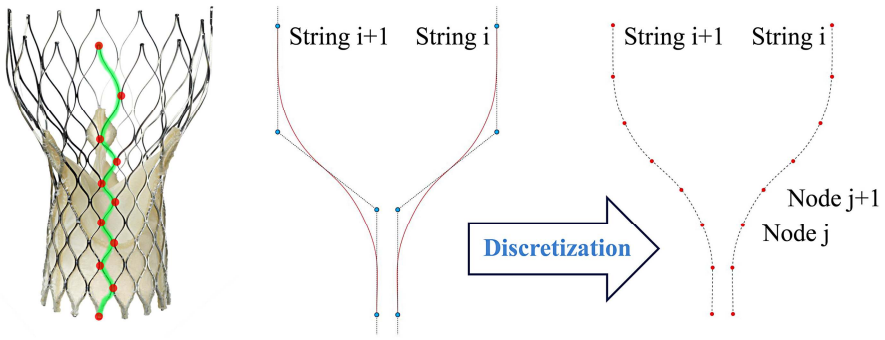

Fig. 1. Stent including leaflets (not modeled) with highlighted a string (green) and according intersection points (red). Bézier-control polygons and discretized center lines.

One of the main difficulties in meshing three dimensional structures with beam elements is to maintain correct orientation for all elements with respect to the geometry and the norm of the finite element solving system that is used. For this purpose, every node on the center line is provided with a local coordinate system, that holds the tangent vector of the spline and two normal vectors which form an orthonormal, right-handed trihedron. The tangents can directly be obtained from the definition of the Bézier splines. The outward normal is calculated from a global cylindrical coordinate system and the tangent, whereas the second normal is obtained from the first two vectors.

The beam element model requires the discretized center lines of the strings and the definition of a cross section. The chosen elements for this model are three dimensional first order two point Timoshenko beam elements (element type B31 in ABAQUS). In order to avoid initial twists or curvatures, both starting- and endpoint of the element need to be provided with the corresponding tangent- and normal vectors. These are obtained by interpolating the vectors which were used to define the nodal coordinate systems. At each intersection point, both corresponding nodes of the neighboring strings are coupled using kinematic equations in all six degrees of freedom.

For the solid model the cross section is discretized in a plane reference system and then transformed into the according local nodal systems. The nodes are connected to form first order, hexahedral solid elements and a reduced integration scheme is applied (element type C3D8R in ABAQUS).

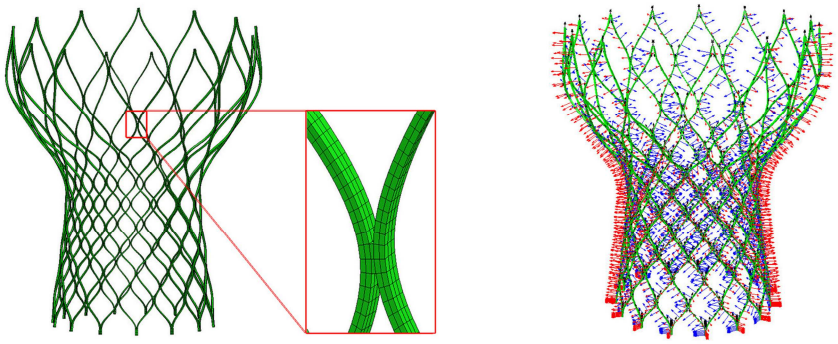

Fig.2. Solid model (left) with a close up view of the mesh (middle). Beam element model (right) with rendered beam profiles and element orientation vectors.

The material used in CoreValve is a nickel-titanium alloy (Nitinol), which exhibits super elastic properties to be able to fully recover from strains of up to 10% as a result of the stents crimping process to the catheter. The constitutive model used for the present study is a linear elastic Hookean solid. In fact, the crimping process is not included in the analysis and, the final deformed state of the stent may include finite rotations but deformation is expected to remain in the small strain regime. Overestimation of stiffness due to choosing a linear elastic model was observed when comparing with experimental data at large deformations, see section 2.3.

2.2 Evaluation of the Influence of Mesh Size

The convergence study is performed using four mesh resolutions ranging from orders of 10'000 (grade 1) to 600'000 (grade 4) elements for the solid model. Approximately 4'000 elements are used for the beam model. Three different global loading states are tested. Fig. 3 shows the results of the analysis of mode 1 loading (global tension) for the four mesh configurations of the solid model. Mode 2 was defined as a global compression and mode 3 a torsional state. The results of modes 2 and 3 are consistent with Fig. 3. An important remark concerns the result of grade 1. Due to the low mesh resolution the profile has only one element in the cross section. The reduced integration scheme for first order elements in states of bending therefore lead to zero-energy deformation modes (hourglassing), which yields completely unrealistic results as seen in Fig. 3. The same deformation modes were applied to the beam element model which provides results for all modes comparable with grades 3 and 4, but with only around 25'000 degrees of freedom.

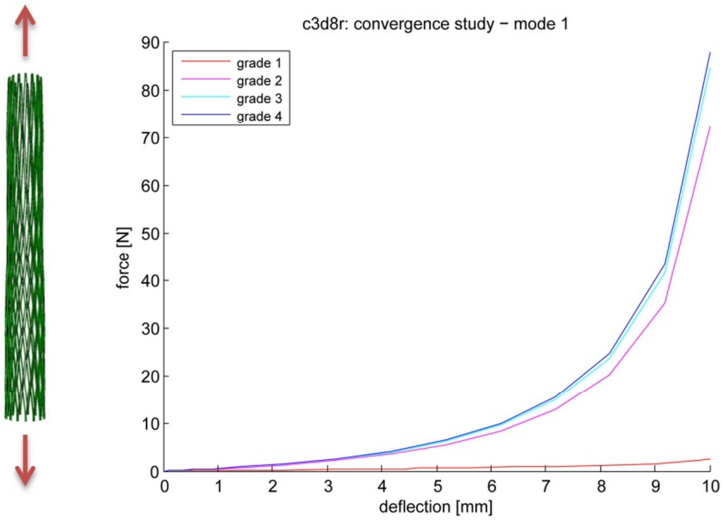

Fig. 3. Mode 1 and results of the corresponding analysis for all mesh resolutions.

2.3 Experimental Validation

The experimental validation of the beam model is performed with one dimensional two point tensile tests. Three configurations were investigated: One symmetrical mode and two nonsymmetrical modes (mode 1 shown in Fig. 4).

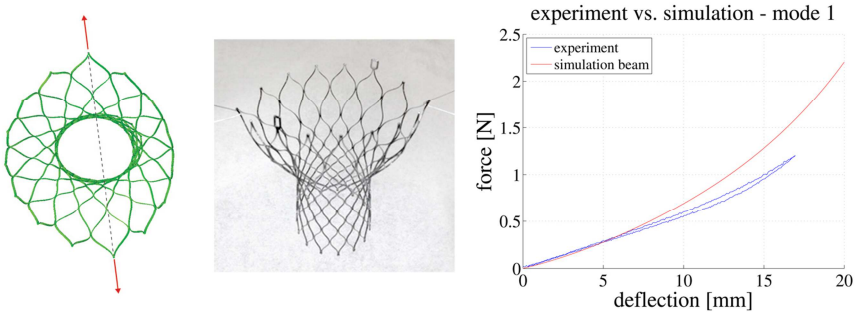

Fig. 4. Mode 1: FE-model, experiment, measured curve (blue) and simulation (red).

Such experiments are relatively easy to perform and mechanically well defined in terms of boundary conditions. In spite of the one dimensional boundary conditions, the coupled grid structure of the stent leads to complex states of deformation, which test both structural as well as constitutive model reliability.

Simulations show good predictive capabilities for low to moderate deflections but a clear overestimation of stiffness for larger deformations. This is deemed to be a consequence of the chosen linear elastic constitutive model. The super elastic material

behavior of Nitinol shows lower stresses at the corresponding level of deformations imposed in the experiments.

2.4 Boundary Conditions for Postoperative Simulation

In order to obtain a patient-specific measurement for the deformation of the CoreValve stent after implantation, a sparsely sampled deformation field is generated. Therefore, the 165 intersection points which define the stent's grid structure are automatically extracted from CT images. With a high spatial resolution (< 0.4 mm in all axes), these intersection points are well visible in CT images as small, well-defined clusters of high-intensity voxels due to the high X-ray contrast of Nitinol. Nevertheless, calcium clusters and image artifacts can create similar clusters or create enough background noise to merge neighboring clusters. A combination of threshold filtering and model-based generation of hypotheses for likely positions of these intersection points is applied in order to identify the intersection points. In practical tests with 25 patient datasets, the proposed method has proved reasonably robust to image noise and calcium. Due to sampling effects and image blurring, the spatial accuracy of the landmark localization was evaluated to be in the range of two voxel lengths, i.e. 0.8 mm.

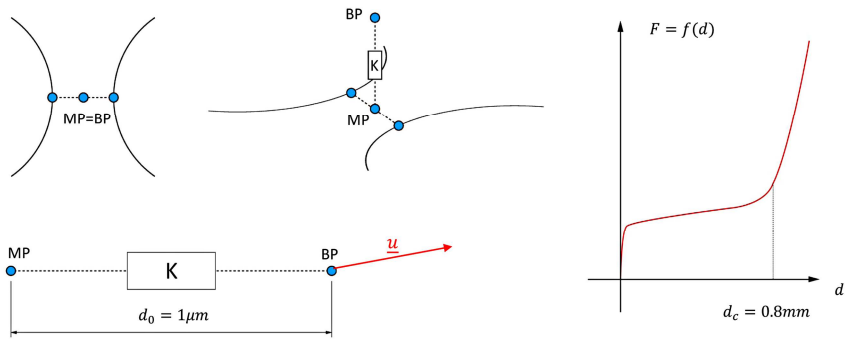

Fig. 5. Intersection middle point (MP), boundary point (BP), connector element (K) and the corresponding nonlinear force law.

If this deformation map was be used directly to impose kinematic boundary conditions at the intersection points, the high ratio of tensile to bending stiffness in beam-like structures would yield large fluctuations in the values of calculated external forces, due to inaccuracy in intersection point position measurement. Therefore an intermediate step was introduced in order to relax these spurious forces. The proposed method is illustrated in Fig. 5. A middle (MP) point is calculated for each intersection. An additional boundary point (BP) in radial direction towards the center of the stent is created. The distance between MP and BP in the undeformed configuration is by orders of magnitude smaller than the applied displacements.. The middle point and the boundary point are connected with a nonlinear force element (K). The force law for the connector element is set up to have a cut-off at approximately d_c=0.8 mm, which

corresponds to the uncertainty of the CT-data. The measured displacement is now applied at the boundary point, instead of the middle point directly. This allows the actual physical middle points to position themselves within a spherical volume around the nominal position to account for measurement uncertainty, thus leading to a global minimum of potential energy in the stent. This approach avoids artificially high reaction forces and provides a lower limit for the actual force field acting on the stent in-vivo.

3 Results

The discrete vector field containing the nodal reaction forces of each intersection point is imported into MATLAB for post processing. The radial components of the forces can be represented as arrows in a three dimensional plot, or their values reported for all nodes along selected paths, as shown in Fig. 6. The green dots correspond to the plotted arrows at nodes 1-7 in the diagram. The sign of the nodal plot was chosen to indicate whether the force points radially inward or outward. Reaction forces in outward direction are considered as artifacts, since the surrounding tissue will not exhibit any adhesion properties in comparable magnitudes. These negative contact forces possibly indicate a local underestimation of the measurement uncertainty in the post-op CT data.
The average value of radial force divided by the corresponding aortic tissue area, typically yields a radial pressure in the range of 30-40 mbar. These stress levels seem plausible when compared with the average values of blood pressure fluctuation between systolic and diastolic pressure (approx. 50 mbar).

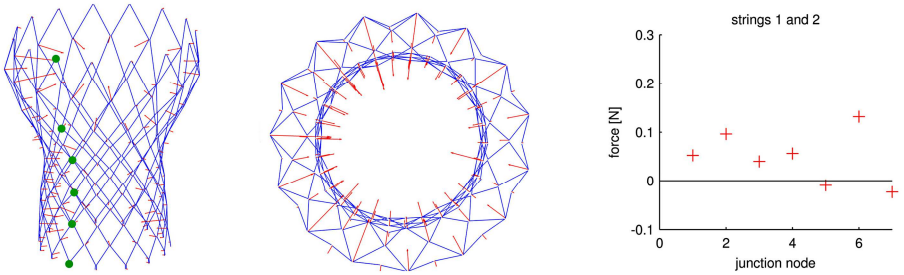

Fig. 6. Three dimensional plot of the force field and nodal force plot.

4 Conclusions

An effective beam model of the CoreValve aortic stent has been created, compared to solid element models and validated experimentally. A method to extract a patient specific nodal deformation map from medical imaging data and a corresponding procedure to deal with measurement uncertainty have been developed. The model per-

formed well in terms of efficiency as well as robustness and showed good predictive capabilities in low to moderate ranges of displacement corresponding experiments.

The feasibility of the novel procedure for reconstruction of stent-tissue interaction from medical images of in-vivo stent deformation has been demonstrated. Previous studies using finite element simulation for post-operative outcomes have used medical imaging systems to obtain patient specific data [4-7]. This data was then used to either model patient specific vascular geometries, or to obtain global information of the implanted stent. However, to the best of our knowledge so far procedure exists to obtain contact forces between stent and tissue from post-op data.
The application of displacement boundary conditions needs further investigation to minimize the artifacts related to measurement uncertainties and avoid local underestimation of contact forces. Further, considering future applications that involve the crimping and releasing processes, a non-linear constitutive model has to be implemented able to reproduce the super elastic properties of Nitinol.

5 Acknowledgements

The project was supported by the Swiss National Science Foundation (SNSF, project nr: CR32I3 135044) and the Swiss Heart Foundation.

6 References

1. M. Padala, E.L. Sarin, P. Willis, V. Babaliaros, P. Block, R.A. Guyton und V.H. Thourani, An engineering review of transcatheter aortic valve technologies. Cardiovasc. Eng. Technol. 1:77-87, 2010.
2. M.Z. Khawaja et al., Permanent pacemaker insertion after CoreValve transcatheter aortic valve implantation: incidence and contributing factors (the UK CoreValve collaborative). Circulation 123:951-960, 2011.
3. J.M. Bosmans et al., Procedural, 30-day and one year outcome following CoreValve or Edwards transcatheter aortic valve implantation: results of the Belgian national registry. Interact. Cardiovasc. Thorac. Surg. 12:762-767, 2011.
4. C. Capelli, G.M. Bosi et al., Patient-specific simulations of transcatheter aortic valve stent implantation, Med. Biol. Eng. Comput. (2012) 50:183–192
5. Tzamtzis S, et al. Numerical analysis of the radial force produced by the Medtronic-CoreValve and EdwardsSAPIEN after transcatheter aortic valve implantation (TAVI). Med Eng Phys (2012)
6. A. Ganguly, R. Simons et al., In-vitro imaging of femoral artery nitinol stents for defmation analysis. J Vasc Interv Radiol. 2011 Feb;22(2):236-43
7. A. Ganguly, R. Simons et al., In-vivo imaging of femoral artery nitinol stents for deformation analysis. J Vasc Interv Radiol. 2011 Feb;22(2):244-9
8. M. Gessat, L. Altwegg, T. Frauenfelder, A. Plass, V. Falk, Cubic hermite bezier spline based reconstruction of implanted aortic valve stents from CT images, Proc. of the 33rd Annular International Conference of the IEEE Enginnering in Medicine and Biology Society (EMBC) 2011, August 2011

Role of 3D/3D and 2D/3D Registration in Computer-Assisted Stenting of Aneurysms

Gouthami Chintalapani and Ponraj Chinnadurai

Siemens Medical Solutions USA Inc.,
Hoffman Estates, IL 60192, USA,
{gouthami.chintalapani, ponraj.chinnadurai}@siemens.com

Abstract. Endovascular treatment of aneurysms uses a combination of 3D images (preoperative CT/MRI or intra-procedural C-arm CT images) and 2D images (fluoroscopy/subtracted angiography) for pre-treatment planning, navigation, device deployment, and post treatment assessment. More often, 3D images and 2D fluoroscopic/angiographic images are displayed on separate monitor displays and the information is visually correlated by the physician. Although many robust image registration algorithms exist, the applicability of these algorithms is very limited in an actual clinical setup due to their complexity, context sensitivity, and user interactivity. This paper explores the scope of image registration, both 3D/3D and 2D/3D, during various stages of computer assisted aneurysm treatment workflow. Examples from clinical procedures such as embolization of intracranial aneurysm and abdominal aneurysm treatment with stent grafts are presented highlighting associated challenges and opportunities.

Keywords: image registration, aneurysm treatment, aneurysm embolization, computer-assisted stenting, image-guided navigation

1 Introduction

Aneurysms are generally characterized as abnormal dilatation of blood vessels due to vessel wall weakening, that can pose life-threatening complications like impending risk of vessel wall rupture resulting in bleeding. As opposed to open-surgical repair, percutaneous endovascular approach offers a viable, less-invasive alternative treatment option for aneurysms. The primary goal of endovascular aneurysm treatment is to embolize (limit the flow into) the aneurysm (by means of devices such as stents and coils, flow-diverters, stent-grafts etc) thereby promoting blood clot formation within the aneurysm while maintaining the blood flow in the parent vessel. Irrespective of the location of aneurysms (eg. small intracranial vessels, thoracic and abdominal aorta), three-dimensional (3D) imaging plays an important role in pre-treatment planning, intra-procedural guidance and post-treatment follow-up. Although pre-and post-treatment imaging involves CT (Computed Tomography) and/or MR (Magnetic Resonance) imaging, endovascular treatment of aneurysm is usually performed under the guidance

of X-ray 2D-fluoroscopic and/or 2D digital subtraction angiographic (DSA) images acquired by an angiographic C-arm system. In addition, latest generation of C-arm imaging systems can also acquire 3D images (C-arm CT) that can provide additional 3D information for navigation and guidance during the procedure [3]. Information from various imaging modalities such as pre-operative CT or MR, inter-procedural C-arm CT and fluoroscopic images can be fused for planning, navigation, and post-treatment assessment.

The concept of image registration has been around for decades and several robust 3D/3D and 2D/3D registration algorithms have been published in literature [5, 7]. Features such as points, lines, curves, regions are detected in images and matched using metrics such as correlation, mutual information. A transformation is computed that maps the moving image to the fixed image and the resulting transformation is applied to the moving image. All these algorithms differ mainly in the features selected, methods used to detect the features and the metrics used to match features. Moreover, these algorithms are customized to register specific anatomical organs. The wide variety of image features, similarity metrics, anatomical organ and clinical context dependency increases the complexity of registration algorithms, thus making it less practical during treatment in a clinical setup. Even in current clinical practice, establishing meaningful correspondence between these various 2D and 3D image information still remains a challenge.

This paper explores the role of image registration in computer assisted endovascular treatment of aneurysms. Images from 3D preoperative scans can be registered to the intra-procedural 2D and 3D images at various stages of aneurysm treatment such as planning, navigation, device deployment, and post-deployment assessment. This paper presents all such possibilities of image registration using a wide variety of features such as anatomical landmarks, manual annotations, images themselves, and stent markers. Several clinical examples from intracranial and abdominal aortic aneurysm treatment procedures are illustrated highlighting associated challenges.

2 Methods

This section highlights the importance of registration in computer assisted stenting and presents various examples of image registration used in actual clinical cases. All intra-procedural imaging is performed on C-arm angiographic Systems, Artis Zee® biplane (VC14h) and Artis zeego® (VC14h) (Siemens AG, Forchheim, Germany) and image registration was performed using tools like syngo Inspace 3D/3D Fusion® and syngo iPilot Dynamic® (Siemens AG, Forchheim, Germany) 2D/3D registration available at the clinical workstation (Leonardo XWP, VB15D, Siemens Medical Solutions USA Inc.).

2.1 Role of Image Registration

Image registration plays a key role in computer assisted aneurysm treatment procedure as shown in Figure 1. Pre-treatment planning involves meaningful

correlation of morphological information about aneurysms from pre-procedural CT and/or MR images to decide on the optimal treatment procedure. Thereafter, when the patient is in the interventional angiographic suite, 3D-DSA/C-arm CT images can be acquired and reconstructed as 3D volumes. Information such as size of the aneurysm and blood vessel, optimal C-arm angle for projection 2D imaging could be derived from these 3D imaging data.

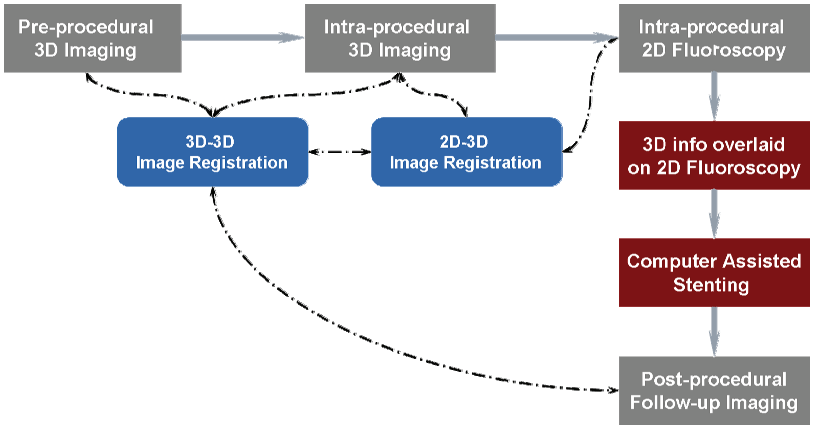

Fig. 1: Schematic showing the role of image registration in computer assisted stent procedure

Intra-procedural image-guided navigation or stent deployment relies primarily on 2D-3D image registration strategies, as most of the realtime catheter and device manipulations are performed under live 2D fluoroscopy. The information from 3D images could be overlaid onto realtime fluoroscopic images thereby providing realtime image guidance that updates dynamically with image zoom, C-arm and table movements. Such realtime fluoroscopic overlay can also help with finding optimal C-arm angle for device deployment and also can possibly reduce the usage of iodinated contrast agent for conventional angiography.

Post-treatment assessment involves 3D-3D registration of pre- and post-procedural images (CT/MR/C-arm CT), that helps with studying the 3D relationship of the device to the vessel wall/aneurysm.

2.2 Computer-Assisted Aneurysm Treatment Workflow

Figure 2 shows detailed workflow for computer assisted treatment of intracranial aneurysms and aortic aneurysms. For intracranial aneurysm treatment, planning is typically performed on intra-procedural 3D DSA images. Planning involves studying aneurysm dimensions for determining the right device (stent, coils, or flow diverter), optimal working view angle, marking landmark features such as aneurysm neck, proximal and distal landing zones for the stent and if available,

virtual stent simulation. All this information is overlaid on to the live fluoroscopic screen for image guidance during navigation using 2D/3D registration. Once deployed, intra-procedural C-arm CT images can be obtained and the device apposition to the vessel wall can be studied. For further coiling assistance, devices can be extracted from C-arm CT images and overlaid onto the fluroscopic screen. Post deployment assessment can be performed by fusing the immediate post C-arm CT images with pre-treatment 3D DSA images using 3D/3D image registration.

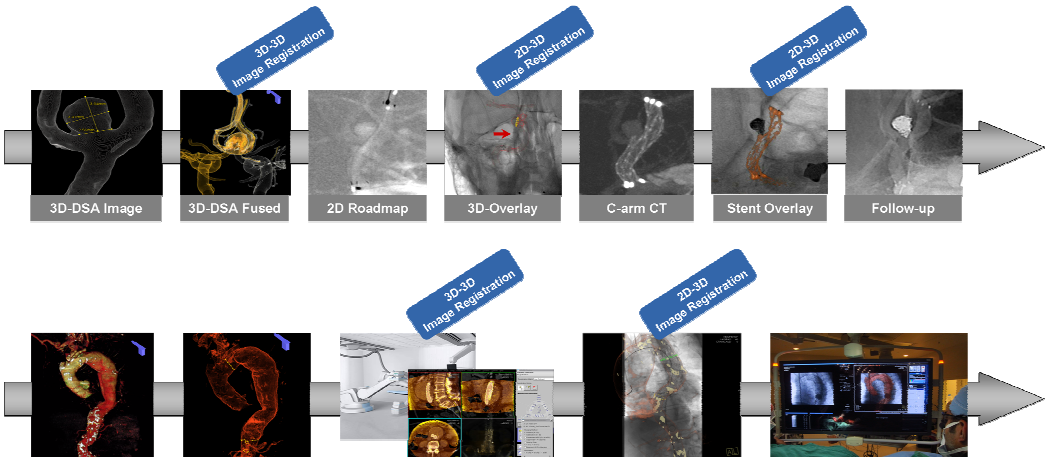

Fig. 2: Detailed workflow for computer assisted aneurysm treatment of intracranial aneurysms (top) and abdominal aortic aneurysms (bottom).

Compared to intracranial aneurysm treatment workflow, planning is always performed on pre-operative CT or MR images in abdominal aneurysm treatment procedure. The aneurysm is studied to determine the stent type and the near by vessels such as renal arteries, celiac and SMA arteries are marked so that care is taken during deployment to avoid occluding these arteries. The position of the nearby vessels determines the landing zone for the stent graft and hence they are carefully marked/annotated. This information can be overlaid onto the fluoroscopic screen either by a direct 2D/3D registration which registers the CT/MR images to two orthogonal X-ray images or through a 3D/3D registration followed by a 2D/3D registration. Using the later option, CT/MR images are initially registered to C-arm CT images and then overlaid onto the fluoroscopic images. Once overlaid, all annotations are available on the live fluroscopic screen during navigation and deployment.

3 Results

3.1 3D/3D Registration

Figures 3 and 4 show a few examples of 3D/3D rigid registration between pre-procedure CT images and intra-procedural C-arm CT images for aortic aneurysm treatment. Images are aligned by matching rib cage (bones), trachea, vascular anatomy if visible in C-arm CT images, and stent grafts themselves. Similar examples for intracranial aneurysms are shown in Figure 5.

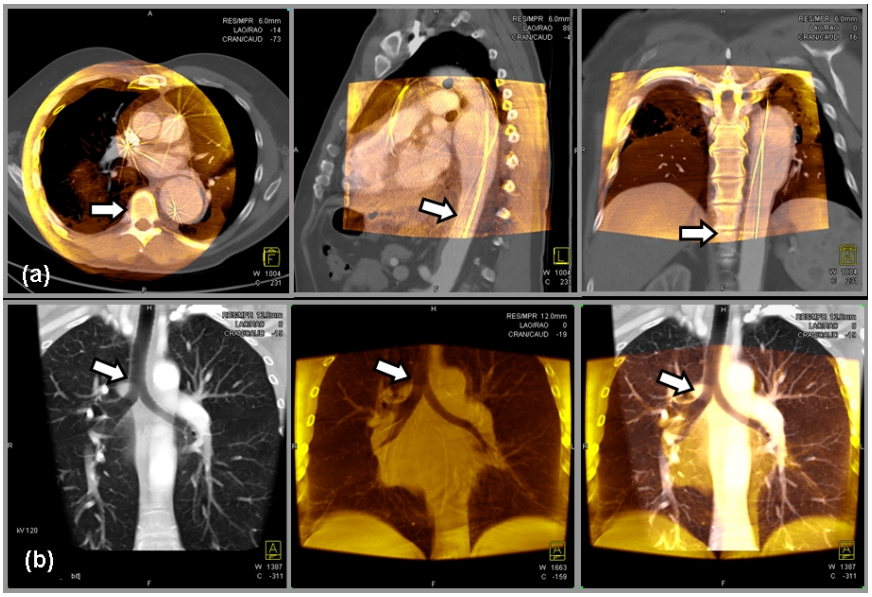

Fig. 3: Examples of 3D-3D rigid registration in endovascular treatment of aortic aneurysms: (a) Pre-procedural CT images are registered to intra-procedural non-contrast C-arm CT images by aligning bones and refined by using guidewire inside aorta(arrow). This is used to overlay planning information from CT to fluoro. This registration is error prone as aligning the bones does not always align the vessels and hence the refinement using guidewire. (b) Pre-procedural CT images are registered to intra-procedural non-contrast C-arm CT images by aligning trachea. This resulted in accurate alignment compared to aligning rib cages or other bony structures. Initial alignment is performed by matching bony structures, followed by manual adjustment to match the structures of interest

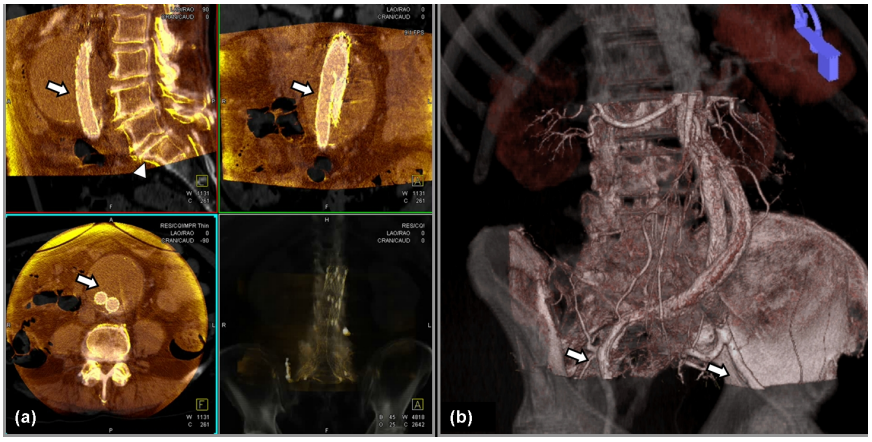

Fig. 4: Examples of 3D-3D rigid registration in endovascular treatment of aortic aneurysms: (a) Pre-procedural CT images are aligned to intra-procedural non-contrast C-arm CT images by aligning stent grafts in endoleak treatment procedures. Stent grafts provide good matching features as they are visible in both imaging modalities. Eventhough the bones could be misaligned (arrowhead) matching stent grafts (arrow) provide accurate alignment, (b) Pre-procedural CT images are aligned to intra-procedural contrast enhanced C-arm CT images by aligning vascular anatomy

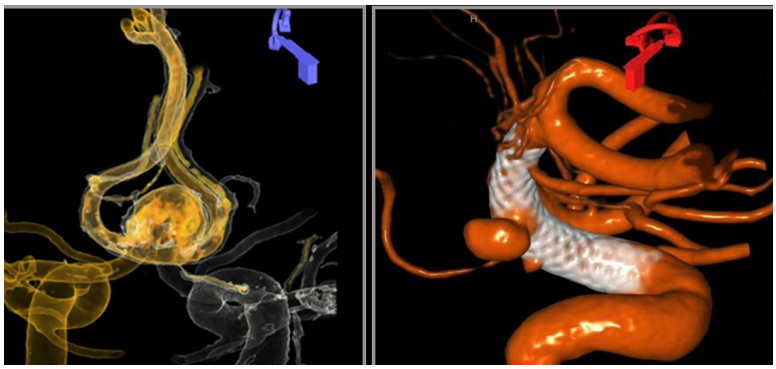

Fig. 5: Examples of 3D-3D registration in endovascular treatment of intracranial aneurysms: (a) 3D DSA images from left internal carotid artery and right internal carotid artery injections are aligned to understand the anatomy of aneurysm located on anterior communicating artery (AComm). Initial alignment is crucial in such applications as the 3D DSA image doesn't have any parenchymal or soft tissue information for the automatic registration to work, (b) Pre-treatment 3D DSA is aligned with immediate post treatment C-arm CT image of the deployed pipeline flow diverter device to understand the aneurysm neck coverage of the device. Images are aligned by matching skull bones and vasculature

3.2 2D/3D Registration

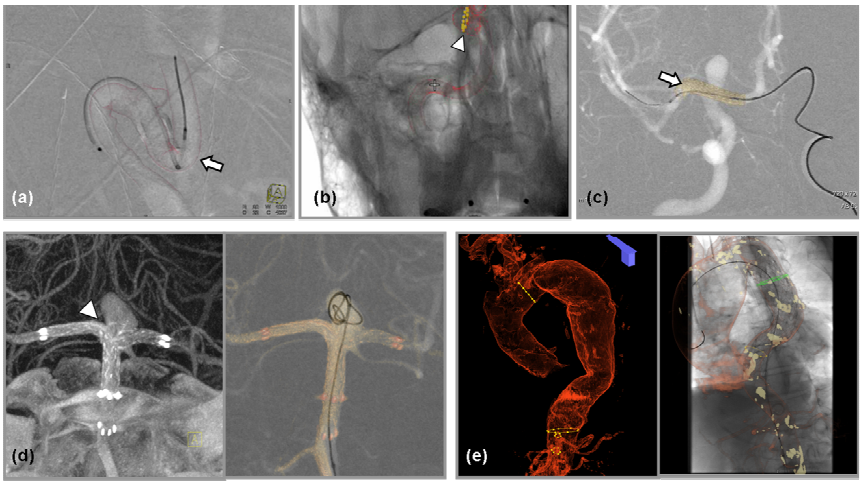

Fig. 6: Examples of 2D-3D registration in computer assisted endovascular treatment of intracranial and aortic aneurysms: (a) Vessel anatomy from 3D DSA images is overlaid on fluoroscopic images. New generation devices such as Pipeline® (eV3,Plymouth,MN) flow diverter devices are better visualized on native fluoro images compare to 2D DSA images. However, the native fluoro images do not show any vessel anatomy, there by losing the context of aneurysm and the parent vessel while deploying the device. This information can be derived from 3D roadmapping by overlaying vessel anatomy (arrow) from intra-procedural 3D DSA images, (b) Similar to (a), but manual annotations such as aneurysm neck (arrow-head), distal and proximal landing zones can be overlaid on fluoro for improved image guidance during device deployment, (c) virtual stent planning or simulation information is overlaid on fluoroscopic images for realtime image guidance during deployment, (d) Deployed stent is overlaid on fluoroscopic images for guidance in stent-assisted coiling procedures. Intra-procedural C-arm CT images are acquired immediately after deploying stent or flow diverter. The images are processed and segmented to extract the deployed device and overlaid on fluoroscopy images. Overlaying stent struts (arrow-head) on fluoroscopy images is helpful as the struts sometimes herniate into the aneurysm and it helps the physician optimally pack the coils so that there is no residual filling at neck of the aneurysm; (e) Aorta with calcifications and planned proximal and distal landing zones (yellow circles) for stent graft are overlaid on fluoroscopy images for image guided navigation and device deployment. The planning is performed on pre-procedural CT, fused with intra-procedural C-arm CT image and overlaid on fluoroscopy images

Figure 6 shows various clinical examples of 2D/3D registration to overlay planning from CT/MR images, pre-treatment C-arm CT images or 3D DSA images, along with implanted devices from intra-procedural C-arm CT images.

4 Discussion

Clinical adoption and routine utilization of any 3D image-guided navigation solution depends not only on the accuracy, but also on how well the solution is integrated into the current clinical workflow. Seamless integration of image acquisition, segmentation, registration, and visualization techniques is a critical pre-requisite for the success of any image-guided navigation solution. This paper illustrated the clinical workflow for computer assisted stent procedures and mainly focused on exploring the role of image registration during the treatment of intracranial and aortic aneurysms.

Image registration, both 3D/3D and 2D/3D, plays a key role in merging information at various stages of the treatment. In general, 3D image guidance during intra-cranial aneurysm treatment relies mainly on the intra-procedural C-arm CT imaging because of its superior quality with high spatial resolution that helps with visualizing high contrast objects such as vessels and intra-cranial devices (stents, coils). In contrast, 3D image guidance during aortic aneurysm treatment relies mainly on pre-procedural CT or MR images, while C-arm CT helps as a bridging modality to register the pre-procedural images to current C-arm coordinate system. Despite considerable research and enormous literature on image registration algorithms, 3D/3D image registration, even rigid, is seldom carried out on a routine clinical basis [2]. A typical interventional workflow may demand a fully automatic registration algorithm that can provide sub-millimeter accuracy within a reasonable computation time and has a large enough capture range. Most automatic registration algorithms are geared towards aligning bony structures and often do not necessarily align the object of interest, thus making it inapplicable during the procedure. In order to make these algorithms routinely applicable in clinical practice, intelligent context-specific image registration algorithms that align the organs of interest, known anatomical landmarks (eg. trachea, calcifications) or devices need to be developed.

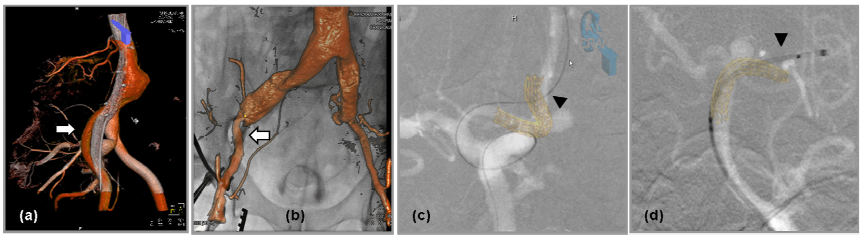

Fig. 7: (a,b) Examples from aortic aneurysm treatment procedure, showing deformation of iliac artery (arrow) due to the device delivery catheter system posing challenges with 3D-3D and 2D-3D registration, (c,d) Examples from intracranial aneurysm treatment procedure, showing deformation of intracranial vessels (arrow-head) due to guidewire and stent delivery catheter system

Overlaying information from 3D images onto live fluoroscopy (3D road-mapping technique) has evolved mainly for neuro-angiographic procedures, [4,6], attributed

to the fact that both 2D and 3D image data are obtained from the same C-arm system and are intrinsically aligned. One of the main advantages of 3D road-mapping over conventional 2D roadmap include dynamic integration of 3D information onto live fluoroscopy from any C-arm/table position or zoom without having to do multiple contrast injections. The current state-of-art 2D/3D registration in clinical practice involves fusing the pre-operative CT/MR with intra-procedural C-arm CT and then projecting on to the fluoroscopy images. This approach imposes additional intra-procedural imaging which increases the procedure time and radiation dose to the patient. Although, direct 2D/3D registration algorithms exist in literature, their clinical existence is limited due to workflow limitations and accuracy.

Moreover, there are additional challenges associated with overlaying 3D information onto 2D fluoroscopy. It is important to address the need for non-rigid registration that can recover misalignment due to different patient positioning between the scans, patient movement during the procedure and vessel deformation due to devices (guide wires and catheters) [1]. Figure 7 illustrates clinical examples of vessel deformation due to devices in the vessels during the procedure. There is a need to capture these deformations and update the 3D information that is being projected onto the fluoroscopy images. However, any non-rigid solution that is proposed brings in another level of complexity that needs careful clinical validation and consideration towards fidelity of data after applying the deformation.

Nevertheless, image-guided navigation and computer-assisted stenting is evolving towards routine clinical practice. Further refinements with anatomical context dependent image registration strategies that fit into the existing clinical workflow are required in the near future.

5 Acknowledgments

We would like to thank Dr. Michel Mawad from St. Luke's Episcopal Hospital, Houston , TX and Dr. Alan Lumsden, Dr. Jean Bismuth from Methodist DeBakey Heart and Vascular Center, Houston, TX for providing image data and evaluating the proposed computer assisted stenting workflow.

References

1. Carrell, T.W.G., Modarai, B., Brown, J.R.I., Penney, G.P.: Feasibility and limitations of an automated 2d-3d rigid image registration system for complex endovascular aortic procedures. Journal of Endovascular Therapy 17(4), 527–533 (2010)
2. Hill, D.L., Batchelor, P.G., Holden, M., Hawkes, D.J.: Medical image registration. Physics in Medicine and Biology 46, R1–R45 (2001)
3. Kamran, M., Nagaraja, S., Byrne, J.: C-arm flat detector computed tomography: the technique and its applications in interventional neuro-radiology. Neuroradiology 52, 319–327 (2010)
4. Kukuk, M., Napel, S.: Rotational roadmapping: a new image-based navigation technique for the interventional room. vol. 10(Pt 2), pp. 636–43 (2007)

5. Maintz, J., Viergever, M.A.: A survey of medical image registration. Medical Image Analysis 2(1), 1 – 36 (1998)
6. Ruijters, D., Homan, R., Mielekamp, P., van de Haar, P., Babic, D.: Validation of 3d multimodality roadmapping in interventional neuroradiology. Physics in Medicine and Biology 56(16), 5335 (2011)
7. Zitov, B., Flusser, J.: Image registration methods: a survey. Image and Vision Computing 21, 977–1000 (2003)

Computational Methods of Modeling Stent Deployment in the Coronary Artery

Nenad Filipovic[1,2*], Dalibor Nikolic[1], Zarko Milosevic[1], Exarchos Themis[3], Dimitris Fotiadis[3] and Oberdan Parodi[4]

[1]University of Kragujevac, Kragujevac, Serbia
{fica@kg.ac.rs}
[2]Harvard University, Boston, USA
{nfilipov@hsph.harvard.edu}
[3]University of Ioannina, Ioannina, Greece
[4] National Research Council Pisa, Italy

Abstract. Coronary artery stents are routinely used in the management of patients with angina or myocardial infarction where percutaneous coronary intervention is the clinically appropriate procedure. Stress inside the arterial wall and stress in the stent are very important biomechanical parameters. Insight into these biomechanical analyses may give better understanding of the process of restenosis.
Geometrical model for the coronary artery was reconstructed from combination of biplane angiography and intravascular ultrasound. In house finite element method computations were performed to simulate the deployment of a stent inside the reconstructed coronary model.
Fluid domain before and after stenting and stress distribution in the stent are studied. In the arterial wall the maximal effective stress are found behind the stent and in the regions where the arterial wall was thinner. Inside the stent the values of the maximal stress of 180 MPa were observed near the connecting parts.
Computer simulation can be used to predict stresses in the stent and the arterial vessel wall in order to make better optimal stent design for a specific patient.

Keywords: stenosis, stent deployment, computer modeling, biomechanical stresses

1 Introduction

Atherosclerosis is a progressive asymptomatic disease characterized by the narrowing and hardening of arteries that may result in eventual blockage causing ischemia to tissues and organs. Treatments for blocked coronary arteries include bypass surgery, angioplasty, and stenting. The stents may be expanded by the assistance of an angioplasty balloon catheter, or they may be self-expanding. A vascular stent is a small metal tube, which is inserted inside the artery and it has a role to reduce narrowing of the artery. A non-desirable process of restenosis is caused by neointimal hyperplasia. [1]. Available experimental studies clearly indicate the stent-artery mechanical interaction as one of the significative causes for the activation of restenosis mechanisms.
There are efforts for modeling and design of stents, as well as stent design affects restenosis [2-4]. Linear elastic models are used for modeling of balloon expansion with stent and artery contact using a 2- dimensional model by Rogers et al. [4]. Migliavacca and colleagues [5-7]

have modeled the characterization of mechanical properties of stents. Lally and colleagues [7] calculated the stent-artery interaction of commercially available stents on an idealized stenosed artery. Holzapfel et al. [9] modeled the balloon expansion of a full three-dimensional anisotropic diseased artery. There is no much study for patient specific geometry stent deployment.
In this study we investigate stent deployment in the specific patient geometry coronary artery with numerical method. Firstly we presented basic equations and finite element methodology for solving blood flow, nonlinear arterial wall and stent interaction with arterial wall. Some results for stress analysis of the arterial wall and stent are presented. Finally, computational results are discussed and summarized.

2 Methods

2.1 3D image reconstruction

The 3D reconstruction of an arterial tree for single case report using CTA images is implemented [10]. A single vessel reconstruction is provided from IVUS and Angiography [11-15]. Two end – diastolic angiographic images are used to predict the catheter path. The artery path is approximated with cubic B – Splines and the catheter path is evolved by the intersection of two splines. IVUS frames are collected at the peak of R wave and by using deformable models and Neural Networks the lumen and outer vessel border are identified [11].

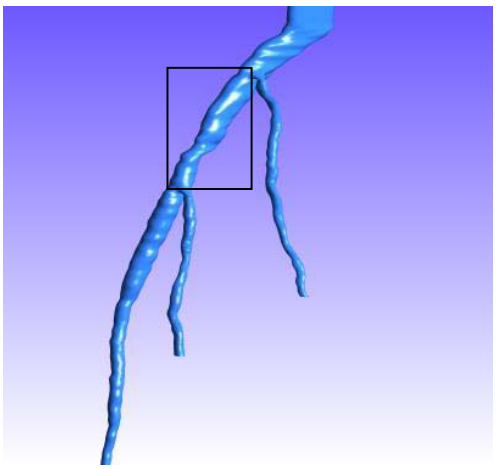

Fig. 1 Three-dimensional reconstructed model of an arterial tree. The location of the stenotic segment where stent was deployed

2.2 Methods of blood flow modeling in large blood vessels

The blood can be considered as an incompressible homogenous viscous fluid for flow in large blood vessels. Also, the laminar flow is dominant in physiological flow environment. Therefore, the fundamental laws of physics which include balance of mass and balance of linear momentum are applicable here. These laws are expressed by continuity equation and the Navier-Stokes equations.

We here present the final form of these equations to emphasize some specifics related to blood flow. The incremental-iterative balance equation of a finite element for a time step 'n' and equilibrium iteration 'i' has a form

$$\begin{bmatrix} \frac{1}{\Delta t}\mathbf{M} + {}^{n+1}\tilde{\mathbf{K}}_{vv}^{(i-1)} & \mathbf{K}_{vp} \\ \mathbf{K}_{vp}^{T} & \mathbf{0} \end{bmatrix} \begin{Bmatrix} \Delta\mathbf{V}^{(i)} \\ \Delta\mathbf{P}^{(i)} \end{Bmatrix}_{blood} = \begin{Bmatrix} {}^{n+1}\mathbf{F}_{ext}^{(i-1)} \\ 0 \end{Bmatrix} - \begin{bmatrix} \frac{1}{\Delta t}\mathbf{M} + {}^{n+1}\mathbf{K}^{(i-1)} & \mathbf{K}_{vp} \\ \mathbf{K}_{vp}^{T} & 0 \end{bmatrix} \begin{Bmatrix} {}^{n+1}\mathbf{V}^{(i-1)} \\ {}^{n+1}\mathbf{P}^{(i-1)} \end{Bmatrix} + \begin{Bmatrix} \frac{1}{\Delta t}\mathbf{M}\,{}^{n}\mathbf{V} \\ 0 \end{Bmatrix} \tag{1}$$

where ${}^{n+1}\mathbf{V}^{(i-1)}$ ${}^{n+1}\mathbf{P}^{(i-1)}$ are the nodal vectors of blood velocity and pressure, with the increments in time step $\Delta\mathbf{V}^{(i)}$ and $\Delta\mathbf{P}^{(i)}$ (the index 'blood' is used to emphasize that we are considering blood as the fluid); Δt is the time step size and the left upper indices 'n' and 'n+1' denote start and end of time step; and the matrices and vectors are defined in [16]. Note that the vector ${}^{n+1}\mathbf{F}_{ext}^{(i-1)}$ of external forces includes the volumetric and surface forces. In the assembling of these equations, the system of equations of the form (1) is obtained, with the volumetric external forces and the surface forces acting only on the fluid domain boundary (the surface forces among the internal element boundaries cancel).

The specifics for the blood flow are that the matrix ${}^{n+1}\mathbf{K}^{(i-1)}$ may include variability of the viscosity if non-Newtonian behavior of blood is considered. We have that

$$\left[K_{KJ}^{(i-1)}\right]_{mk} = \left[\hat{K}_{KJ}^{(i-1)}\right]_{mk} + \int_{V} \mu^{(i-1)} N_{K,j} N_{J,j}\, dV \tag{2}$$

where $\mu^{(i-1)}$ corresponds to the constitutive law for the last known conditions (at iteration '$i-1$'). In case of use of the Cason relation (2), the second invariant of the strain rate $D_{II}^{(i-1)}$ is to be evaluated when computing $\mu^{(i-1)}$.

The penalty method is used in order to reduce pressure unknown per node, as well as the ALE formulation for large displacements of blood vessel walls [17].

In addition to the velocity and pressure fields of the blood, the distribution of stresses within the blood can be evaluated. The stresses ${}^{t}\sigma_{ij}$ at time 't' follow from

$${}^{t}\sigma_{ij} = -{}^{t}p\,\delta_{ij} + {}^{t}\sigma_{ij}^{\mu} \tag{3}$$

where

$${}^{t}\sigma_{ij}^{\mu} = {}^{t}\mu\left(v_{i,j} + v_{j,i}\right) \tag{4}$$

is the viscous stress. Here, ${}^{t}\mu$ is viscosity corresponding to the velocity vector ${}^{t}\mathbf{v}$ at a spatial point within the blood domain. The field of the viscous stresses is given by (4).

Further, the wall shear stress at the blood vessel wall is calculated as:

$${}^{t}\tau = {}^{t}\mu\frac{\partial\, {}^{t}v_{t}}{\partial n} \tag{5}$$

where ${}^{t}v_t$ denotes the tangential velocity, and n is the normal direction at the vessel wall. Practically, we first calculate the tangential velocity at the integration points near the wall surface, and then numerically evaluate the velocity gradient $\partial {}^{t}v_t / \partial n$; finally, we determine the viscosity coefficient ${}^{t}\mu$ using the average velocity at these integration points. In essence, the wall shear stress is proportional to the shear rate γ at the wall, and the blood dynamic viscosity μ.

For a pulsatile flow the mean wall shear stress within a time interval T can be calculated as [18]

$$ {}^{T}\tau_{mean} = \left| \frac{1}{T} \int_0^T {}^{t}\tau_n dt \right| \tag{6} $$

Another scalar quantity is a time-averaged magnitude of the surface traction vector, calculated as

$$ {}^{T}\tau_{mag} = \frac{1}{T} \int_0^T \left| {}^{t}\mathbf{t} \right| dt \tag{7} $$

where the vector ${}^{t}\mathbf{t}$ is given by the Cauchy formula.

2.3 Modeling the deformation of blood vessels

Blood vessel tissue has complex mechanical characteristics. The tissue can be modeled by using various material models, from linear elastic to nonlinear viscoelastic. We here summarize the governing finite element equations used in modeling wall tissue deformation with emphasis on implementation of nonlinear constitutive models.

The finite element equation of balance of linear momentum is derived from the fundamental differential equations of balance of forces acting at an elementary material volume. In dynamic analysis we include the inertial forces in this equation according to. Then, by applying the principle of virtual work

$$ \mathbf{M}\ddot{\mathbf{U}} + \mathbf{B}^{w}\dot{\mathbf{U}} + \mathbf{K}\mathbf{U} = \mathbf{F}^{ext} \tag{8} $$

Here the element matrices are: $\mathbf{M}$ is mass matrix; $\mathbf{B}^{w}$ is the damping matrix, in case when the material has a viscous resistance; $\mathbf{K}$ is the stiffness matrix; and $\mathbf{F}^{ext}$ is the external nodal force vector which includes body and surface forces acting on the element. By the standard assembling procedure, the dynamic differential equations of motion are obtained. These differential equations can further be integrated in a way described, with a selected time step size Δt. The nodal displacements ${}^{n+1}\mathbf{U}$ at end of time step are finally obtained according to equation:

$$ \hat{\mathbf{K}}_{tissue}\, {}^{n+1}\mathbf{U} = {}^{n+1}\hat{\mathbf{F}} \tag{9} $$

where the tissue stiffness matrix $\hat{\mathbf{K}}_{tissue}$ and vector ${}^{n+1}\hat{\mathbf{F}}$ are expressed in terms of the matrices and vector in (8). Note that this equation is obtained under the assumption that the problem is linear: displacements are small, the viscous resistance is constant, and the material is linear elastic.

In many circumstances of blood flow the wall displacements can be large, as in case of aneurism or hart, hence the problem becomes geometrically nonlinear. Also, the tissues of blood vessels have nonlinear constitutive laws, leading to materially-nonlinear FE formulation. Therefore, the approximations adopted to obtain equation (9) may not be appropriate. For a nonlinear problem, instead of (9) we have the incremental-iterative equation

$$ {}^{n+1}\hat{\mathbf{K}}_{tissue}^{(i-1)}\,\Delta\mathbf{U}^{(i)} = {}^{n+1}\hat{\mathbf{F}}^{(i-1)} - {}^{n+1}\mathbf{F}^{\mathrm{int}(i-1)} \tag{10} $$

where $\Delta\mathbf{U}^{(i)}$ are the nodal displacement increments for the iteration 'i', and the system matrix ${}^{n+1}\hat{\mathbf{K}}_{tissue}^{(i-1)}$, the force vector ${}^{n+1}\hat{\mathbf{F}}^{(i-1)}$ and the vector of internal forces ${}^{n+1}\mathbf{F}^{\mathrm{int}(i-1)}$ correspond to the previous iteration.

We here emphasize the material nonlinearity of blood vessels which is used in further applications. As presented, the geometrically linear part of the stiffness matrix, $\left({}^{n+1}\mathbf{K}_L\right)_{tissue}^{(i-1)}$, and nodal force vector, ${}^{n+1}\mathbf{F}^{\mathrm{int}(i-1)}$, are defined in equation:

$$ \left({}^{n+1}\mathbf{K}_L\right)_{tissue}^{(i-1)} = \int_V \mathbf{B}_L^T\,{}^{n+1}\mathbf{C}_{tissue}^{(i-1)}\,\mathbf{B}_L\,dV, \quad \left({}^{n+1}\mathbf{F}^{\mathrm{int}}\right)^{(i-1)} = \int_V \mathbf{B}_L^T\,{}^{n+1}\boldsymbol{\sigma}^{(i-1)}\,dV \tag{11} $$

where the consistent tangent constitutive matrix ${}^{n+1}\mathbf{C}_{tissue}^{(i-1)}$ of tissue and the stresses at the end of time step ${}^{n+1}\boldsymbol{\sigma}^{(i-1)}$ depend on the material model used. Calculation of the matrix ${}^{n+1}\mathbf{C}_{tissue}^{(i-1)}$ and the stresses ${}^{n+1}\boldsymbol{\sigma}^{(i-1)}$ for the tissue material models used in further applications. In each of the subsequent sections we will give the basic data about the models used in the analysis.

3 Results

In order to perform computer modeling of the combined effects of the surrounding arterial wall and inner forces of blood and stent deployment against the arterial wall, a 3D reconstruction from IVUS and angiography was derived.

The FE model consists of the solid domain and the fluid domain (Fig. 1). The solid domain consists of: stent and arterial wall. Fluid and solid domains are modeled using 3D-8-node finite elements.

Boundary conditions for the solid surrounding the artery are as follows. It is assumed that the first and last cross-sections do not move axially, hence all FE element nodes in these cross-sections are axially restrained.

It is also assumed that the wall material is orthotropic nonlinear elastic, and the Fung material model is adopted [19]. The strain energy function is defined. The material parameters c, a_1, a_2, a_4 are determined using data fitting procedure from [16]. Material parameters obtained from the fitting procedure are:

$$ c = 0.7565\ \left[MPa\right],\ a_1 = 0.166,\ a_2 = 0.084,\ a_4 = 0.045 \tag{12} $$

For the stent material, the alloy of Nitinol is adopted (for the definition of this material. Material parameters characterizing this alloy are [20]:

$$ \begin{aligned} &E = 60000\ \left[MPa\right] && \nu = 0.3 \\ &\sigma_s^{AS} = 520 && \sigma_f^{AS} = 750 && \sigma_s^{SA} = 550 && \sigma_f^{SA} = 200 \\ &\beta^{AS} = 250 && \beta^{SA} = 20 && \varepsilon_L = 7.5\% && C = 0\ \left[MPa/K\right] \end{aligned} \tag{13} $$

where all σ - and β -parameters are in [*MPa*]. Material parameters of blood are: density $\rho = 1.05 \cdot 10^{-3} \left[g / mm^3 \right]$ and dynamic viscosity $\mu = 3.675 \cdot 10^{-3} \left[Pa \cdot s \right]$.

According to the boundary conditions and loads mentioned above, the numerical analysis of the material behavior of this complex model is performed. To examine different loading conditions, we apply hemodynamic flow as well as stent deployment procedure at the arterial wall. Post deployment geometry was obtained by finite element simulation.

The stent is loaded by an internal uniform radial pressure linearly varies from zero to 1 MPa. Due to the artery incompressibility requirement and to avoid locking-problems, 8-node brick elements are used in all the analyses [16]. In particular, in the simulations we use up to 232214 elements and 257532 nodes, resulting in 666354 variables. The interaction between the expanding stent and the artery is described as contact between deformable surfaces. As contact conditions, we set finite sliding, no-friction, with the constraint enforced by a Lagrange multiplier method. The stenotic segment of the artery which was examined before and after stent deployment is presented in Fig. 2.

a) b)

Fig. 2 Stent positioning before (a) and after (b) stent deployment

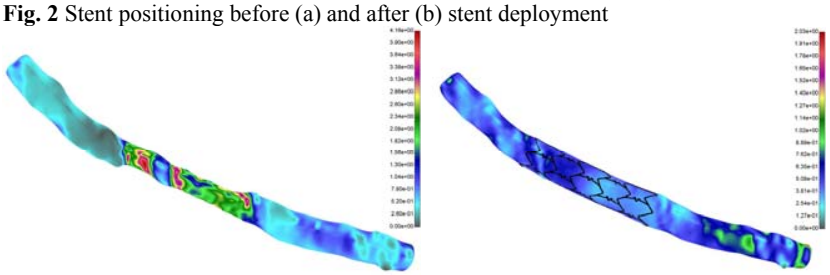

a) b)

Fig. 3 Shear stress distribution for pre (a) and after stent deployment (b). The units are in Pa.Blood flow analysis was performed by finite element method described in the methods section. Shear stress distribution before and after stent deployment is shown in Fig. 3. It can be seen that stent reduce wall shear stress significantly after deployment which is caused by opening the artery and reducing the narrowing.

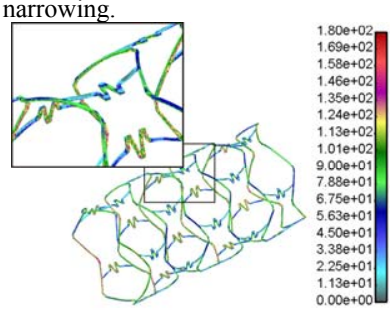

Fig. 4 Effective von Mises stress distribution for inflation pressure of 1 MPa. The units are in MPa

The effective von Mises stress distribution in the stent is presented in Fig. 4. It can be observed that highest stresses are located near the connectors between the stent struts. These parts are subjected to plastic deformation with maximal stress around 180 MPa.

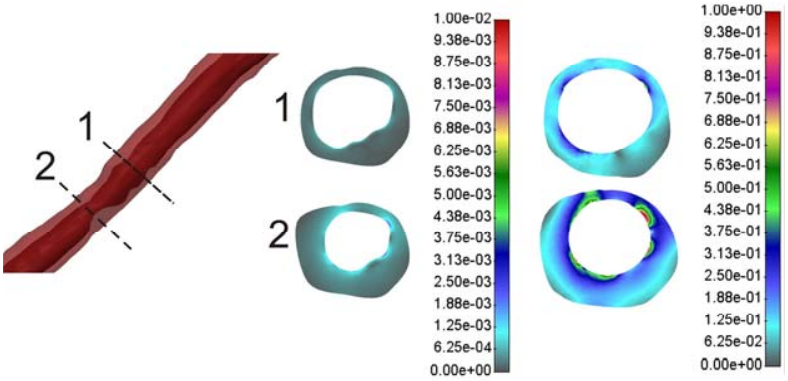

Fig. 5. Effective stress distribution in the two different cross-section locations inside the arterial wall at the end of stent deployment

The effective stress distribution in the arterial wall at the two different cross-section locations at the end of stent deployment with maximum deployment pressure is shown in Fig. 5. It can be observed that higher stress exists when wall thickness is reduced during deployment procedure.

4 Discussion and conclusion

In this study stresses inside the arterial wall as well as stent during stent deployment procedure is investigated. Three-dimensional reconstruction of coronary artery is obtained by CTA and combination of IVUS and Angiography. Finite element formulation for blood flow analysis, a nonlinear wall artery and stent deformation and contact problem is implemented. Stress distribution of the artery wall and stent during expansion of occluded zones is analyzed. The maximal effective stress are found behind the stent and in the regions where the arterial wall was thinner. This is probably due to reduced volume distribution in these zones. Also shear stress distribution before and after stent deployment is compared. From the comparison with the preoperative situation it is possible to observe how the stent pushes the arterial wall towards the outside allowing the expansion of the occluded artery.

Better understand of stent deployment procedure and arterial wall response as well as optimal stent design can be obtained using computer simulation.

Acknowledgments

This study was funded by a grant from FP7-ICT-2007 project (grant agreement 224297, ARTreat) and grants from Serbian Ministry of Education and Science III41007 and ON174028.

References

[1] Edelman E.R., Rogers C: Pathobiologic responses to stenting. Am J Cardiol, 81(7A), 4E-6E, (1998)

[2] Kastrati, A., Mehilli, J., Dirschinger, J., Pache, J., Ulm, K., Schuhlen, H., Seyfarth, M., Schmitt, C., Blasini, R., Neumann, F.J., Schomig, A.: Restenosis after coronary placement of various stent types. The American Journal of Cardiology, 87, 34-39 (2001)

[3] Rogers, C., Edelman, E. R.: Endovascular stent design dictates experimental restenosis and thrombosis. Circulation 91, 2995-3001 (1995)
[4] Rogers, C., Tseng, D.Y., Squire, J.C., Edelman, E.R.: Balloon-artery interactions during stent placement: a finite element analysis approach to pressure, compliance, and stent design as contributors to vascular injury. Circulation Research 84, 378-383 (1999)
[5] Petrini, L., Migliavacca, F., Auricchio, F., Dubini, G.:Numerical investigation of the intravascular coronary stent flexibility. Journal of Biomechanics 37, 495-501 (2004)
[6] Migliavacca, F., Petrini, L., Colombo, M., Auricchio, F., Pietrabissa, R.:Mechanical behavior of coronary stents investigated through the finite element method. Journal of Biomechanics 35, 803-811 (2002)
[7] Migliavacca, F., Petrini, L., Montanari, V., Quagliana, I., Auricchio, F., Dubini, G., 2005. A predictive study of the mechanical behaviour of coronary stents by computer modelling. Medical Engineering and Physics 27, 13-18 (2005)
[8] Lally, C., Dolan, F., Prendergast, P.J.: Cardiovascular stent design and vessel stresses: a finite element analysis. Journal of Biomechanics 38, 1574-1581 (2005)
[9] Holzapfel, G. A., Sommer, G., Regitnig, P.: Anisotropic mechanical properties of tissue components in human atherosclerotic plaques. Journal of Biomechanical Engineering 126, 657-665 (2004)
[10] Parodi O., Exarchos T., Marraccini P., Vozzi F., Milosevic Z., Nikolic D., Sakellarios A., Siogkas P., Fotiadis D., Filipovic N.: Patient-specific prediction of coronary plaque growth from CTA angiography: a multiscale model for plaque formation and progression, IEEE Trans Inf Technol Biomed. (in press) (2012)
[11] Plissiti, M., Fotiadis, D., Michalis, L., Bozios, G.: An Automated Method for Lumen and Media-Adventitia Border Detection in a Sequence of IVUS Frames, IEEE trans on Inf Tech. in Biomed, 8, 131-141. (2004)
[12] Papadogiorkaki, M., Chatzizisis, Y.: Automated IVUS Contour Detection usingIntensity Features and Radial Basis Function Approximation, IEEE International Symposium on Computer Based Medical Systems. (2007)
[13] Wahle, A,, Prause, G., Dejong, S., Sonka, M.: Geometrically correct 3-D reconstruction of intravascular ultrasound images by fusion with biplane angiography – methods and validation," IEEE Trans Med Imaging, 18, 686-98 (1999)
[14] Laban, M., Oomen, J., Slager, C., Wentzel, J., Krams, R., Schuurbiens, J.:ANGUS: a New Approach to Three-Dimensional Reconstruction of Coronary Vessels by Combined Use of Angiography and Intravascular Ultrasound, In: Proc. conf. CinC Vienna. (1995)
[15] Slager, C., Wentzel, J., Schuurbiers, J., Oomen, J., Kloet, J., Krams, R.: True 3-Dimentional Reconstruction of Coronary Arteries in Patients by Fusion of Angiography and IVUS (ANGUS) and its Quantitive Validation" Circulation, 102, 511-6 (2000)
[16] Kojic M., Filipovic N., Stojanovic B., Kojic N.: Computer Modeling in Bioengineering: Theoretical Background, Examples and Software. John Wiley and Sons, Chichester, England (2008)
[17] Filipovic N., Mijailovic S., Tsuda A., Kojic M.: An Implicit Algorithm Within The Arbitrary Lagrangian-Eulerian Formulation for Solving Incompressible Fluid Flow With Large Boundary Motions, Comp. Meth. Appl. Mech. Engrg., 195, 6347-6361 (2006)
[18] Taylor C.A., Hughes T.J.R., Zarins C.K.:Finite element modeling of blood flow in arteries, Comp. Meth. Appl. Mech. Engrg., 158, 155-196. (1998)
[19] Fung, Y.C., Fronek K., Patitucci P., Pseudoelasticity of arteries and the choice of its mathematical expression, Am. J. Physiol., 237, 620-631 (1979)
[20] Auricchio F., Taylor R.: Shape-memory alloys: modelling and numerical simulations of the finite-strain superelastic behavior, Comp. Meth. Appl. Mech. Engrg., 143, 175-194 (1997)

Stent Strut Detection by Classifying a Wide Set of IVUS Features

Rui Hua[1] *, Oriol Pujol[1], Francesco Ciompi[1], Simone Balocco[1], Marina Alberti[1], Fina Mauri[2], and Petia Radeva[1]

[1]Universitat de Barcelona, Barcelona, Spain
[2]Hospital Germans Trias i Pujol, Badalona, Spain

Abstract. Stent placement is a well-established clinical routine for treating coronary diseases due to its safety and minimal invasive surgery. In this paper, an automatic method for stent struct detection in Intravascular Ultrasound (IVUS) images is proposed based on a novel framework, which combines local and contextual information of strut appearance. In the first stage, local features are extracted from a wide filter base and used in a pixel-wise classification aimed at detecting candidate pixels belonging to stent struts. Since the appearance of the contextual surrounding structures is critical to remove artifacts with similar local appearance to struts, the former detection map is refined by using contextual features from the image patch centered at the candidate pixel.The proposed algorithm has been widely tested on 273 images of 12 pullbacks achieving encouraging results.

Keywords: IVUS analysis, stent strut detection, feature extraction

1 Introduction

Atherosclerosis is a hazardous disease, in which arterial wall hardens and thickens. A routine treatment for this kind of coronary artery disease is stent placement, which can re-dilate the artery with minimal invasive surgery. However, this technique also carries considerable potential risk due to underexpansion or malaposition of the stent, which can increase the risk of restenosis and thrombosis. IVUS is a catheter-based technique, which allows to visualize the result of stent vessel placement as well as to detect underexpansion and malaposition. Due to the large amount of data acquired during an IVUS pullback, manual analysis of stent positioning is difficult and time-consuming. Therefore, an automatic method for stent strut detection in IVUS images is on demand to speed up this analysis and reduce the subjectivity of manual segmentation [4].

Despite of the high clinical interest, surprisingly, only very little research on automatic analysis of stent implantation in IVUS can be found in the literature. Cañero et al. [1] proposed a technique to visualize and quantify the

* This work has been supported in part by the projects TIN2009-14404-C02 and CONSOLIDER-INGENIO CSD 2007-00018. We specially thank to Juan Rigla from BSCI for the valuable help and support.

mutual position between the stent and the vessel wall in IVUS pullbacks. Two deformable generalized cylinders, corresponding to the vessel wall and the stent, were adapted to image features in the IVUS sequence in order to obtain a 3D reconstruction of the stent and vessel borders. This algorithm showed its potential of detecting stent border, but it has only been qualitatively validated. Dijkstra et al. [4] proposed a stent contour detection algorithm. Firstly, a rough detection was performed to detect stent border based on brightness information. Then, two different model-guide optimizations were carried out to optimize the results. An improved method was proposed by the same authors [5], in which the local stent contour was adjusted using the information of the whole 3D model. This technique demonstrated its capability of detecting stent boundaries, however, it requires manual correction and images of good quality. A method for automatic detection of bio-absorbable coronary stent was proposed by Rotger et al. [8]. In this work, a cascade of classifiers was employed based on Haar-like features, which were selected to take advantage of the special appearance of polymer stent in IVUS images. This method is specialized on biodegradable struts and metallic struts are not considered by the authors.

In this paper, an automatic method is proposed to detect stent struts in 2D IVUS frames. The proposed detection method is mainly based on extraction of a wide set of IVUS features and applying machine learning techniques, due to the large amount of variation of the appearance of stents and complexity of IVUS images. The detection framework consists of two main stages. Firstly, pixel-wise descriptors are constructed and classified to detect potential strut candidates. This step is capable to locate almost all the struts, while still allowing some false positives (FPs). Secondly, these strut candidates are represented in a feature space using higher order contextual information by means of patch-based descriptors. Thus, stent struts are detected according to the morphological structures that surround them. Finally, the detection windows are merged to obtain an accurate strut location. We validate our method on 12 patients dataset of different clinical situations (underexpanded or malaposed stents, etc.) extracting several statistical measures like precision, sensitivity and F-measure to analyse the performance of the method.

2 Method

The pipeline of our method for automatic stent strut detection is shown in Fig.1.

2.1 Pixel-Based Classification

Stent struts appear in IVUS images as thin strips, which are bright and close to lumen, as shown in Fig.1 (a). Considering the intensity and shape characteristics of stent struts, several features have been specially chosen for the detection task. The intensity properties of stent struts are captured using: its intensity, the maximum, mean intensity and standard deviation of its neighbourhood. Besides, ridges are good at detecting connected regions of high intensities [1].

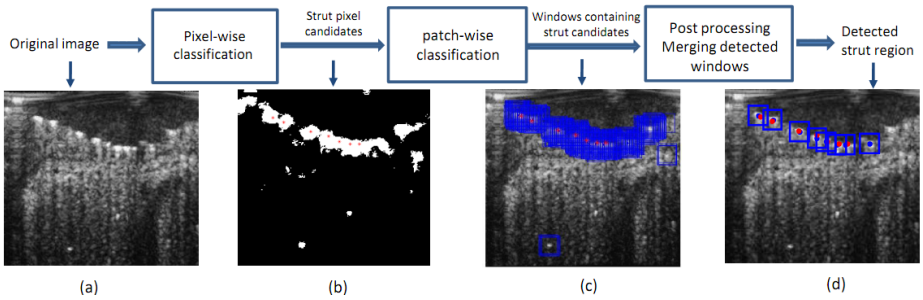

Fig. 1: Pipeline of the algorithm: (a) original image in polar system; (b) First strut detection map (c) Detected windows (blue) containing strut candidates; (d) Final detection windows in blue with their centers (blue dots) and ground truth (red dots).

In addition, the texture information of the image can be captured by 20 Gabor filters at different scales and orientations [2]. Furthermore, the shape of the struts is represented by a blob detector [6], which is a circularly symmetric Laplacian of Gaussian operator producing a high response at the center of image region with a blob shape. In summary, 36 local features are obtained to describe strut pixels.

Once defined the descriptor of strut centers, we proceed with a classification task to decide whether a pixel belongs to a strut. Adaboost with Decision Stumps is applied to the pixel-wise descriptors as one of the optimal classifiers to detect objects in images [9]. Moreover, it is capable of managing to learn from a large amount of data and features.

2.2 Patch-Based Classification

The first step produces potential strut candidates that represent a rough approximation of struts location. Since no contextual information has been exploited, the detection of false positives in regions characterized by high intensities and rounded shape is expected. In order to reduce FPs, a patch-based classification is defined, since the neighbourhood of stent struts provides a very diverse information to decide the presence of struts. Hence, we exploit the information of the local context around the strut candidates. For this purpose, a squared window of size (24×24) pixels is considered at each candidate pixel and a set of contextual features are extracted from each patch, as we estimated empirically that a window of (10×16) pixels (corresponding to (0.2×0.32) mm in polar coordinates) is enough to contain a strut. For each patch, three main operators are applied to extract features, namely Histogram of Oriented Gradients (HoG), Local Binary Patterns (LBP) and Steerable Filters (SF).

HoG is selected as a very characteristic descriptor, as it can capture the local appearance and shape of struts using the histogram of local gradient of different angles [3]. The edge structure related to image gradient can well characterize

local shape, as well as it is translation and intensity invariant. In this work, an image patch is divided into 3×3 overlapping cells and 9 orientation bins are used in the histogram as the optimal number of orientation bins for performance and computation cost [3]. LBP is another efficient texture descriptor, based on a binary comparison of the intensities of the center pixel and its neighbourhood. In this work, it is applied at the center of the image patch at 3 scales (circular neighbourhoods of radius of 1,2,3 pixels) and a rotationally invariant histogram is constructed for each of them achieving the property of being invariant to scale and rotation [7]. SF is used to highlight the strut regions. The image patch after filtering is divided into 9 parts, for each of which the mean and standard deviation are computed. Finally, the maximum intensity of the patch and the value of the distance with respect to the catheter are also included as additional features. A feature vector of length of 706 elements was extracted for each patch.

Adaboost with decision stumps is, again, chosen as the classifier to solve the binary classification problem to decide whether each detected window contains a struct or not.

2.3 Training Strategy

In order to train the pixel-wise classifier, a ground truth map needs to be generated to indicate which pixels belong to struts. As for this project only the center position of every strut is provided, the average size of the struts is measured by using an average template, which is calculated by taking a window of (36×36) pixels around every ground truth point and computing the average intensity of these windows.In order to select the real mean size of the struts, pixels with an intensity value lower than the 50% of the highest intensity are removed. However, the image contains a bright region below the center due to some mala-posed struts, therefore, as struts regions are symmetrical, the height is selected as twice the distance from the center to the uppermost point, achieving a size of (10×16) pixels. To ensure all the positive samples are taken from strut regions, a window (4×4) pixels is used instead. Negative samples are selected from outside the (10×16) window and pixels between these two windows are not considered for the training step.

2.4 Window Merging

The detection windows should be merged to reduce multiple candidates yield by the patch-wise classification. First of all, a window density image is generated by summing up the window number over each pixel in the image, as shown in Fig 2 (a). As stent struts often appear brighter than their neighbors, a combined density map is defined: $C = P \times I^3$, where $\times$ represents the pixel-wise product, P is the window density image, I is the image intensity. The regions with the highest response in the combined map are separated to locate precisely each strut, as shown in Fig.2. The result is further processed by removing very small regions and those, whose radius distance is further than 3/4 of the height of the image, taking into account the stent context in the IVUS image.

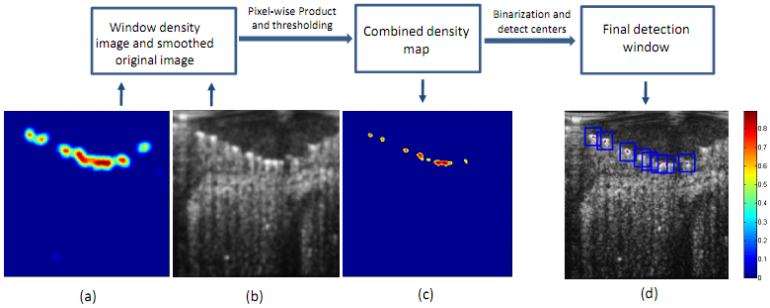

Fig. 2: Pipeline of window merging procedure: (a) Window density image; (b) Original image smoothed by a Gaussian; (c) Combined density map; (d) Final detection windows. (Red points are ground truth; Blue points are detected strut centers and blue windows are the final detection windows.)

3 Experimental Results

We validate our stent strut detection algorithm on 273 IVUS images from 12 pullbacks, in an average of 23 frames per pullback. These images contain stents from various companies, such as Skylor, Coroflex, and so on. All the images were acquired with Boston Scientific iLab IVUS Imaging System. In order to obtain a dataset of a large variability and of reasonable size, only around 23 representative frames are selected for each patient, considering the similarity of adjacent frames of one patient. As there is special clinical interest on under-expansion and mala-position, we have selected a challenging dataset, in which all the patients have under-expansion or mala-position to different degree and some patients have serious calcification. The ground truth was made by manually labelling the center of struts with a point by two physicians at Hospital Germans Trias i Pujol in Spain. Moreover, only the struts identified with high confidence were marked.

3.1 Evaluation methodology

In order to evaluate the detection result quantitatively, two measurements are computed. First, precision and sensitivity curves are given. Second, the average and standard deviation of the distance from a detected stent strut center to the ground truth center is reported. To decide whether a strut marked in the ground truth is correctly detected, for each detected strut center, we construct a square window of 10×16 pixels around it: if the ground truth point is inside the window, it is considered as a true positive (TP), otherwise it is considered as a FP. In order to compared our method with previous work, we also compute the F measure using precision and sensitivity, $F = PS/(P+S)$ [8].

Due to the large amount of data, the 12 patients were separated into 4 exclusive sets and cross validation has been applied on them. Given that 4-fold cross-validation 'leaving three patients out' is used to obtain the average score. Results

are expected to provide a lower bound on the performance of the methodology on new patients.

3.2 Results

The first quantitative analysis of the performance of the method is shown by the curve of precision and sensitivity of each patient varying with respect to the threshold of the combined window detection density map, as shown in Fig.3. The average equal precision and sensitivity, which is the crossing point between the two curves, is reached at 66% with an average threshold of 0.17.

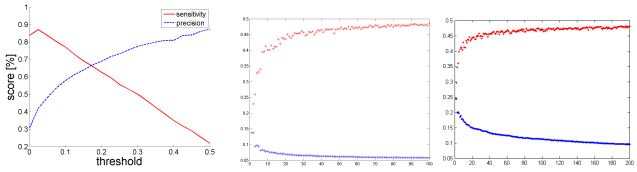

(a) (b) (c)

Fig. 3: (a) Curve of sensitivity (red) and precision (blue) varying with respect to the threshold of the combined map, averaged by the 4 folds of the cross validation. (b) Training error of Adaboost, strong classifier (red dots) and all the weak ones (blue dots), in the first classification. (c) Training error of Adaboost in the second classification.

In order to further measure the quality of the accuracy of the detection, the distance from the center of the detected struts to the ground truth was calculated. The average Euclidean distance is 2.18 pixels (0.04 mm) with a variance of 1.72 pixel (0.03 mm). Note that the average size of the stent struts is around 10×16 pixels, thus, our detection is extremely close to the ground truth.

Qualitative results are depicted in Fig. 4, where both the ground truth points and the results of the detection algorithm are shown. Most of the stent struts are correctly detected and the detections are very close to the ground truth points. Even, some of them can be argued to be more accurate, as they are closer to the real center of the strut than the ground truth points are. However, there remain some FPs. FPs usually corresponding to small calcified regions near the lumen border which have very similar appearance to stent struts. Additionally, we should note that physicians only annotated struts that they are completely confident about their presence. This causes some candidate struts (see Fig. 4(g)) to be considered as arguably false positives, worsening the overall performance. Missing struts mainly come from regions resembling fibrotic tissue. Fig. 4(h) shows an example of a malaposed strut that has been missed by the algorithm and can only be detected by considering the whole stent configuration.

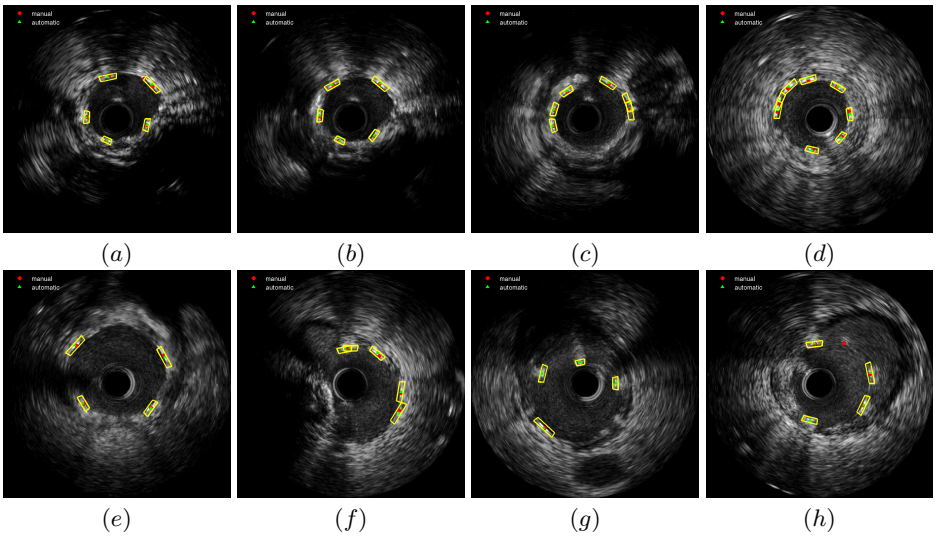

Fig. 4: Results of the automatic struts detection: The red points shows the ground truth; The green points present the detected strut centers and the yellow windows are the final detection windows

4 Discussions

In this work Adaboost was used with Decision Stumps as a reference classifier. The iteration limit in the first classification step is set to be 72, with which the error of Adaboost goes to less than 5%, as shown in Fig. 3 (a). This step ensures that nearly all positive samples are correctly detected but more than 90% of the whole set of pixels are removed. The second classifier focuses on the remaining candidate pixel set and describes the patches centred at them in order to capture the contextual appearance. This results in a 706-element feature vector. The second classifier converged at around 10% error rate Fig. 3 (b).

It is important to mention that in this dataset all the patients contain malaposition and some of them also have under-expansion. Images of patients with malaposition are challenging, since they have low intensities and they are not connected to the lumen, which may create a special shadow, different from normal struts.

5 Conclusions and Future Work

In this work, a novel method of stent strut detection is proposed, which integrates three steps: pixel-based local classification, patch-based feature extraction for contextual local appearance description and classification and, finally, a detection fusion step. The methodology is tested on a challenging dataset including

normal and malapposed stent struts. It is worth noting that malapposed stent struts have a different appearance from well-posed ones. This method is capable to detect struts with equal precision and sensitivity at 66% and an average pixel error of 2.18 pixels. In this paper we propose to validate the struts detection on 2D IVUS images without using any information of media, lumen or the whole pullback. Unfortunately there is no information in the literature on the performance of other methods working under the same conditions to compare with. Naturally, using global context like lumen and media as used by Rotger et.al. [8] or information from the whole pullback as used by Dijkstra et.al. [4] will additionally improve the results.

As discussed in the results section, there are some missing struts difficult to detect locally. Thus, one of the future lines is to include global morphological context information in order to disambiguate those cases. Additionally, very small calcified deposits on the lumen border resemble single stent struts need to be well handled. One of the main problems in assessing the results of the proposed method with respect to the state-of-the-art literature is the lack of a common database and methodology for automatic method validation. Different IVUS equipments and catheter specifications result in completely different problems. We plan to contribute in the future in constructing such a public database and well accepted validation methodology.

References

1. C. Canero, O. Pujol, and P. Radeva. et.al. Three-dimensional evaluation of the mutual position of stent and vessel via intracoronary ecography. In *Computer in Cardiology*, pages 265–268, 1999.
2. F. Ciompi. ECOC-based plaque classification using in-vivo and ex-vivo intravascular ultrasound data. Master's thesis, UAB, Spain, 2008.
3. N. Dalal and B. Triggs. Histograms of Oriented Gradients for Human Detection. In *Computer Vision and Pattern Recognition*, volume 1, pages 886–893, 2005.
4. J. Dijkstra and G. Koning. et. al. Automatic border detection in intravascular ultrasound images for quantitative measurements of the vessel, lumen and stent parameters. In *CARS*, volume 1230 of *ICS*, pages 916–922. Elsevier, 2001.
5. J. Dijkstra and G. Koning. et.al. Automatic stent border detection in intravascular ultrasound images. In *CARS*, pages 1111–1116, 2003.
6. T. Lindeberg. Detecting salient blob-like image structures and their scales with a scale-space primal sketch: A method for focus-of-attention. *IJCV*, 11:283–318, 1993.
7. T. Ojala, M. Pietikinen, and T. Menp. Multiresolution Gray-Scale and Rotation Invariant Texture Classification with Local Binary Patterns. *IEEE TPAMI*, 24:971–987, 2002.
8. D. Rotger, P. Radeva, and N. Bruining. Automatic detection of bioabsorbable coronary stents in ivus images using a cascade of classifiers. *IEEE Transactions TITB*, 14(2):535–537, 2010.
9. P. A. Viola and M. J. Jones. Robust real-time face detection. In *ICCV*, page 747, 2001.

Index

The 1st International Workshop on Computer Assisted Stenting

http://campar.in.tum.de/STENT2012/WebHome

Sponsored by
SIEMENS
Boston Scientific

MICCAI-STENT'12

1st MICCAI-Workshop on Computer Assisted Stenting